

國立交通大學

資訊科學與工程研究所

博士論文

計算解剖學之腦區域擷取與對位演算法



Brain Extraction and Registration Algorithms

for Computational Anatomy

研究生：劉嘉修

指導教授：陳永昇 博士

中華民國九十八年十二月

計算解剖學之腦區域擷取與對位演算法  
Brain Extraction and Registration Algorithms  
for Computational Anatomy

研究生：劉嘉修      Student : Jia-Xiu Liu  
指導教授：陳永昇      Advisor : Yong-Sheng Chen

國立交通大學  
資訊科學與工程研究所  
博士論文



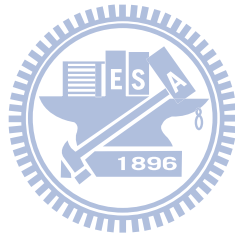
A Dissertation  
Submitted to Institute of Computer Science and Engineering  
College of Computer Science  
National Chiao Tung University  
in partial Fulfillment of the Requirements  
for the Degree of  
Doctor of Philosophy  
in  
Computer Science

December 2009

Hsinchu, Taiwan, Republic of China

中華民國九十八年十二月

To my parents



## 致 謝

謝謝永昇老師及麗芬老師

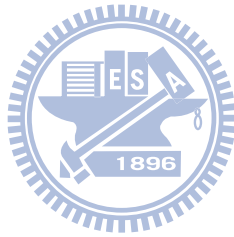
除了生活上的照顧與學業上的指導外  
老師對研究的熱誠更是影響我甚深的無形教誨

謝謝李石增醫師、江安世老師、盧鴻興老師、荊宇泰老師及林益如老師  
所給予的建議與對疏漏處的指正讓論文內容更臻詳實

謝謝常被我遙控的清偉、億婷及實驗室的學弟妹們

謝謝所有關心我的人

謝謝



## 摘要

計算解剖學 (computational anatomy) 廣泛運用非侵入式造影與影像處理方法於腦部結構分析上。為讓結構分析聚焦於腦組織並使腦結構空間標準化，腦區域擷取 (brain extraction) 與腦部結構對位 (brain registration) 在計算解剖學上扮演重要之角色。此兩項技術之準確性可提升結構分析之可信度，且其高執行效率可增加結構分析之處理容量進而提升統計效度。本論文針對快速且準確之腦部結構分析提出腦區域擷取與腦部對位演算法，並將所開發之影像處理技術運用於躁鬱症病患之腦纖維病理分析上。

在腦區域擷取方法中，本論文提出新的隱式形變模型 (implicit deformable model) 以期能有效的切割出腦部區塊。我們採用一組具區域影響性之 Wendland 輻射基底函數 (radial basis function) 以描述平滑的腦部曲線，並降低隱式形變模型之計算複雜度。在內力 (internal force) 與外力 (external force) 的交互作用下，輻射基底函數中心點將依次由初始位置逐漸推進至腦部邊界。由於不同視角下的腦部邊界曲率往往差異頗大，因此我們分別對矢狀面 (sagittal view) 與冠狀面 (coronal view) 的影像切片進行腦部區域擷取，並將不同切面的擷取結果整合以達到互補之效果。利用 Internet Brain Segmentation Repository 兩組測試影像所進行的效能評估結果，顯示本論文所提出的腦部擷取技術較 Brain Surface Extractor、Brain Extraction Tool、Hybrid Watershed Algorithm 與 Model-based Level Set 等方法有最佳的準確性與強健性 (robustness)。

在腦結構影像對位方面，我們藉由影像導數 (image derivatives) 所得到的腦結構資訊，以仿射轉換 (affine transformation) 與非線性形變模型建立測試影像與目標影像間的空間對應關係。利用腦結構方向性之不同與腦重心位置之差異可估計一組旋轉角度與位移量，以作為仿射對位的初始值。承續仿射對位之空間對應結果，所提出的非線性方法階層式的將 Wendland 輻射基底函數佈置於具顯著腦結構的區域上以描述影像的形變，仿射轉換與非線性形變均以階層式之影像解析度進行影像相似度之最佳化。一般而言，非線性最佳化 (nonlinear optimization) 結果之優劣深受初始值之影響。而本論文所提出之方法能有效的估計仿射對位與非線性對位的初始空間對應關係。運用多組高解析度與低解析度影像之效能評估結果，顯示所提出的影像對位方法較許多已廣泛運用的演算法精準且快速。另外，本論文亦以模擬影像實驗量化影像對位準確度對腦結構分析正確性之影響。

雖然罹患第一型與第二型躁鬱症 (bipolar disorders) 之病患呈現相異的表徵與認知能力 (cognitive functions)，然而此二亞型 (subtypes) 是否亦具有不同之神經基質 (neural substrates) 卻一直是未知的。為探究第一與第二型躁鬱症病患間之腦部纖維結構性差異，我們運用所開發之影像處理技術以及由擴散張量磁振造影 (diffusion tensor imaging) 所導出之非等向性指標 (fractional anisotropy) 於正常人、第一型躁鬱症病患、第二型躁鬱症病患與所有躁鬱症病患間之腦部纖

維結構之分析上。此研究採用雙樣本 t 檢定 (two-sample t-test) 之體素分析 (voxel-wised analysis) 方式進行，所發現的顯著性差異區域之平均非等向性指標亦用於探究其與臨床表徵及認知測驗分數之相關性。研究結果顯示第一與第二型躁鬱症病患的腦部纖維均在視丘 (thalamus)、前扣帶 (anterior cingulate) 與下額頁 (inferior frontal) 等位置有顯著性之結構異常。另外，第二型躁鬱症病患的腦部纖維損傷現象亦呈現於顳頁 (temporal) 及下前額頁 (inferior prefrontal) 等區域。第一型躁鬱症的右下額頁與第二型躁鬱症的左中顳頁等區域之平均非等向性指標與認知執行功能具顯著性相關，第二型之躁鬱症病患的左中顳頁與下前額頁等區域之平均非等向性指標與楊氏躁症量表 (YMRS) 分數及輕躁症發作期 (hypomanic episodes) 呈顯著性相關。此研究結果指出第一型躁鬱症病患的腦纖維異常處多與認知功能有關，而第二型躁鬱症病患具顯著性差異之位置則涵括了認知與情緒處理等功能。

本論文提出兼具高執行效率與高準確度之腦部擷取與腦結構對位等演算法，所提出之影像處理方法的高準確性可使結構分析結果更值得信賴；而其低計算複雜度可使需要大量運用腦部擷取與腦結構對位的結構分析更有效率。本論文亦將所開發的影像處理方法運用於分析躁鬱症病患的腦部纖維結構之損傷，此結構分析結果顯示第一型與第二型躁鬱症病患具有不同之神經基質。



## Abstract

Computational anatomy, or morphometry, concentrates upon the quantitative analysis of brain structure, such as gyrification study and the examination of anatomical size and shape. Neuroimaging as well as image processing techniques are extensively utilized in this emerging field. Two key computerized methods of morphometry are brain extraction and registration, which can be applied to remove the non-brain tissues followed by normalizing brain structures into a standard stereotaxic space. Accurate extraction and registration algorithms facilitate the validity of morphometric analysis. Computational anatomy generally requires large participants to provide the statistical power, and thus efficient image processing approaches support the feasibility of a large-scale study. Toward an accurate and efficient morphometric analysis, this thesis proposes a brain extraction method and brain registration algorithms. The developed image processing techniques were implemented in a voxel-based analysis protocol which was conducted to explore the fiber pathology of bipolar disorders.

The proposed brain extraction method utilizes a new implicit deformable model to well represent brain contours and to segment brain region from magnetic resonance (MR) images. This model is described by a set of Wendland's radial basis functions (RBFs) and has the advantages of compact support property and low computational complexity. Driven by the internal force for imposing the smoothness constraint and the external force for considering the intensity contrast across boundaries, the deformable model of a brain contour can efficiently evolve from its initial state toward its target by iteratively updating the RBF locations. In the proposed method, brain contours are separately determined on 2-D coronal and sagittal slices. The results from these two views are generally complementary and are thus integrated to obtain a complete 3-D brain volume. The proposed method was compared to four existing methods, Brain Surface Extractor, Brain Extraction Tool, Hybrid Watershed Algorithm, and Model-based Level Set, by using two sets of MR images along with manual segmentation results obtained from the Internet Brain Segmentation Repository. Our

experimental results demonstrated that the proposed approach outperformed others when jointly considering extraction accuracy and robustness.

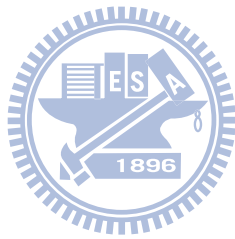
The proposed brain registration algorithms (BIRT) can rapidly and accurately register brain images by utilizing the brain structure information estimated from image derivatives. Source and target image spaces are related by affine transformation and non-rigid deformation. The deformation field is modeled by a set of Wendland's RBFs hierarchically deployed near the salient brain structures. In general, nonlinear optimization is heavily engaged in the parameter estimation for affine/non-rigid transformation and good initial estimates are thus essential to registration performance. In this work, the affine registration is initialized by a rigid transformation, which can robustly estimate the orientation and position differences of brain images. The parameters of the affine/non-rigid transformation are then hierarchically estimated in a coarse-to-fine manner by maximizing an image similarity measure, the correlation ratio, between the involved images. T1-weighted brain magnetic resonance images were utilized for performance evaluation. Our experimental results using four 3-D image sets demonstrated that BIRT can efficiently align images with high accuracy compared to several extensively adopted algorithms. Moreover, a voxel-based morphometric study quantitatively indicated that accurate registration can improve both the sensitivity and specificity of the statistical inference results.

Patients with bipolar I and II disorders exhibit heterogeneous clinical presentations and cognitive functions, however, it remains unclear whether these two subtypes have distinct neural substrates. Fractional anisotropy (FA) maps calculated from diffusion tensor images and processed by the developed techniques were compared among healthy, bipolar I, and bipolar II groups using two-sample t-test analysis in a voxel-wise manner. Correlations between the mean FA value of each survived area and the clinical characteristics as well as the scores of neuropsychological tests were further analyzed. Patients of both subtypes manifested fiber impairments in the thalamus, anterior cingulate, and inferior frontal areas, whereas the bipolar II patients showed more fiber alterations in the temporal and inferior



prefrontal regions. The FA values of the subgenual anterior cingulate cortices for both subtypes correlated with the performance of working memory. The FA values of the right inferior frontal area of bipolar I and the left middle temporal area of bipolar II both correlated with execution function. For bipolar II patients, the left middle temporal and inferior prefrontal FA values correlated with the scores of YMRS and hypomanic episodes, respectively. Our findings suggest distinct neuropathological substrates between bipolar I and II subtypes. The fiber alterations observed in the bipolar I patients were majorly associated with cognitive dysfunction, whereas those in the bipolar II patients were related to both cognitive and emotional processing.

This dissertation proposes brain extraction and registration algorithms which can rapidly extract brain volumes and align brain images with high accuracy. The high accuracy of our methods can facilitate computational anatomy to report accurate results. Due to the high execution efficiency, the developed image processing techniques are feasible to morphometric analysis which applies brain extraction and registration processes intensively. The proposed algorithms are also utilized to investigate the fiber impairments of bipolar disorders. Our analysis results demonstrated the distinct neuropathological substrates between bipolar I and II disorders.



# Contents

<b>List of Figures</b>	<b>vii</b>
<b>List of Tables</b>	<b>ix</b>
<b>1 Introduction</b>	<b>1</b>
1.1 Morphometric analysis of brain images . . . . .	2
1.2 Research scope . . . . .	4
1.3 Thesis organization . . . . .	8
<b>2 Brain extraction</b>	<b>9</b>
2.1 Background and related works . . . . .	10
2.2 Methods . . . . .	12
2.2.1 Structure information of the brain . . . . .	13
2.2.2 Estimation of image intensity parameters and brain centroid . . . . .	16
2.2.3 Brain extraction on the slices in two views . . . . .	16
2.2.4 Initial contour . . . . .	19
2.2.5 Deformable model for brain extraction . . . . .	20
2.2.6 Integration of segmentation results . . . . .	23
2.2.7 Performance evaluation . . . . .	24
2.3 Experimental results . . . . .	29
2.4 Discussion . . . . .	36
<b>3 Brain registration</b>	<b>41</b>
3.1 Background and related works . . . . .	42



3.2	Methods . . . . .	45
3.2.1	Affine registration . . . . .	46
3.2.2	Non-rigid registration . . . . .	51
3.2.3	Correlation ratio . . . . .	58
3.2.4	Evaluation of registration performance . . . . .	60
3.2.5	Effects of registration accuracy on VBM analysis . . . . .	62
3.3	Experimental results . . . . .	65
3.3.1	Comparison of affine registration algorithms . . . . .	66
3.3.2	Determination of TDOG threshold . . . . .	66
3.3.3	Comparison of non-rigid registration algorithms . . . . .	69
3.3.4	Effects of registration accuracy on VBM analysis . . . . .	71
3.4	Discussion . . . . .	71
<b>4</b>	<b>White matter abnormalities between bipolar I and II disorders</b>	<b>85</b>
4.1	Background and related works . . . . .	86
4.2	Materials and methods . . . . .	87
4.2.1	Participants . . . . .	87
4.2.2	Neuropsychological assessments . . . . .	87
4.2.3	Image acquisition and processing . . . . .	90
4.2.4	Statistical analyses . . . . .	92
4.3	Results . . . . .	92
4.4	Discussion . . . . .	96
<b>5</b>	<b>Conclusions and future works</b>	<b>99</b>
	<b>Bibliography</b>	<b>103</b>

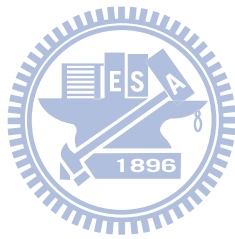
# List of Figures

1.1	MR images acquired using different pulse sequences . . . . .	3
1.2	Brain morphometric analysis system . . . . .	4
1.3	Intensity inhomogeneity of T1-weighted MR image . . . . .	5
1.4	T1-weighted MR images acquired from different scanners present quite different intensity properties . . . . .	5
2.1	Flowchart of the brain extraction method . . . . .	14
2.2	The TDOG foreground reveals the regions with relatively low intensities . . .	15
2.3	Brain surface presents quite different curvatures in the coronal and sagittal views . . . . .	18
2.4	Initial brain contour . . . . .	19
2.5	Implicit contour representation . . . . .	21
2.6	The weighting function used to constrain the evolution distance . . . . .	24
2.7	Brain extraction results of a T1-weighted MR image . . . . .	25
2.8	Excess non-brain tissues affect the extraction accuracy of BET and HWA .	30
2.9	Brain extraction risk evaluation using two IBSE data sets . . . . .	35
2.10	Influence of systematic edge artifacts to the extraction results of BSE . . . .	38
3.1	Flowchart of the proposed affine registration method . . . . .	47
3.2	Registration results between two T1-weighted MR images . . . . .	48
3.3	Brain MSP estimation and refinement . . . . .	50
3.4	Segmentation of CC on MSP . . . . .	52
3.5	Flowchart of the proposed non-rigid registration method . . . . .	53
3.6	Wendland radial basis function . . . . .	54

3.7	Hierarchical space division in non-rigid registration . . . . .	56
3.8	Correlation ratio measurement . . . . .	59
3.9	The construction of simulated images with different degrees of volume difference in the cerebellum . . . . .	64
3.10	Comparison for the stability and accuracy of affine registration algorithms .	68
3.11	Influences of the thresholding value in TDOG upon the alignment accuracy and computational efficiency of the proposed non-rigid registration method	70
3.12	Comparison for the stability and accuracy of non-rigid registration algorithms	73
3.13	VBM structural analysis results using simulated images with different scales of volume differences . . . . .	74
3.14	ROC curves of the simulated VBM structural analyses . . . . .	75
3.15	The affine registration for brains with large orientation difference . . . . .	76
3.16	Affine registration for the brain images which include the neck regions and partial brain tissues are out of the field of view . . . . .	78
3.17	Regularization degree of non-rigid registration influences the sharpness of mean alignment results . . . . .	79
3.18	A sharp image averaged from non-rigid alignment results could not imply accurate registration . . . . .	80
3.19	Inter-subject non-rigid alignment between T1-weighted and T2-weighted brain images using the proposed BIRT methods . . . . .	81
3.20	Intra-subject rigid alignment between non-diffusion-weighted and T1-weighted images using the proposed affine method . . . . .	82
3.21	Inter-subject rigid alignment between T1-weighted and CT images using the proposed affine method . . . . .	83
3.22	Registration of drosophila brains using the proposed BIRT methods . . . . .	84
4.1	Morphometric analysis protocol for bipolar patients . . . . .	91
4.2	Abnormal white matter areas found in the patients with bipolar disorders . .	95

# List of Tables

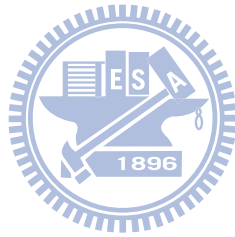
2.1	Performance evaluation for brain extraction methods using the first IBSR data set after excluding the unsatisfactory results of each algorithm . . . . .	31
2.2	Performance evaluation for brain extraction methods using the first IBSR data set without considering all the cases which caused unsatisfactory results	32
2.3	Performance evaluation for brain extraction algorithms using the second IBSR data set . . . . .	34
3.1	Performance comparison of affine registration algorithms . . . . .	67
3.2	Performance comparison of non-rigid registration algorithms . . . . .	72
3.3	The correlation coefficients between the ground truths and the t-maps obtained from VBM analysis . . . . .	73
4.1	Demographic characteristics of participants in the morphometric analysis of bipolar disorders . . . . .	88
4.2	Neuropsychological performance of participants in the morphometric analysis of bipolar disorders . . . . .	89
4.3	Regions with significantly decreased FA in patients with bipolar disorders .	94





# Chapter 1

## Introduction



## 1.1 Morphometric analysis of brain images

The great advances of medical imaging technology in past decades have facilitated the explosion of human brain mapping research. One at the core of brain mapping is computational anatomy, or morphometry, which relies on image-processing techniques and large image ensembles for the quantification of anatomical features and the changes thereof. Large participants provide statistical power as compared to the conventional psychobehavioral or molecular biological methods. The use of image processing techniques avoids subjective and labor-intensive human intervention and provides the feasibility of large-scale study. Automated longitudinal follow-up or group comparison of tissue volumes [1–6] or fiber tracts [7, 8] can thus be statistically inferred.

Non-invasive magnetic resonance (MR) images are extensively used in computational anatomy. Generally, MR imaging (MRI) provides good intensity contrast between soft tissues compared to other 3-D imaging methods, such as computed tomography (CT) and ultrasound imaging. The acquisitions of MR images with different pulse sequences result in distinct image properties which are valuable to varied clinical and research applications. For example, the majority of brain structural analyses prefer T1 weighting (Fig. 1.1a) because it performs best at defining anatomy. T2-weighted scans (Fig. 1.1b) are sensitive to water content and thus are well suited to the diagnosis of edema. Increasing brain morphometric studies utilize diffusion tensor images (Fig. 1.1c) to investigate the abnormalities or changes of white matter (WM) because it is capable of revealing subtle fiber alterations [9].

Computational approaches established for structural analysis include voxel-based morphometry (VBM), deformation-based morphometry (DBM), and surface-based morphometry (SBM) [10]. VBM differentiates anatomical differences between spatially normalized image groups in a voxel-wise manner [11]. Instead of the utilization of aligned brain images, DBM examines anatomical shape based on the deformation fields obtained from highly non-rigid registration [12]. SBM employs surface model to characterize the shape

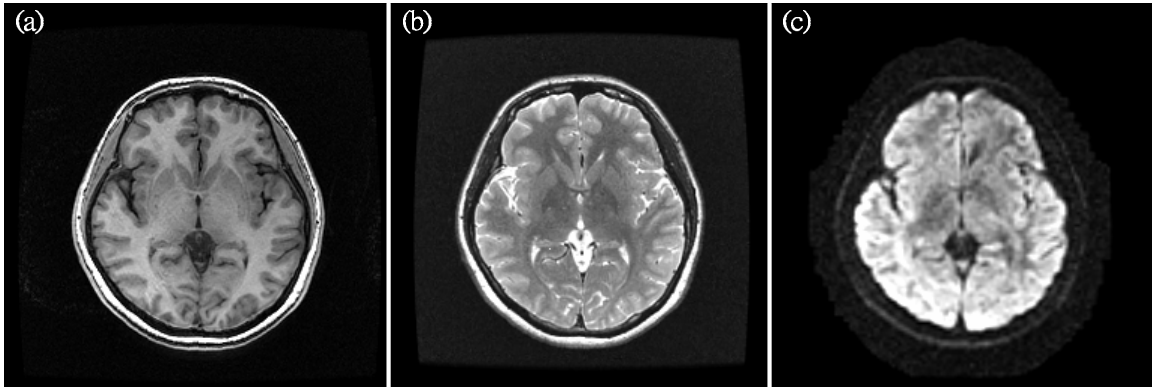


Figure 1.1: MR images acquired using different pulse sequences. (a) T1-weighted MR image. (b) T2-weighted MR image. (c) Diffusion tensor image.

properties of brain anatomy [13], such as the cortical thickness [14], sulcal depth [15], and surface curvature [16]. All these morphometric methodologies heavily rely on computerized algorithms though they are different in the underlying theoretical frameworks.

Voxel-based structural analysis of brain MR images requires a number of image processing tasks before the statistical inference, as shown in Fig. 1.2. Due to the technical factors of MRI, the intensity of homogeneous tissue is seldom uniform in each scanned image (Fig. 1.3) and may greatly alter between multi-site acquisitions (Fig. 1.4). Reducing intensity inhomogeneity and variability facilitates the accuracy and robustness of intensity-based image-processing algorithms as well as the reliability of structural analysis results [17, 18]. Image segmentation techniques, brain extraction and tissue segmentation methods, are used to determine the regions concerned in morphometric analysis, such as specific anatomical structures or the WM, gray matter (GM), and cerebrospinal fluid (CSF) tissues. Considering the accuracy of inhomogeneity correction, brain extraction is generally performed beforehand [19, 20]. Image normalization spatially registers homologous anatomical structures of intra- or inter- subjects to a standard stereotactic space. The standard space used in morphometric analysis is commonly defined by an average brain template which well represents the population [21] and is annotated with anatomical labels, such as the MNI-

305 [22] and MNI-152 [23]. Once brain structures are spatially aligned, image groups can be compared statistically in a voxel-wise manner.

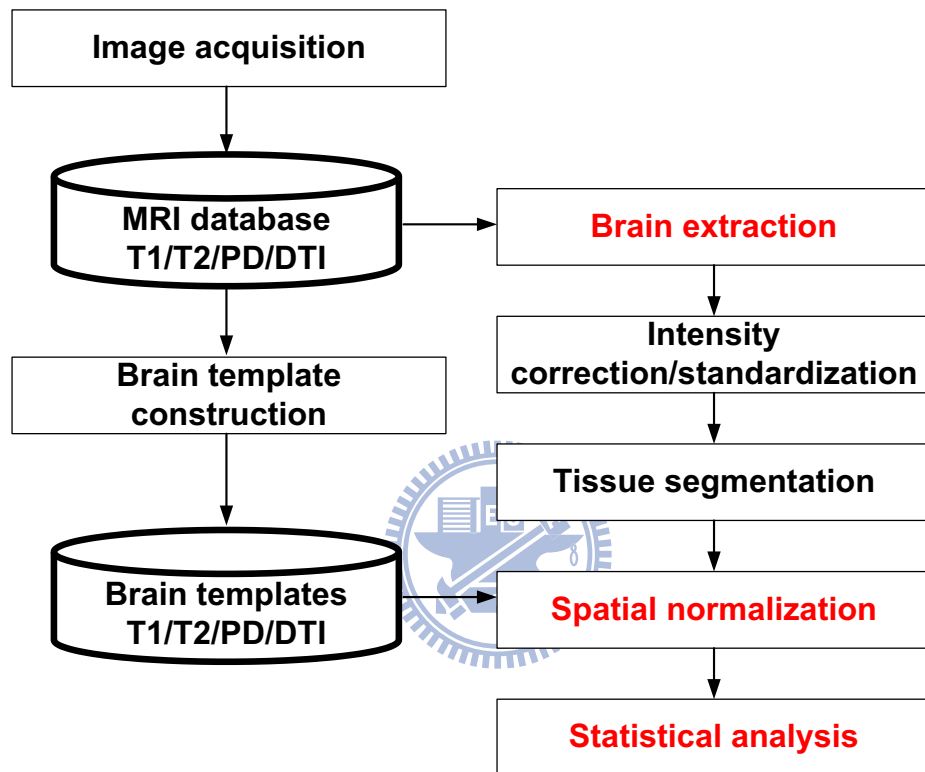


Figure 1.2: Brain morphometric analysis system. This dissertation focuses on the development of brain extraction and brain registration techniques. The developed image-processing algorithms were used for the structural analysis of bipolar patients.

## 1.2 Research scope

Toward an accurate and efficient structural analysis of human brain, this dissertation focuses on the development of brain extraction and brain registration techniques. The developed image processing techniques were implemented in a morphometric analysis protocol for the investigation of fiber pathology between bipolar I and II disorders.

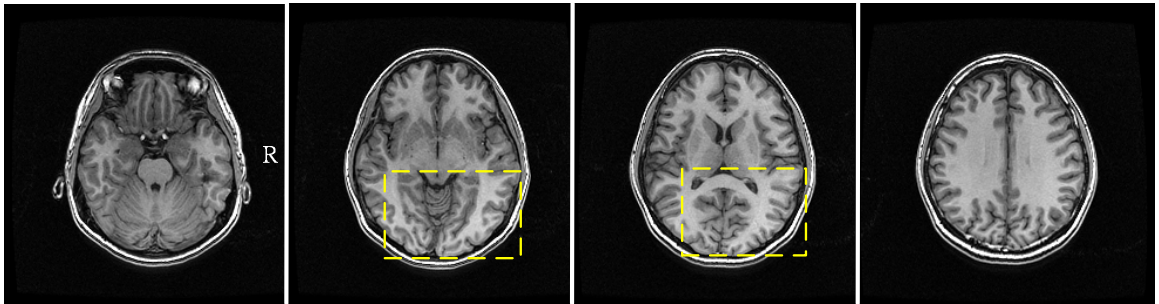


Figure 1.3: Intensity inhomogeneity of T1-weighted MR image. The right-posterior tissues highlighted in dashed boxes show obviously higher intensity compared to other regions.

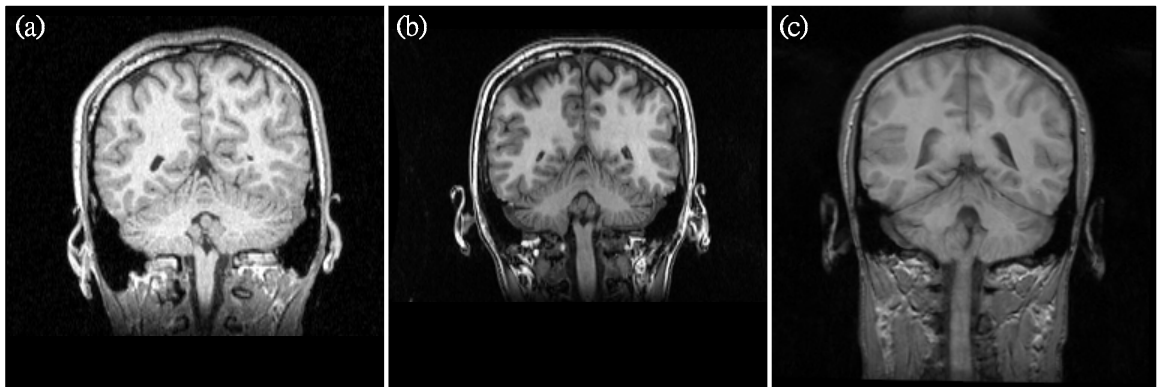


Figure 1.4: T1-weighted MR images acquired from different scanners present quite different intensity properties. MR images (a), (b), and (c) were scanned on a Bruker MedSpec S300 3T system, GE Signa EXCITE 1.5T system, and Siemens Magnetom 1.5T system, respectively.

Brain extraction from head MR image is a classification problem of segmenting image volumes into brain and non-brain regions. The difficulties of brain extraction primarily arise from the complicated brain surface and the varied intensity properties of images. Usually intensity is utilized to differentiate between brain and non-brain tissues. However, the inevitable image artifacts, intensity inhomogeneity, inapparent brain/non-brain boundaries, and the diverse intensity profiles of multi-site images can degrade the extraction performance significantly, especially for the methods based on intensity thresholding and region clustering. Extraction algorithms using deformable models are generally more robust to both image artifacts and boundary discontinuities [24–26], but these kind of methods are commonly hard to tackle the varied curvature of brain surface [24, 27].

This thesis presents a brain extraction method which utilizes a new implicit deformable model to well represent the brain contour and to segment the brain region of MR image with high accuracy. The deformable model is described by a set of Wendland's radial basis functions (RBFs) and has the advantages of compact support property and low computational complexity. Driven by the internal force for imposing the smoothness constraint and the external force for considering the intensity contrast across boundaries, the deformable model of a brain contour can efficiently evolve from its initial state toward its target by iteratively updating the RBF locations. In the proposed method, brain contours are separately determined on 2-D coronal and sagittal slices. The results from these two views are generally complementary and are thus integrated to obtain a complete 3-D brain volume.

Registration of MR brain images is a geometric operation that determines point-wise correspondences between two brains. Convoluted brain structures and considerable data amount pose obstacles to the registration of brain images, in terms of alignment accuracy and execution efficiency. Highly non-rigid method is indispensable for the alignment of brain structures with inter-subject variance or intra-subject deformation. However, it is generally difficult to determine a good spatial mapping between brains in a large parameter space. High-resolution images are helpful for precise morphometric analysis, but the large

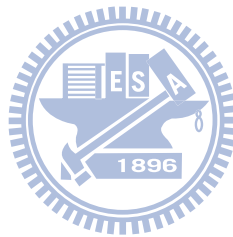
amount of data contributes to the major computational burden in registration process. On the other hand, the registration of low-resolution images is relatively time efficient at the expense of the degradation of alignment accuracy.

This thesis presents novel methods that can rapidly and accurately register brain images by utilizing the brain structure information estimated from image derivatives. Source and target image spaces are related by affine transformation and non-rigid deformation. The deformation field is modeled by a set of Wendland's RBFs hierarchically deployed near the salient brain structures. In general, nonlinear optimization is heavily engaged in the parameter estimation for affine/non-rigid transformation and good initial estimates are thus essential to registration performance. In this work, the affine registration is initialized by a rigid transformation, which can robustly estimate the orientation and position differences of brain images. The parameters of the affine/non-rigid transformation are then hierarchically optimized in a coarse-to-fine manner by maximizing an image similarity measure, the correlation ratio, between the involved images.

Bipolar disorder is a psychiatric illness which affects approximately 5% of the general population [28]. According to the clinical characteristics, bipolar disorders can be categorized into several subtypes, including bipolar I, bipolar II, cyclothymia, and bipolar disorder not otherwise specified. Although patients with bipolar I and II disorders exhibit heterogeneous clinical presentations and cognitive functions, it remains unclear whether these two subtypes have distinct neural substrates [29–31]. This dissertation utilized fractional anisotropy maps calculated from diffusion tensor images to investigate the white matter integrity of bipolar I and II disorders in a voxel-wise manner. Diffusion tensor imaging was utilized because it is capable of detecting subtle fiber alterations [32]. The developed brain extraction and registration algorithms were adopted in this morphometric study for efficient and accurate image processing as well as reliable analysis results.

### 1.3 Thesis organization

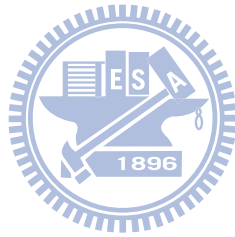
The rest of this thesis is organized as follows. Chapter 2 introduces the proposed implicit deformable model as well as the application in brain extraction. The registration techniques presented in Chapter 3 comprise an affine and a non-rigid approaches. Chapter 4 introduces the morphometric analysis conducted to examine the neuropathological substrates of bipolar I and II disorders. Finally, Chapter 5 concludes the researches presented in this dissertation.





## Chapter 2

### Brain extraction



## 2.1 Background and related works

Brain extraction is essential or beneficial to many neuroimaging applications. For example, removal of the non-brain tissues facilitates the correction of intensity non-uniformity for MR images [20]. Tissue segmentation algorithms for separating brain regions into GM, WM, and CSF usually incorporate brain extraction as a preprocessing step to simplify the segmentation problem [33–35]. Extraction of brain regions can improve the accuracy of brain image registration by avoiding the interference of inter-subject variation of non-brain structures [36], including affine and non-rigid methods [37–39]. In the past decade, VBM [11] has been extensively applied to statistically reveal regions with significant structural discrepancy between image groups [1,3,40–42]. Recent studies indicated that accurate brain extraction can improve the validity of VBM results because of better tissue segmentation and brain registration [20, 43].

Brain extraction algorithms can be classified into four major classes: (1) thresholding/clustering based methods, (2) boundary-based methods, (3) deformable model methods, and (4) hybrid methods. Thresholding/clustering based methods extract brain regions according to the phenomenon that intensities of the voxels belonging to the same tissue are similar. Lemieux et al. proposed a fine-tuned algorithm which utilizes several intensity thresholds and morphological operations to remove non-brain areas [44]. Analysis of Functional NeuroImages (AFNI) fits a Gaussian mixture model to the intensity histogram of a brain image and estimates an intensity range to segment the brain areas in a slice-by-slice manner [45, 46]. Hahn and Peitgen presented a watershed algorithm which uses a connectivity criterion, pre-flooding height, to group image voxels with similar intensities and then regards the largest connected component as the brain volume [47]. More examples can be found in [48–53]. Methods of this type are usually sensitive to image scanning parameters and image artifacts, such as noise and intensity inhomogeneity. Therefore, user intervention is usually required to determine proper parameters.

Boundary-based methods locate brain boundaries using the edge information obtained from image derivatives. Bomans et al. presented a semi-automated algorithm in which the brain region was manually labelled from the connected components detected with the Marr-Hildreth operator [54]. Brain Surface Extractor (BSE) method improved the work of Bomans et al. by adaptively smoothing the noisy regions, detecting structure edges, and automatically determining the brain volume [35,55]. In contrast to the thresholding/clustering based approaches, these methods are less sensitive to intensity inhomogeneity and scanning parameters. However, automated methods of this type may encounter difficulties in differentiating true boundaries from the false ones. For example, the GM/WM edges are usually very close to the target boundaries, the CSF/GM edges, and thus may perplex the determination of the brain volume.

Extraction methods using deformable models segment brain volumes by evolving contour or surface toward the target. Deformable model can be characterized by its representation method, implicit or explicit, and the evolution scheme [56, 57]. An explicit model directly describes the brain contour or surface and the fitting process is usually rapid [24,33,58,59]. On the other hand, implicit model can easily change the model topology, for example, to split or merge objects, but the computational complexity is usually high. The level set method adopted in Zhuang et al.'s work [26] is an example of this kind of methods. Brain extraction using deformable model is generally more robust and accurate compared to the thresholding/clustering based and boundary-based methods [24–26]. Moreover, incorporation of constraints or prior knowledge about the brain shape is relatively easy for this kind of methods. Therefore, they are more robust to both image artifacts and boundary discontinuities and can achieve subvoxel accuracy [56].

Hybrid approaches integrate the methods of different types with the anticipation to draw on the specific strengths at the expense of more computational cost [60–65]. Ségonne et al. applied the watershed algorithm [47] to generate an initial brain volume and incorporated the prior information of the brain shape into a deformable model to refine the extraction

results [25]. Rehm et al. integrated the extraction results obtained from atlas registration [36], intensity thresholding, and the BSE algorithm [35,55] by means of voting in the brain volume [66].

For large-scale studies, both accuracy and efficiency are important issues when considering brain extraction algorithms [19]. The level set methods, which use implicit deformable models, are superior in accuracy and robustness, but the computational complexity of these methods is usually very high. On the contrary, methods using explicit models are generally more efficient. However, the discretization process in this kind of methods needs to compromise between the extraction accuracy and evolution efficiency. Finer (coarser) discretization employs more (fewer) sampling points to model object boundaries and can achieve more precise (rougher) results at a relatively slow (rapid) evolution speed.

In this work, we designed a new deformable model and developed an automated brain extraction method. The deformable model is implicitly represented by a set of Wendland's RBFs and can efficiently evolve toward the target boundary by iterative updates of RBF locations. Because of the use of RBFs, the new model can smoothly represent object boundaries though each RBF keeps a distance to the neighboring ones. Brain contours of 2-D coronal and sagittal slices are individually fitted. The results of these two views are generally complementary and thus can be integrated to obtain accurate 3-D brain volumes. According to our experiments, the proposed brain extraction method outperformed others when jointly considering extraction accuracy and robustness.

## 2.2 Methods

The proposed brain extraction method comprises three major steps, as shown in Fig. 2.1. Image intensity parameters and brain centroid are first estimated for the following segmentation procedures. Then the proposed deformable model is applied to extract the brain area

on each of the coronal and sagittal slices. Complementary areas extracted from two different views are then integrated into a complete 3-D brain volume. Before the detailed description of the brain extraction method, we first introduce the structure information of the brain obtained from image derivatives. The structure information is not only useful for the estimation of intensity parameters required in our brain extraction approach but for the estimation of brain orientation and the modeling of image deformation required in the proposed registration algorithms.

### 2.2.1 Structure information of the brain

Difference of Gaussian (DOG) performs image subtraction after convolution with two Gaussian kernels  $G(\sigma_1)$  and  $G(\sigma_2)$ ,  $\sigma_1 > \sigma_2$ :

$$DOG(I, \sigma_1, \sigma_2) = G(\sigma_1) * I - G(\sigma_2) * I, \quad (2.1)$$

where  $I$  is a T1-weighted MR image and “\*” denotes the convolution operator. We define the thresholded DOG (TDOG) value to be one (foreground) when the DOG value is larger than a threshold, and otherwise the TDOG value is zero (background). Instead of using the zero-crossings of DOG results to detect edge features, we utilize the foreground in the TDOG image to reveal those regions with relatively low intensity in  $I$ , such as the GM and CSF, as shown in Fig. 2.2. We can observe that the background voxels in the brain area are mostly the WM. This information can be applied to estimate the global intensity parameters for the proposed brain extraction method. Notice that the region between two hemispheres contains mostly TDOG foreground voxels. This phenomenon can be utilized to determine the mid-sagittal planes (MSPs) and then estimate the orientation of brains. Non-brain tissues may present in TDOG foreground and can be easily removed by applying the brain masks. Then the masked foreground can guide the deployment of RBFs to cortices and ventricles in the proposed non-rigid registration method.

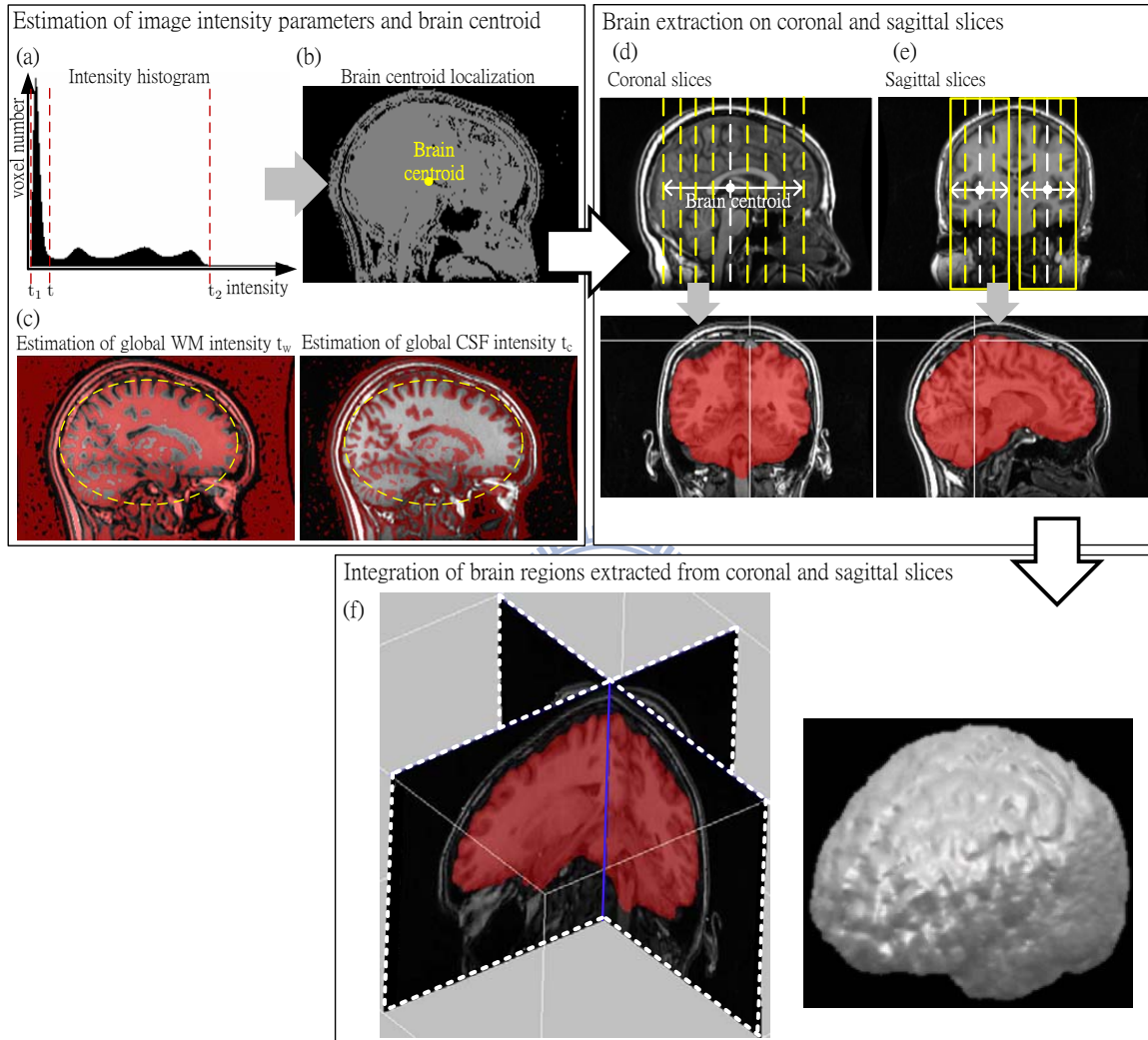


Figure 2.1: Flowchart of the brain extraction method. (a) The effective intensity range  $[t_1, t_2]$  and a rough head/background threshold  $t$  are estimated from the intensity histogram. (b) Then the voxels with intensity value within  $[t, t_2]$  are used to approximate the brain centroid. (c) Applying DOG operator with zero threshold, the global WM intensity  $t_w$  and CSF intensity  $t_c$  are decided from the voxels within the ellipsoid approximating the brain shape. The brain areas of the (d) coronal slices and (e) sagittal slices are extracted. (f) A complete 3-D brain region is determined from the complementary areas segmented from two different views.

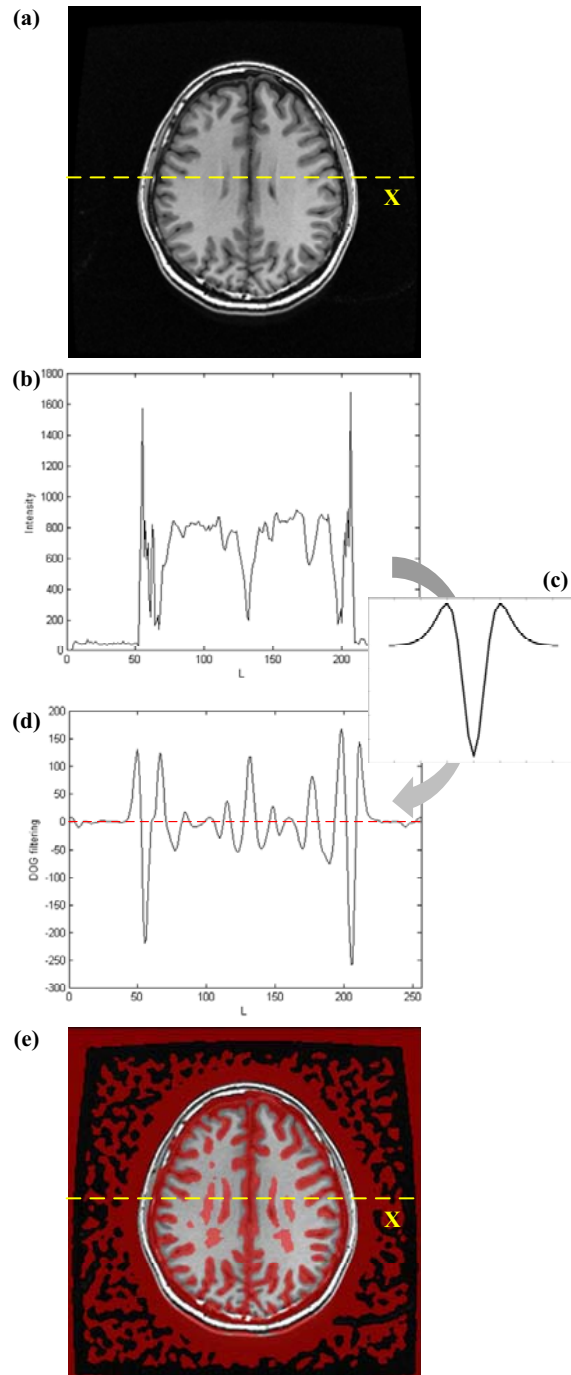


Figure 2.2: The TDOG foreground reveals the regions with relatively low intensities. (a) One axial slice of a T1-weighted MR brain image. (b) The pixel intensity profile on the scan line X. (c) An example of DOG kernel. (d) The results obtained by convolving DOG kernel to the scan line X. (e) Image overlay of the the 2D TDOG foreground (in red color) on the axial slice.

### 2.2.2 Estimation of image intensity parameters and brain centroid

We estimate the effective intensity range and centroid of the head as the work of [24]. An effective intensity range  $[t_1, t_2]$  is determined to ignore the voxels with unusual intensities, such as noises or DC spikes, in which  $t_1$  and  $t_2$  are the intensity values in the histogram such that the accumulated number of voxels reaches 2% and 98%, respectively, as shown in Fig. 2.1. To roughly separate the head from the background, the threshold  $t$  is set to be 10% in the range of  $[t_1, t_2]$ . The brain centroid  $\mathbf{O}$  is calculated by the first order image moment using the voxels with intensity value in the range of  $[t, t_2]$ .

An ellipsoid approximating the brain shape is determined by detecting the head bounding box from those voxels with intensity within  $[t, t_2]$ . The polar radius is set to the distance between the centroid and superior plane and the two equatorial radii are set to the halves of the distances between the opposite bounding planes, that is, the left-right and the anterior-posterior planes.

The voxels with DOG values smaller than zero are in the regions with relatively high intensities, which are mostly the WM areas in the brain. Therefore, the median intensity of these voxels within the brain-approximating ellipsoid estimates the global WM intensity,  $t_w$ . On the other hand, the regions with DOG values larger than zero indicate the tissues with relatively low intensities. These voxels within the ellipsoid are mostly the GM and CSF. We apply Otsu's algorithm [67] to calculate an intensity threshold  $t_o$  for separating CSF voxels from GM voxels. The median intensity of the CSF voxels estimates the global CSF intensity,  $t_c$ .

### 2.2.3 Brain extraction on the slices in two views

Brain extraction using deformable model generally requires a constraint to keep the contour or surface smooth. Loosening this constraint may lead to better fitting for the



uneven brain surface but may face the risk of leakage through the weak boundaries. On the other hand, models with strict smoothness constraint can achieve stable results, but they usually underestimate the curvature of brain surface. To tackle this problem, Smith utilized a hyperbolic tangent function with empirically obtained maximum and minimum curvature values to adaptively smooth the model of brain surface [24].

In this work, we apply the deformable contour model to extract the brain regions on both coronal and sagittal slices and then integrate the results from two views. As shown in Fig. 2.3, local curvatures of a region extracted from different views are usually quite different. Fitting a local boundary in the view with relatively low curvatures often achieve more reliable results, whereas the boundaries frequently cut through the tissues due to the high curvatures in another view. Therefore, segmentation results in different views can complement each other. Applying a strict smoothness constraint for two views followed by the simple logical OR operation for the integration can achieve accurate and stable extraction. Notice that brain extraction on the axial slices is not considered in this work because of the efficiency issue.

The segmentation in the coronal view starts with the slice nearest to the brain centroid  $O$  and proceeds with the slices toward the anterior and posterior directions. The extraction on the sagittal slices, which are parallel to the detected MSP, is divided into two parts. Each part starts with a sagittal slice 30 mm apart from the MSP and proceeds with the slices toward the MSP and the most lateral slice, as shown in Fig. 2.1. Sagittal slices within 3 mm from the MSP are not processed to avoid the unstable segmentation due to relatively few GM and WM tissues. Because the extracted brain region shrinks gradually as the extraction goes forward along the anterior, posterior, left, and right directions, brain extraction in each of these directions is terminated once the size of the extracted brain region is smaller than a threshold.

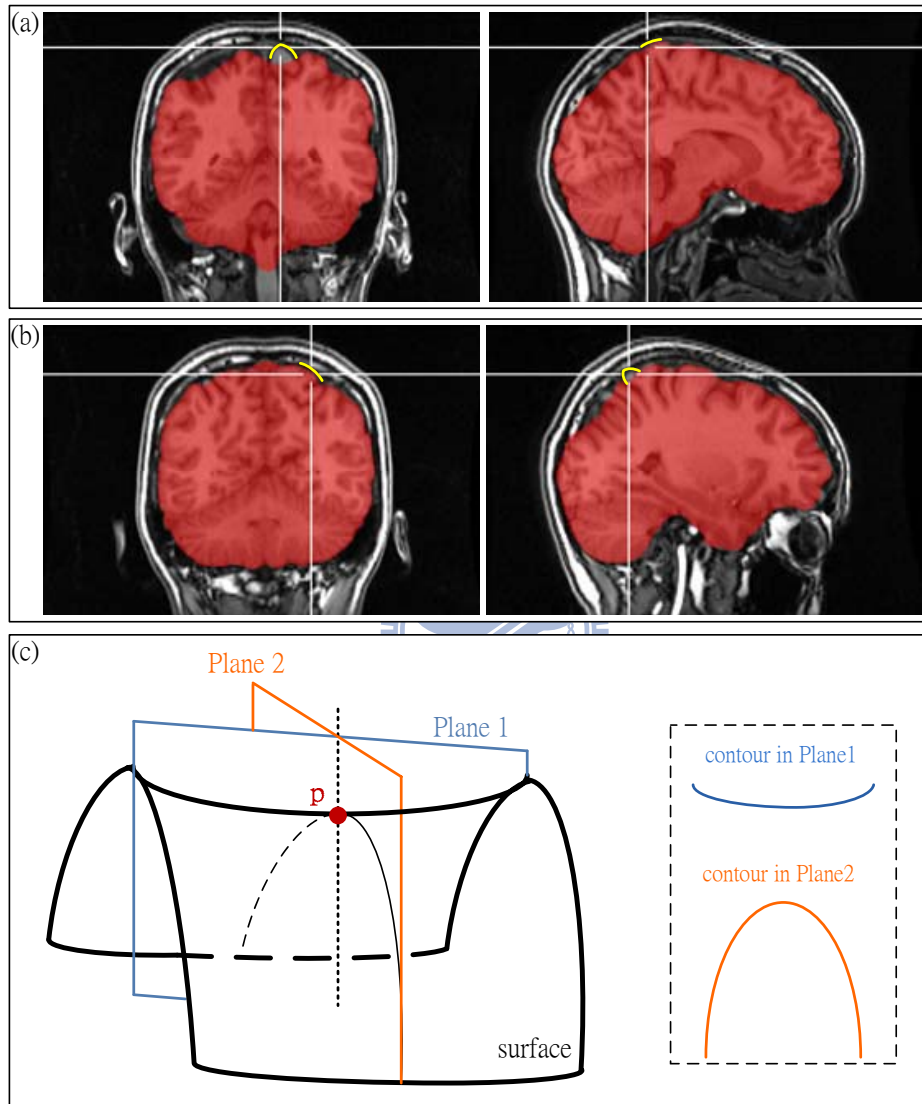


Figure 2.3: Brain surface presents quite different curvatures in the coronal and sagittal views. (a) The yellow curves show that the local curvature of brain surface in the coronal view is significantly higher than that in the sagittal view, and (b) vice versa. (c) Boundary fitting can achieve more reliable results with low curvatures than with high curvatures. The regions marked as red in (a) and (b) illustrate that the fitting results obtained from coronal and sagittal views are mutually complementary.

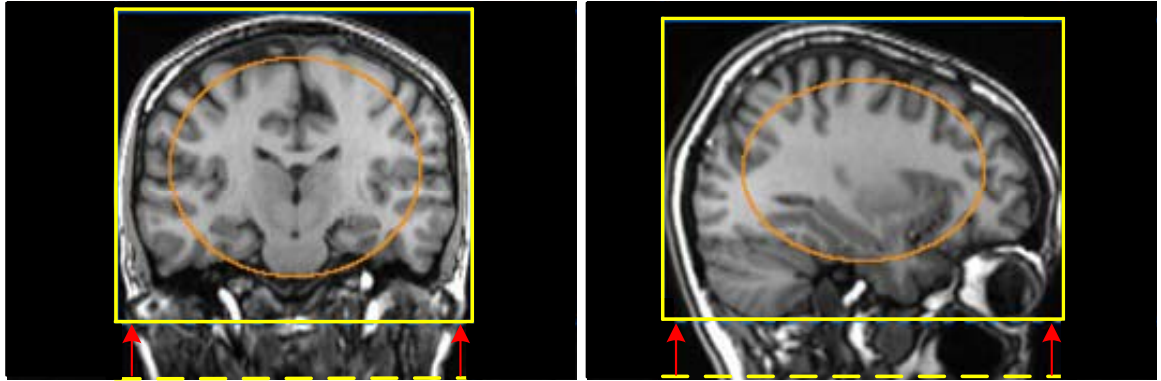
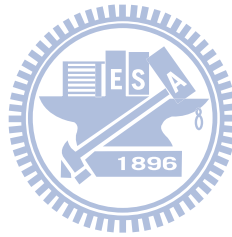


Figure 2.4: Initial brain contour. An elliptic contour centered in the approximated bounding box of the brain is regarded as the initial contour for the brain extraction on each of the starting slices.

#### 2.2.4 Initial contour



An initial contour within the brain region is required for each of the three starting slices, as shown in Fig. 2.4. The brain bounding box is first detected from those pixels with their intensity values within  $[t_1, t_2]$ . In this way the lower boundary of the bounding box is usually located at the bottom of the MR volume and is thus adjusted according to the aspect ratios 8:7 and 4:3 for the coronal and sagittal slices, respectively. A set of Wendland's RBFs are then equally spread along an ellipse centered in the bounding box with the lengths of its axes set to be 0.7 times the length and width of the box. These RBFs determine an initial contour which can evolve to fit the brain contour by the method described in the next section. Because the brain contours of adjacent slices are usually similar, the evolved contour of current slice provides a good initial for the neighboring ones. This propagation way improves the performance of brain extraction, in terms of both accuracy and efficiency.

## 2.2.5 Deformable model for brain extraction

### Implicit contour representation

A contour in a  $d$ -dimensional image space ( $d$  is 2 or 3) can be implicitly modeled as the zero set of a scalar function  $\varphi : \mathbb{R}^d \rightarrow \mathbb{R}$ :

$$C = \{\mathbf{x} \mid \varphi(\mathbf{x}) = 0, \mathbf{x} \in \mathbb{R}^d\} . \quad (2.2)$$

In this work, we define the scalar function  $\varphi(\cdot)$  as the sum of  $K$  weighted RBFs:

$$\varphi(\mathbf{x}) = \sum_{i=1}^K T_i(\mathbf{x} - \mathbf{c}_i) \phi_s(\|\mathbf{x} - \mathbf{c}_i\|) , \quad (2.3)$$

where  $\|\cdot\|$  is the Euclidean norm and  $T_i(\cdot)$  is a weighting function for the RBF  $\phi_s(\cdot)$ . The one-argument function  $\phi_s : \mathbb{R}_+ \rightarrow \mathbb{R}$  is the RBF centered at  $\mathbf{c}_i$ ,  $\mathbf{c}_i \in \mathbb{R}^d$ . This work adopts the Wendland's  $\psi$ -functions,  $\psi_{3,1}$ , as the function  $\phi_s$  because of its advantages of compact support property and low computational complexity [68, 69]:

$$\phi_s(r) = \begin{cases} (1 - \frac{r}{s})^4 (\frac{4r}{s} + 1) , & 0 \leq r < s \\ 0 , & s \leq r \end{cases} , \quad (2.4)$$

where  $s$  is the shape parameter for accommodating various extents of the compact support. Given the outward normal vector  $\mathbf{n}_i$  at  $\mathbf{c}_i$ , the weighting function  $T_i : \mathbb{R}^d \rightarrow \mathbb{R}$  is defined as:

$$T_i(\mathbf{v}) = \mathbf{v}^t \mathbf{n}_i . \quad (2.5)$$

Therefore, each  $T_i(\cdot)\phi_s(\cdot)$  term in Eq. (2.3) implicitly represents a line as the zero set in 2D image space. The normal vector at the RBF center determines the orientation of the line and the summation of these products results in a smooth contour representation, as illustrated in Fig. 2.5. Notice that we only consider the zero set within the support extents of RBFs and usually the contour does not pass through RBF centers in this model. From the implicit function, the normal vector  $\mathbf{n}_i$  at the control point  $\mathbf{c}_i$  is calculated as

$$\mathbf{n}_i = \frac{\nabla \varphi(\mathbf{c}_i)}{\|\nabla \varphi(\mathbf{c}_i)\|} . \quad (2.6)$$

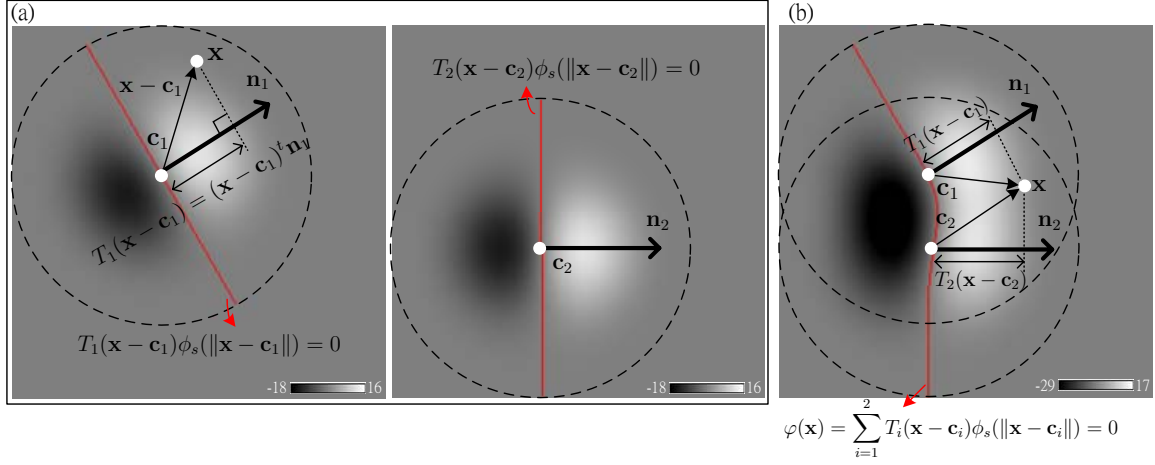


Figure 2.5: Implicit contour representation. (a) Image intensity in this figure represents the value of  $T_i(\cdot)\phi_s(\cdot)$ . The zero set where  $T_i(\cdot)\phi_s(\cdot) = 0$  within the compact support region represents the implicit model, marked as the red line. (b) The combination of  $T_i(\cdot)\phi_s(\cdot)$  can represent contour smoothly.

During the contour evolution, we adaptively allocate or deallocate RBFs according to the distance between the neighboring RBF centers.

### Contour evolution forces

The brain area on each slice is determined by iteratively moving each RBF center  $\mathbf{c}_i$  along the normal direction  $\mathbf{n}_i$  to a compromise between an internal force  $F_s(\mathbf{c}_i)$  and an external force  $F_e(\mathbf{c}_i)$ ,  $i = 1 \dots K$ :

$$\frac{\partial \mathbf{c}_i}{\partial t} = (aF_s(\mathbf{c}_i) + bF_e(\mathbf{c}_i)) \mathbf{n}_i, \quad (2.7)$$

where the weighting parameters  $a$  and  $b$  are both generally set to be 0.5.

The internal force calculated from the contour itself is used to keep the contour smooth during the evolution process. We define the smoothness constraint function  $F_s(\cdot)$  at  $\mathbf{c}_i$  as the averaged magnitude of the orientation differences between the normal vector  $\mathbf{n}_i$  and the

normal vectors  $\mathbf{n}_{i-1}$  and  $\mathbf{n}_{i+1}$  of  $\mathbf{c}_i$ 's neighboring RBFs centered at  $\mathbf{c}_{i-1}$  and  $\mathbf{c}_{i+1}$ :

$$F_s(\mathbf{c}_i) = \mathbf{u}_i^t \mathbf{n}_i \times \frac{\|\mathbf{n}_i - \mathbf{n}_{i-1}\| + \|\mathbf{n}_i - \mathbf{n}_{i+1}\|}{2}, \quad (2.8)$$

where  $\mathbf{u}_i$  is the normalized vector which starts from  $\mathbf{c}_i$  and points to the midpoint between  $\mathbf{c}_{i-1}$  and  $\mathbf{c}_{i+1}$ . Because each RBF keeps a distance to its neighboring ones, the contour smoothness is estimated from a larger scale of view, compared to the local curvature  $\nabla \mathbf{n}_i$  estimated at  $\mathbf{c}_i$ .

The external force is used to evolve the initial contour toward its target boundary. Here we modify the external force adopted in Zhuang et al.'s work [26], which originated from [33] and [24], as follows:

$$F_e(\mathbf{c}_i) = w(d, \alpha, s') \times \left( \frac{I_{\min}(\mathbf{c}_i)}{I_{\max}(\mathbf{c}_i)} - \beta \right). \quad (2.9)$$

The function above is designed according to the phenomenon that the intensity contrast between the CSF and GM/WM is usually high. Functions  $I_{\min}(\cdot)$  and  $I_{\max}(\cdot)$  find the local minimum intensity and local maximum intensity, respectively, among several sampled pixels starting from each RBF center  $\mathbf{c}_i$  along the opposite direction of  $\mathbf{n}_i$ :

$$I_{\min}(\mathbf{c}_i) = \max(t_1, \min(t_m, I(\mathbf{c}_i), I(\mathbf{c}_i - \mathbf{n}_i), I(\mathbf{c}_i - 2\mathbf{n}_i), \dots, I(\mathbf{c}_i - M\mathbf{n}_i))), \quad (2.10)$$

$$I_{\max}(\mathbf{c}_i) = \min(t_2, \max(t_w, t_m, I(\mathbf{c}_i), I(\mathbf{c}_i - \mathbf{n}_i), I(\mathbf{c}_i - 2\mathbf{n}_i), \dots, I(\mathbf{c}_i - N\mathbf{n}_i))), \quad (2.11)$$

where  $M$  and  $N$  determine the search ranges and  $t_m$  is the median intensity of the brain tissues on each slice, which is approximated from the pixels within the initial brain region. The parameter  $\beta$  is used to characterize the intensity contrast between the brain and non-brain tissues. Its value is slightly larger than the intensity ratio of the CSF to WM:

$$\beta = \frac{t_c}{t_w} + k, \quad (2.12)$$

where  $k$  is a small positive number. In this way the value of the parameter  $\beta$  is not fixed but adaptively determined because the WM and CSF intensities,  $t_w$  and  $t_c$ , are estimated from the MR image. This advantage benefits the robustness of the proposed brain extraction

method. Generally, the distance  $N$  in  $I_{\max}(\cdot)$  should be large enough to reach the WM during the evolution. Therefore,  $I_{\max}(\cdot)$  roughly equals to the local WM intensity. If the evolving contour is inside the brain region,  $I_{\min}(\cdot)$  is most likely the intensity of GM or WM. This results in a positive external force and drives the contour outward. Once the contour is outside the brain boundary,  $I_{\min}(\cdot)$  is most likely the CSF intensity and the resulted negative external force (approximately  $-k$ ) pulls the contour inward.

Because the brain boundaries of neighboring slices are usually similar, we apply a weighting function  $w(\cdot)$  to constrain the moving distance  $d$  of the RBF while the deformable model evolves from its initial position. Here the weighting function  $w(\cdot)$  is defined as the Wendland's RBF in Eq. (2.4) with support extent  $s'$ :

$$w(d, \alpha, s') = \phi_{s'}(\max(0, d - \alpha)) . \quad (2.13)$$

As the example shown in Fig. 2.6,  $w(\cdot)$  begins to gradually decrease to zero when the moving distance  $d$  is larger than  $\alpha$ . Therefore, this function regularizes the amount of brain contour evolution and thus imposes the smoothness constraint of the extracted brain volume across adjacent slices. Note that this term is set to be the constant one in the extraction process for each of the starting slices.

### 2.2.6 Integration of segmentation results

The brain regions determined from the coronal and sagittal slices are complementary and thus can be integrated to increase the sensitivity of brain extraction. Segmentation results of the sagittal slices are first transformed back to the native space because these slices are sampled from the planes parallel to the detected MSP. Logical OR operation is then applied to combine the coronal and the transformed sagittal results. Finally, we apply morphological opening with a circle as the structural element to remove the weak connected components and to smooth the brain surface. Fig. 2.7 illustrates the extraction results of a T1-weighted head image.

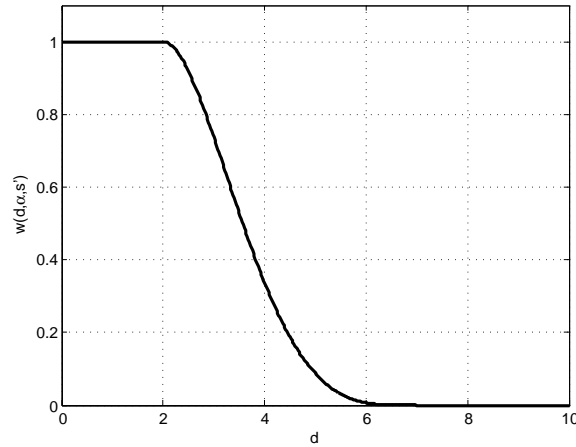


Figure 2.6: The weighting function  $w(d, \alpha, s')$  used to constrain the moving distance  $d$  of the RBF while evolving from its initial position. In this example,  $\alpha$  and  $s'$  are set to be 2 and 5, respectively.

### 2.2.7 Performance evaluation



This section introduces the methods used to evaluate the performance of the proposed brain extraction algorithm, including the data sets, performance criteria, and the approaches used for comparisons. The obtained accuracy evaluation results are further analyzed by two-sample t-test for performance comparison among the brain extraction methods. Moreover, previous evaluation works can be found in [19, 70, 71].

#### Brain extraction algorithms for performance comparisons

The proposed method was compared with the Brain Surface Extractor (BSE) in BrainSuite2 [35, 55, 72], Brain Extraction Tool (BET) version 2.1 [24, 73], Hybrid Watershed Algorithm (HWA) version stable 3 [25], and Model-based Level Set (MLS) version 0.5 [26]. The programs of the compared methods used in our experiments were downloaded from their webpages. BET, BSE, HWA, and our method were implemented in C++ whereas MLS was programmed in Java. All extraction experiments were performed on an AMD



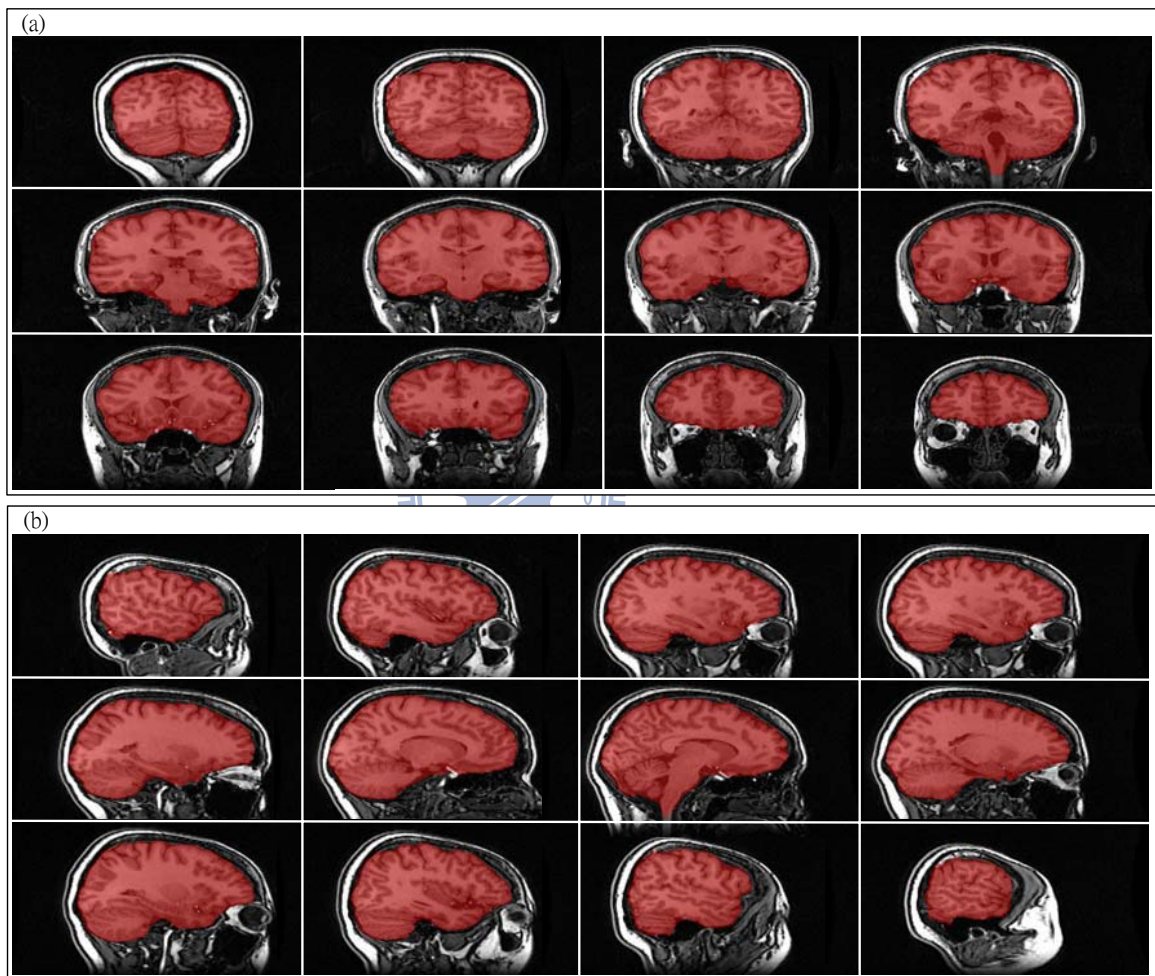


Figure 2.7: Brain extraction results of a T1-weighted image shown in (a) coronal and (b) sagittal views.

Opteron 240 processor running Linux, except BSE. Software of BSE is available only for Windows system, thus we evaluated its performance on another machine with an AMD XP 2400+ processor. Furthermore, we adopted the nearest neighbor sampling in our implementation not only because of its efficiency but also its accuracy compared to the trilinear interpolation. This observation agrees with the findings in [24]. The reason could be that sampling methods other than the nearest neighbor somewhat blur images and the resulted weak boundaries may deteriorate the accuracy of brain extraction.

### Image data sets with manual segmentation results

Two sets of T1-weighted head MR images as well as manual segmentation results were obtained from the Internet Brain Segmentation Repository (IBSR)<sup>1</sup>. In the experiments, we applied extraction algorithms to determine the brain volumes of these subjects and employed the manually segmented brain areas, including the ventricles, to evaluate the extraction accuracy.

The first IBSR data set comprises twenty MR volumes, each with around 60 coronal slices, matrix size  $256 \times 256$ , FOV  $256 \times 256$  mm<sup>2</sup>, and slice thickness 3.1 mm. Obvious intensity inhomogeneity and other significant artifacts present in most of the MR images in this data set. Another challenge of this data set is that the neck and even shoulder areas are included. This may influence the extraction accuracy of BET and HWA methods, as the examples shown in Figs. 2.8a and 2.8c (HWA even failed to process eighteen of the twenty MR images), because the excess non-brain tissues severely bias the estimation of the required parameters. To fairly evaluate extraction performance, several inferior slices of the image volumes containing neck or shoulder area were manually removed beforehand. In this way, BET and HWA achieved better segmentation results, as shown in Figs. 2.8b and 2.8d.

---

<sup>1</sup>IBSR was developed by the Center for Morphometric Analysis at Massachusetts General Hospital and is available at <http://www.cma.mgh.harvard.edu/ibsr>.

The second IBSR data set contains eighteen MR images, each with around 128 coronal slices, matrix size  $256 \times 256$ , FOV  $240 \times 240$  mm<sup>2</sup>, and slice thickness 1.5 mm. All images were transformed to radiological convention beforehand based on the orientation information obtained from IBSR. These images have superior quality in contrast to those in the first data set. According to the document of IBSR, each image in this data set has been roughly registered to the Talairach space and the intensity inhomogeneity has been corrected using the software developed by the Center for Morphometric Analysis at the Massachusetts General Hospital.

### Criteria for extraction accuracy assessment

Several criteria are utilized to measure the extraction accuracy, including the Jaccard similarity coefficient (JSC), the sensitivity and specificity coefficients, and the risk evaluation of the segmentation results. The JSC, also known as the Jaccard index, is an extensively adopted measurement which evaluates the similarity between the extracted brain region  $B$  and the corresponding ground truth  $A$ :

$$JSC(A, B) = \frac{|A \cap B|}{|A \cup B|} , \quad (2.14)$$

where  $|\cdot|$  denotes the cardinality value. The value of JSC is within  $[0, 1]$  and a larger JSC value means a better overlap with the ground truth.

Brain extraction is usually a compromise between the high recognizing percentage for brain voxels (that is, high sensitivity) and the high rejecting percentage for non-brain voxels (that is, high specificity). Therefore, the coefficients of sensitivity  $S_e$  and specificity  $S_p$  can be used to characterize brain extraction algorithms:

$$S_e = \frac{TP}{TP + FN} , \quad (2.15)$$

$$S_p = \frac{TN}{TN + FP} . \quad (2.16)$$

The true positive rate, TP, and false positive rate, FP, are the number of voxels correctly and incorrectly classified as brain tissues, respectively. The true negative rate, TN, and false negative rate, FN, are the number of voxels correctly and incorrectly classified as non-brain tissues, respectively.

In some applications, it is more important to avoid missing brain tissues than to reject all non-brain regions. From this point of view, Ségonne et al. proposed an error function  $E$  to measure the extraction risk [25]:

$$E(c) = \frac{p_f + cp_m}{1 + c}, \quad (2.17)$$

where  $c$  is the risk ratio between the probabilities of missed detection for brain tissues,  $p_m$ , and false alarm,  $p_f$ . These two probabilities are calculated as

$$p_m = \frac{|A - B|}{|A \cup B|}, \quad (2.18)$$

$$p_f = \frac{|B - A|}{|A \cup B|}, \quad (2.19)$$

where  $B$  is the extracted brain region,  $A$  is the corresponding ground truth, and  $|\cdot|$  denotes the cardinality value.

### Parameters of brain extraction algorithms

The parameters of the compared methods were determined to achieve the best average JSC value for each data set. In other words, there were two sets of parameter values for each method and each set is for one data set. For the first (second) IBSR image set, the smoothness weighting of MLS was chosen as 0.05 (0.1); the fractional intensity threshold of BET was set to be 0.6 (0.7); the parameters of HWA were set to the default values (default values with surface-shrink option turned on); the parameter  $k$  of the proposed method was set to be 0.15 (0.15); and the edge constant, diffusion iteration, and diffusion constant of BSE were set to be 3 (3), 1 (1), and 0.70 (0.66), respectively.

## 2.3 Experimental results

This section presents our results of performance evaluation for brain extraction methods. Table 2.1 lists the experimental outcomes of the proposed and other brain extraction algorithms using the first IBSR data set. In general, MLS and our method performed better than others. Jointly considering both the sensitivity and specificity, the accuracy indices of BET and BSE were moderate among the five methods evaluated. In this experiment, HWA did not achieve significant outperformance for all accuracy criteria ( $p > 0.05$ ). Notice that the performance indices of each method shown in Table 2.1 did not count in the cases that (1) the JSC value between the extracted brain volume and the ground truth is smaller than 0.6 (three cases for BSE); (2) the program terminates without any results (three cases for HWA); and (3) the extraction result is blank (one case for BSE and one case for MLS). Excluding these cases (seven in total), all methods achieved slightly larger JSC values, which means better overlapping of the extracted brain regions with the ground truths, as shown in Table 2.2. HWA had remarkable improvement in its sensitivity due to the omission of additional four poor cases. Because of the exclusion of these seven cases, outperformance of BSE and MLS to our method became significant in terms of the specificity ( $p = 0.001$ ) and JSC ( $p = 0.024$ ), respectively.

To verify that the manual removal of slices containing neck or shoulder region in the first experiment did not largely affect the performance for BSE, MLS, and the proposed methods, we applied these three algorithms again to extract the brain volumes from original IBSR images. The obtained results indicated that these three algorithms produced similar extraction outcomes no matter the excess non-brain slices were removed or not.

Table 2.3 lists the experimental results of the proposed and other extraction algorithms using the second IBSR data set. Our method generally performed better than others with respect to all accuracy criteria, except for the sensitivity. HWA achieved the best sensitivity in detecting brain tissues at the expense of the relatively low specificity. BET, MLS, and

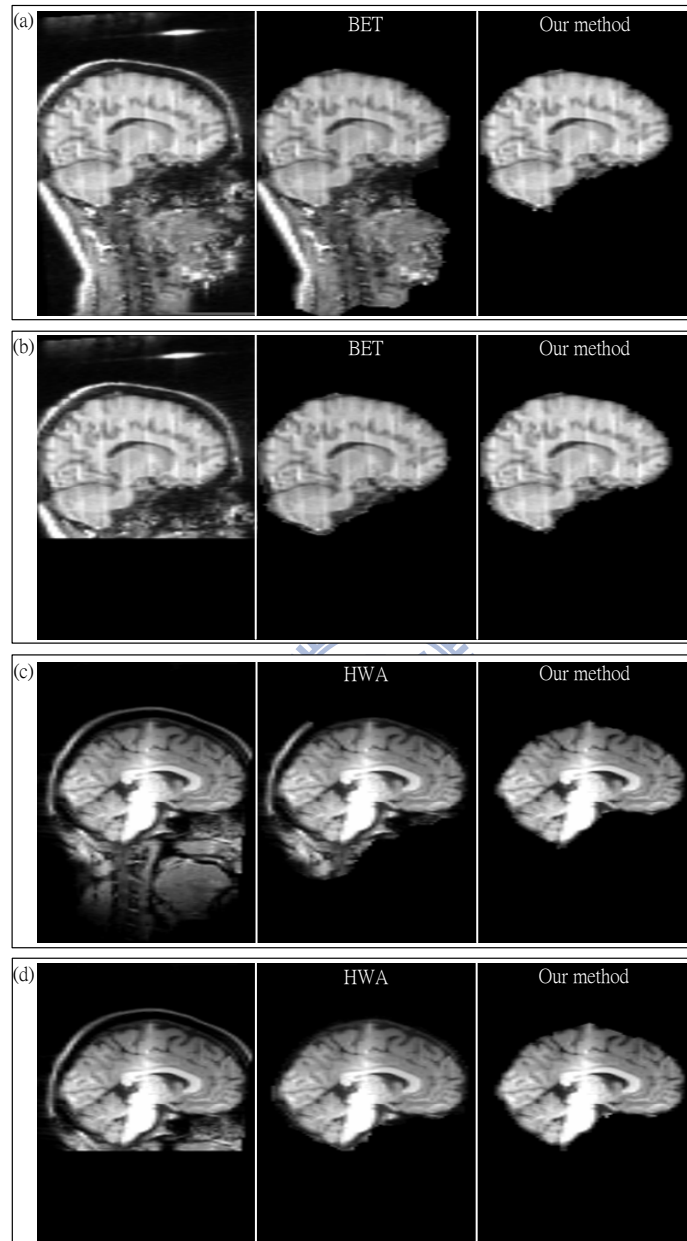


Figure 2.8: Excess non-brain tissues affect the extraction accuracy of BET and HWA. The MR images of the first IBSR data set contain neck areas, as shown in the left of (a) and (c). In this case BET and HWA cannot well extract the brain volumes, as shown in the middle of (a) and (c). Manually removing several inferior non-brain slices, as shown in the left of (b) and (d), can facilitate BET and HWA to produce better extraction results, as shown in the middle of (b) and (d). On the other hand, the proposed method is relatively robust to the excess non-brain tissues, as shown in the right from (a) to (d).

Table 2.1: Performance evaluation using the first IBSR data set after excluding the unsatisfactory results of each brain extraction algorithm.

Method	$JSC$	$S_e$	$S_p$	$p_m$	$p_f$	Time (sec.)
BET	0.878(.017) <sup>A</sup>	0.983(.023)	0.987(.004) <sup>a</sup>	0.016(.022)	0.107(.021) <sup>A</sup>	11.4 (.8)*
BSE <sup>4</sup>	0.900(.025)	0.954(.035) <sup>A</sup>	0.993(.003)	0.044(.034) <sup>A</sup>	0.055(.017) <sup>B</sup>	3.6 (1.0) <sup>+</sup>
HWA <sup>3</sup>	0.752(.037) <sup>A</sup>	0.974(.068)	0.970(.008) <sup>A</sup>	0.022(.056)	0.226(.026) <sup>A</sup>	96.1 (24.7)*
MLS <sup>1</sup>	0.922(.025)	0.989(.010)	0.992(.006)	0.011(.009)	0.067(.031)	228.6 (28.0)*
Proposed method	0.910(.018)	0.986(.013)	0.991(.005)	0.013(.013)	0.077(.027)	14.4 (3.6)*

mean (standard deviation)

<sup>A</sup>The proposed method is superior to the compared method with  $p < .01$

<sup>a</sup>The proposed method is superior to the compared method with  $p < .05$

<sup>B</sup>The compared method is superior to the proposed method with  $p < .01$

The superscripts in the first column indicate the number of the excluded cases. The marks “\*” and “+” indicate that the experiments were executed on an AMD Opteron 240 processor running Linux and an AMD XP 2400+ processor running Windows XP, respectively.



Table 2.2: Performance evaluation using the first IBSR data set without considering all the cases which caused unsatisfactory results.

Method	$JSC$	$S_e$	$S_p$	$p_m$	$p_r$	Time (sec.)
BET <sup>7</sup>	0.881(.017) <sup>A</sup>	0.981(.026)	0.988(.003) <sup>A</sup>	0.017(.024)	0.102(.021) <sup>A</sup>	11.5 (.9)*
BSE <sup>7</sup>	0.905(.025)	0.954(.035) <sup>A</sup>	0.994(.002) <sup>B</sup>	0.044(.034) <sup>A</sup>	0.051(.010) <sup>B</sup>	3.7 (1.0)+
HWA <sup>7</sup>	0.762(.012) <sup>A</sup>	0.999(.001) <sup>b</sup>	0.967(.008) <sup>A</sup>	0.001(.001) <sup>b</sup>	0.237(.013) <sup>A</sup>	91.6 (16.2)*
MLS <sup>7</sup>	0.922(.023) <sup>b</sup>	0.989(.010)	0.992(.006)	0.011(.010)	0.067(.030) <sup>b</sup>	230.2 (30.0)*
Proposed method <sup>7</sup>	0.911(.014)	0.988(.015)	0.991(.004)	0.012(.014)	0.077(.023)	19.9 (2.9)*

mean (standard deviation)

<sup>A</sup>The proposed method is superior to the compared method with  $p < .01$

<sup>a</sup>The proposed method is superior to the compared method with  $p < .05$

<sup>B</sup>The compared method is superior to the proposed method with  $p < .01$

<sup>b</sup>The compared method is superior to the proposed method with  $p < .05$

The superscripts in the first column indicate the number of the excluded cases. The marks “\*” and “+” indicate that the experiments were executed on an AMD Opteron 240 processor running Linux and an AMD XP 2400+ processor running Windows XP, respectively.



BSE were statistically equal in all accuracy criteria, except for the specificity of BSE. BSE had the significantly lower specificity in detecting non-brain regions compared to BET ( $p=0.046$ ) and MLS ( $p=0.02$ ).

Tables 2.1 to 2.3 also list the average execution time of extraction methods using the first and second IBSR data sets. Both experiments show that BSE achieved the best efficiency, followed by BET and our method, though BSE was executed on a relatively low-end processor. The processing time of HWA and MLS was apparently longer among the compared methods. Notice that MLS has a chance to achieve better efficiency if the algorithm is implemented in C/C++, instead of Java.



For each brain extraction method, the probabilities of the false classification for brain and non-brain voxels,  $p_m$  and  $p_f$ , were calculated to evaluate its extraction risk. Fig. 2.9a shows the risk profiles of the first experiment when the risk ratio  $c$  between  $p_m$  and  $p_f$  ranged from 1 to 10. It is apparent that MLS and our method have relatively lower extraction risks. BET and HWA perform better than BSE when the risk ratio is larger than 1.8 and 8.0, respectively. This figure also illustrates the extraction risk for the results excluding the seven subjects that caused markedly poor results. We can see that the performance of the proposed method, BSE, and MLS has been slightly improved. The extraction risk of HWA decreases rapidly due to its high sensitivity to the inclusion of brain tissues. The risk profiles of the second experiment shown in Fig. 2.9b indicate that the proposed method has the lowest extraction risk compared to other algorithms if the penalty is smaller than 6. HWA performs better than BSE, MLS, BET, and our method if the risk ratio is larger than 1.6, 2.0, 3.0, and 6.0, respectively.

Table 2.3: Performance evaluation for brain extraction algorithms using the second IBSR data set.

Method	$JSC$	$S_e$	$S_p$	$p_m$	$p_f$	Time (sec.)
BET	0.891(.052) <sup>a</sup>	0.959(.042)	0.989(.005)	0.038(.038)	0.071(.031)	17.9 (2.9)*
BSE	0.838(.083) <sup>A</sup>	0.957(.042) <sup>a</sup>	0.973(.030) <sup>a</sup>	0.041(.041) <sup>a</sup>	0.119(.104)	14.9 (0.5) <sup>+</sup>
HWA	0.814(.040) <sup>A</sup>	0.9997(.0003) <sup>B</sup>	0.965(.016) <sup>A</sup>	0.0002(.0002) <sup>B</sup>	0.186(.040) <sup>A</sup>	101.5 (9.7)*
MLS	0.878(.081) <sup>a</sup>	0.938(.099)	0.989(.007)	0.060(.098)	0.061(.037)	485.8 (86.1)*
Proposed method	0.915(.018)	0.978(.011)	0.990(.003)	0.021(.011)	0.064(.022)	27.4 (1.9)*

mean (standard deviation)

<sup>A</sup>The proposed method is superior to the compared method with  $p < .01$ <sup>a</sup>The proposed method is superior to the compared method with  $p < .05$ <sup>B</sup>The compared method is superior to the proposed method with  $p < .01$ 

The marks “\*” and “+” indicate that the experiments were executed on an AMD Opteron 240 processor running Linux and an

AMD XP 2400+ processor running Windows XP, respectively.

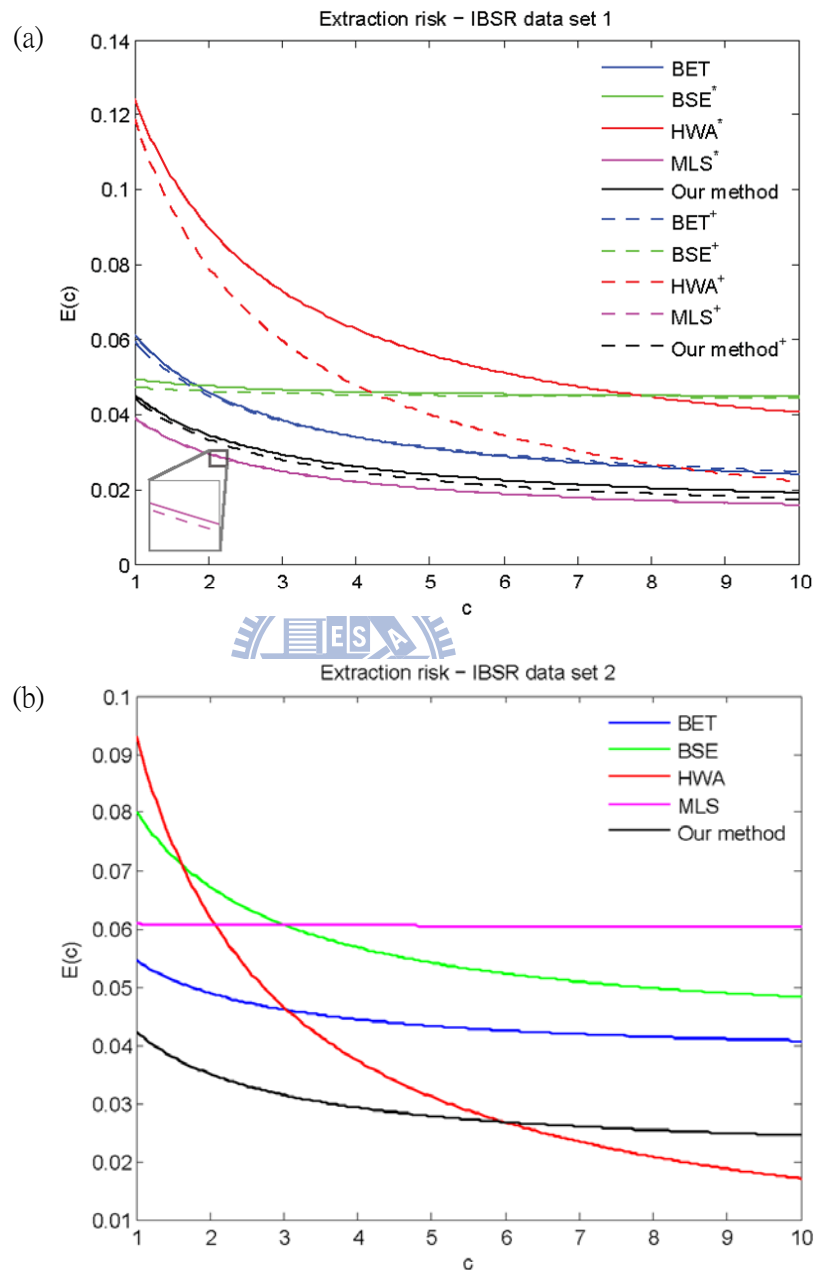


Figure 2.9: Extraction risk evaluation using (a) the first IBSR data set and (b) the second IBSR data set. The mark “\*” indicates that some failed or extremely poor segmentation case(s) are not included. After excluding all of these cases for each method, the risk profiles are shown as the dashed lines in (a).

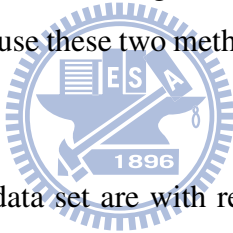
## 2.4 Discussion

Our method implicitly represents the brain contours with the proposed deformable model and explicitly evolves the contours by moving the RBF centers of the deformable model. Wendland's RBFs can well represent smooth object boundaries and are thus appropriate for brain extraction. By utilizing the explicit evolution, boundary determination of our method is efficient, at the expense of not being able to change the model topology. Therefore, the proposed model is appropriate for the application in which the object to be segmented has the same topology as the initial contour. Moreover, the performance of our deformable model, in terms of both accuracy and efficiency, can be further improved by considering adaptive RBF placement. For example, sparsely (densely) deploying RBFs with larger (smaller) support extent to the boundary with smaller (larger) curvature.

The first experiment indicated that excess non-brain tissues may greatly affect the extraction accuracy of BET and HWA. Neck or shoulder region in the image volume largely biases the estimation of brain centroid and brain size. Therefore, BET may locate the initial surface far from a reasonable position and thus fail to drive it toward the target. For HWA, the deviation of initial parameters may cause erroneous estimation of tissue intensity in the following watershed procedure. On the contrary, the proposed method is more robust that the excess non-brain regions do not obviously affect the segmentation results, as the examples shown in Fig. 2.8. In this work, we considered fully automated procedure for brain extraction. Nevertheless, softwares of both BET and HWA provide options for the manual specification of brain radius and centroid parameters to remedy the biased estimation caused from the excess non-brain regions.

Three of the compared methods, BSE, HWA, and MLS, obtained unsatisfactory extraction results or even failed for some subject(s) in the first experiment. These cases were further analyzed to comprehend the underlying properties of these extraction algorithms. By correcting the intensity inhomogeneity beforehand using the N3 method [17], MLS

produced good extraction result for the previously failed case whereas BSE and HWA still obtained unsatisfactory results. This suggests that inhomogeneity correction may improve the extraction stability of MLS. The failed cases of HWA resulted from program termination because the estimated brain size or WM intensity was too large. Manual specification of brain centroid and radius can avoid the extraction failure of HWA. This suggests that poor image quality may cause poor initial extraction results for the watershed procedure, a thresholding/clustering method, of HWA. From the excluded cases of BSE, we observed that all the images present systematic edge artifacts caused by, for example, the noise spike in k-space. Enlarging the kernel size of diffusion smoothing, BSE can improve the extraction accuracy for the images with moderate edge artifacts though it could not tackle the images with obvious edges, as shown in Fig. 2.10. On the other hand, the proposed method and BET are more robust because these two methods did not obtain poor results for the first IBSR data set.



Images of the first IBSR data set are with relatively poor quality and manifest themselves in high intensity inhomogeneity, low signal-to-noise ratio, and other significant artifacts. Image quality of the second IBSR data set is closer to what a modern MR image scanner can achieve. Quantitative evaluation results shown in Tables 2.1 to 2.3 indicated that our method can accurately extract the brain volumes for the images in both sets, and this may imply that the proposed method is less sensitive to image quality compared to other algorithms. These experiments also show that the segmentation risk using HWA decreases rapidly as the relative importance to the inclusion of brain tissues increases. This phenomenon implies that HWA is appropriate if applications prefer to keep most brain voxels at the expense of the inclusion of non-brain tissues, such as the meninges and venous sinuses.

Quantitative morphometric studies of brain MR images require a large number of subjects to increase the statistical power. In this case, MR images used for structural analysis are probably obtained from different scanners [18, 74]. Because the tissue intensity of

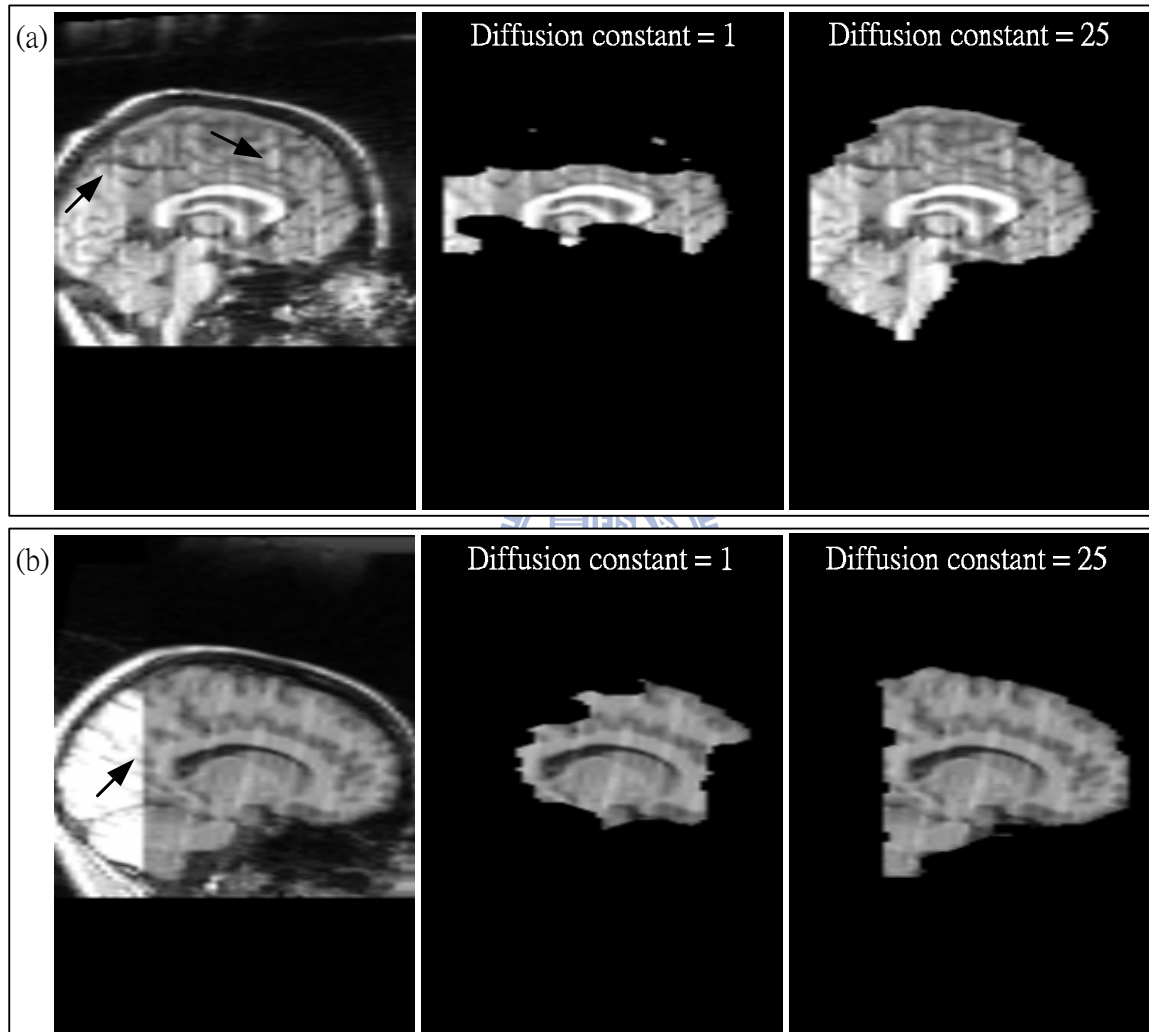


Figure 2.10: Influence of systematic edge artifacts, indicated by the arrows, to the extraction results of BSE. (a) A large kernel size of diffusion smoothing may facilitate BSE to improve the brain extraction results for the images with moderate edge artifacts, (b) but not for the images with obvious edges.

multi-site images can vary considerably, a robust brain extraction algorithm should prevent from the parameter adjustment for images obtained by different scanners. To accommodate the various intensity properties, we utilize DOG to estimate the principal parameter of our algorithm, the intensity ratio of CSF to WM. The use of image derivative reduces the influence of noise and intensity inhomogeneity. Thresholded DOG can robustly reveal the regions with relatively low and high intensity and thus it provides good information for the estimation of global CSF and WM intensities.

In conclusion, we have proposed an implicit deformable model and developed a novel brain extraction method for head MR images. Experimental results using two IBSR data sets indicated that our method can extract brain volumes with high accuracy compared to four existing algorithms, which have been extensively applied in neuroimaging applications.

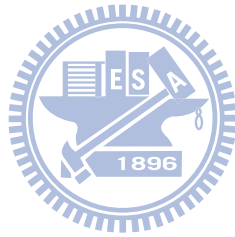






# Chapter 3

## Brain registration



### 3.1 Background and related works

Registration is an essential geometric operation in medical image analysis. In longitudinal studies, for instance, images acquired repeatedly over a period of time can be used to observe the temporal changes of brain structures by subtracting the registered images [75, 76] or by analyzing the structure deformation [77, 78]. Customized or standard brain templates can be constructed by spatially normalizing and then averaging the brain images in a stereotaxic space [21–23, 79]. Registration of an individual brain to the template can bridge the individual brain to the Talairach space [80] and can also help to obtain the gross anatomical structures of the individual brain with template-based segmentation methods [81, 82].

When registering images, the degree of structural variability determines the transformation model to be adopted. Rigid or affine transformation can only accommodate the global transformation and are adequate to register the images acquired for the same subject. Many approaches were proposed for affine registration of brain images. Ashburner et al. incorporated the prior knowledge of human brains into a Bayesian framework [83]. Wood et al. used a Newton-type method to iteratively optimize the values of transformation parameters [84]. Jenkinson et al. proposed a coarse-to-fine method that can optimize the transformation parameters from multiple candidates [37, 85].

A transformation model with a high degree of freedom is indispensable to inter-subject registration, in which the anatomical difference is non-rigid. In the following, non-rigid registration methods are briefly introduced according to the adopted transformation model. Comprehensive surveys can be found in [38, 86–88].

Elastic methods register images by compromising the deformation smoothness and the similarity measurement between images [89]. Because of the smoothness constraint, these kind of methods may not sufficiently model highly localized deformation, such as the con-

volution of cerebral cortex [90, 91]. Their variants, fluid models, relax the smoothness constraint to overcome this problem at a higher risk of false registration [90]. Fluid registration works can be found in [75, 92, 93]. Moreover, the Demons algorithm [94] and its variant [95] are also considered as an approximation of fluid registration [38].

A finite element method (FEM) registers images by using the segmented objects, which are usually represented by the meshes of tetrahedrons or hexahedrons [96–102]. It can deform objects in a more realistic way because different energy terms can be assigned to objects according to their physical properties. However, the computational complexity of the FEM approach is generally high and the error of tissue segmentation contributes to the deviation of registration.

Basis functions have been extensively applied to describe the spatial mapping relationship between images. These methods can be further divided into two sub-categories. The first kind of methods, referred as landmark-based approaches, establishes the spatial transformation from a set of corresponding control points or landmarks. Numerous basis functions have been used to model the spatial mapping, such as the thin-plate splines (TPS) [103, 104], Gaussian [105], inverse multi-quadrics [106], multi-quadrics [104], and Wendland's RBFs [69]. The major disadvantage of these kind of methods is that the identification of landmarks is not only time-consuming but also prone to errors. To alleviate this problem, Likar and Pernus applied affine registration to the sub-regions of images and regarded the centers of the registered parts as the matching control points [107].

Instead of the labor-intensive landmark selection, the second kind of methods regularly deploy basis functions in image volumes and calculate the coefficients of basis functions by optimizing an objective function. Many basis functions have been applied to model the deformation fields, including wavelets [108], discrete cosine transform [109], and B-splines [110, 111]. However, a large number of basis functions are required to model subtle deformation. In this case, the computational complexity is high and it is usually difficult to obtain good results by searching in a large parameter space. To reduce the number

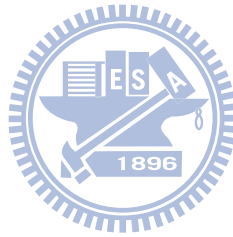
of basis functions, Rohde et al. used the gradient magnitude of the normalized mutual information (NMI) to detect poorly aligned image regions and repeatedly deployed RBFs in these regions for registration refinement [112].

Anatomical information has also been applied in non-rigid registration frameworks. Plum et al. incorporated image gradient into the similarity measurement, mutual information (MI), for utilizing the spatial information [113]. Marsland et al. iteratively determined the poorly registered regions and deployed knot points to the strong edges for modeling the deformation field with the clamped-plate splines [114]. Camara et al. registered the corresponding structures and used the obtained results to initialize the subsequent procedure for the multimodal registration of whole-body images [115]. More examples can be found in [116–120]. Generally, these type of methods take advantage of both the structure and intensity information during the registration process.

Image registration is an important tool in quantitative analysis using VBM. VBM statistically reveals the structural differences between two image groups through a voxel-wise comparison of tissue volumes [11]. There have been numerous VBM studies presented in the literature, such as the examination of brain asymmetry and the effects of sex and handedness in brain structures [2], the aging of brains [1], and the characterization of diseases [3, 40, 41]. Before the statistical comparison, all images have to be spatially normalized into the same stereotaxic space such that the corresponding structures are well aligned. Many registration techniques have been adopted in the VBM procedure and the accuracy of image registration can greatly affect the reliability of the analysis results [121–124]. Moreover, VBM analysis usually applies registration procedure intensively. Therefore, an accurate and time efficient registration algorithm is generally considered preferable for VBM.

In this work, we utilize the structure information of the brain extracted from image derivatives and develop affine and non-rigid methods, called the Brain Image Registration Tools (BIRT), for the accurate and time efficient registration of MR brain images.

The proposed affine method aligns brain images by estimating the orientation and position differences between brains followed by optimizing the similarity between images in a hierarchical manner. The non-rigid deformation of the brain is modeled by a set of Wendland's RBFs, which are hierarchically deployed near the salient anatomical structures. In this way, a small amount of RBFs are sufficient to well represent the deformation field and thus are beneficial to the execution efficiency. A VBM study of inter-group structural analysis is also conducted to qualitatively and quantitatively investigate the effect of registration accuracy upon the VBM analysis results. Software packages of the proposed registration algorithms are available at <http://bsp.cs.nctu.edu.tw/software>.



## 3.2 Methods

Image registration establishes the spatial mapping  $\mathbf{T} : \mathbf{p} \mapsto \mathbf{q}$ , which transforms every point  $\mathbf{p}$  in the source (or test) image to its corresponding point  $\mathbf{q}$  in the target (or reference) image, such that the same structures are well aligned. The mapping relation  $\mathbf{T}$  generally consists of a global transformation  $\mathbf{T}_g$ , which is usually an affine transformation, and a local, non-rigid deformation  $\mathbf{T}_1$ :

$$\mathbf{q} = \mathbf{T}(\mathbf{p}) = \mathbf{T}_g(\mathbf{p}) + \mathbf{T}_1(\mathbf{T}_g(\mathbf{p})) . \quad (3.1)$$

Notice that  $\mathbf{T}_g$  maps each point  $\mathbf{p}$  to its corresponding point  $\mathbf{T}_g(\mathbf{p})$  while  $\mathbf{T}_1$  represents the non-rigid displacement vector field. In addition, the brain structure information required in the proposed affine and non-rigid registration methods has been introduced in Sec. 2.2.1.

### 3.2.1 Affine registration

#### Overview of the affine registration method

The proposed affine registration method comprises four major steps, as shown in Fig. 3.1, which determine the twelve degrees of freedom of the transformation  $\mathbf{T}_g(\mathbf{p}) = \mathbf{A}\mathbf{p} + \mathbf{b}$ , where  $\mathbf{b}$  is a translation vector and  $\mathbf{A}$  is the transformation matrix representing the rotation, scaling, and shearing of an image volume. Among the twelve parameters of affine registration, the rigid parameters for rotation and translation are highly coupled and hence the estimation accuracy is critical to the whole affine registration process [37]. We estimate the six parameters of the rigid-body transformation by locating the MSPs followed by aligning brain volumes on the overlapped MSPs, as described in Secs. 3.2.1 and 3.2.1. Subsequently, the six rigid parameters are further refined and the results provide a good set of initial values in the parameter estimation for affine transformation. The engaged optimization process for the refinement of rigid transformation  $\mathbf{T}_r$  and affine transformation  $\mathbf{T}_g$  utilizes a hierarchical image structure and the Nelder-Mead downhill simplex method [125] to maximize the correlation ratio (CR),  $S_{\text{CR}}(I_t, I_s, \mathbf{T}_r)$  and  $S_{\text{CR}}(I_t, I_s, \mathbf{T}_g)$ , between the spatially mapped source image  $I_s$  and target image  $I_t$ . Fig. 3.2(d) shows an example of the alignment results using our affine registration method. Detailed description about CR criterion will be given in Sec. 3.2.3.

#### Determination of brain MSP

The MSP of a brain is defined as the plane which best separates the two hemispheres [126]. Locating brain MSPs requires the estimation of two rotation and one translation parameters among the six parameters of rigid transform. Some methods of automatic determination of MSPs can be found in [127], [128], and [126]. In this work, we first estimate the MSP in an analytical way. By utilizing the first order image moment as the work of [24],

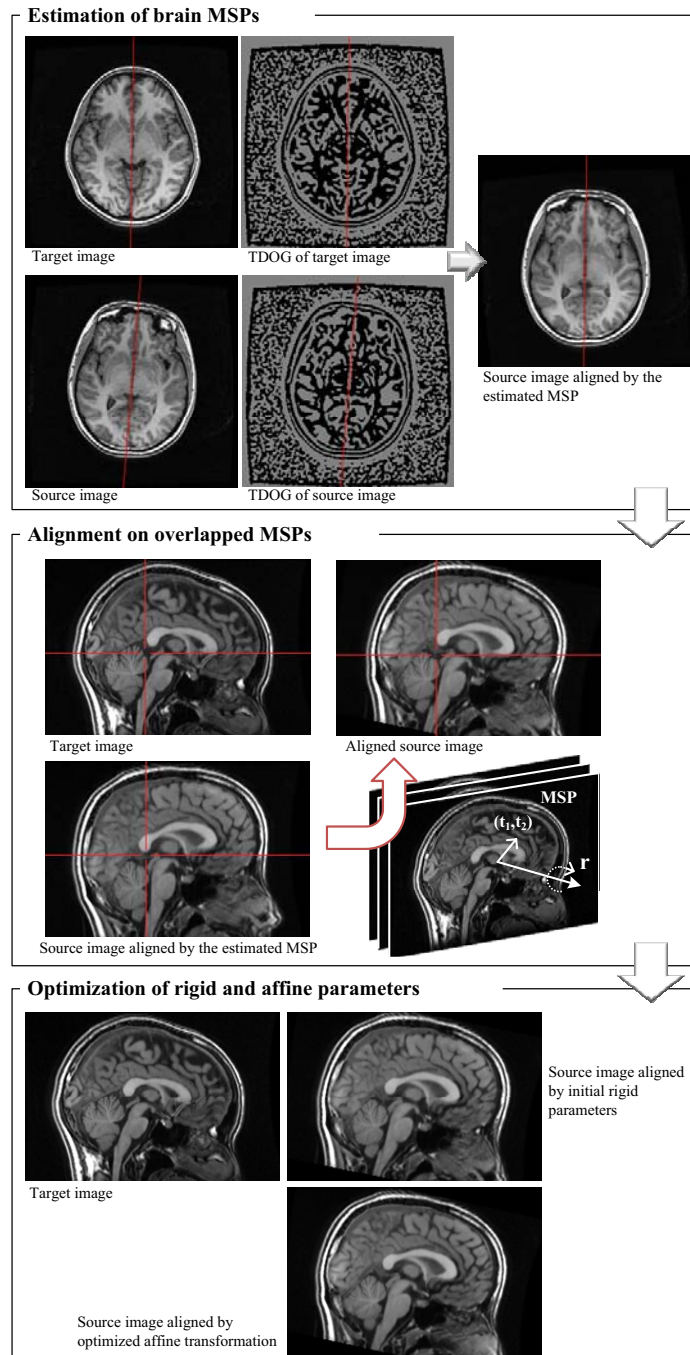


Figure 3.1: Flowchart of the proposed affine registration method. The brain MSPs in the source and target images are determined according to the TDOG images and are then overlapped together. The alignment on the overlapped MSPs is achieved by maximizing the image similarity. The obtained rigid parameters are further refined and then applied to initialize the affine registration of brain images.

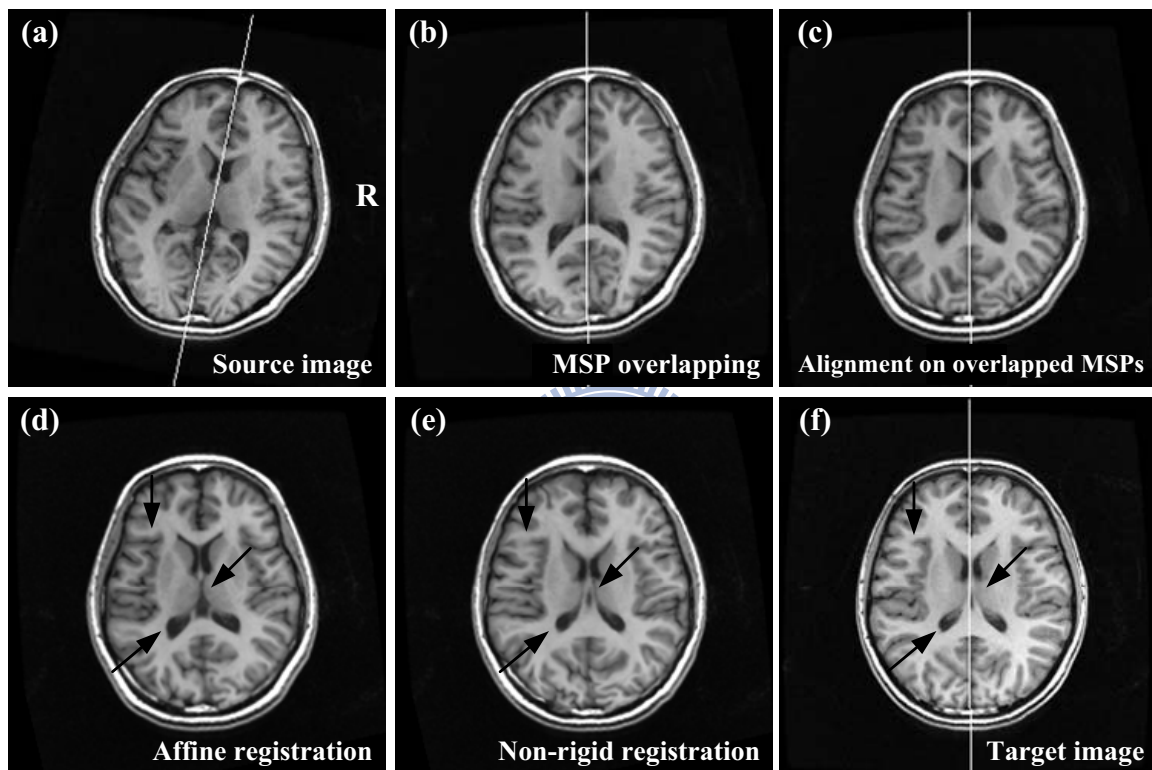


Figure 3.2: Registration between the source image (a) and the target image (f) by using the proposed BIRT methods. The slices shown from (b) to (e) illustrate the results of the MSP overlapping, alignment on the overlapped MSP, affine registration, and non-rigid registration, respectively. The white line in (a) indicates the estimated MSP of the source image whereas those in (b), (c), and (f) indicate the estimated MSP of the target image. The arrows in (d) and (e) indicate those areas with stepwise improved alignment refined by the proposed affine and non-rigid methods.



the brain centroid is calculated as a point on the initial MSP. The normal vector of the initial MSP is estimated by applying principal component analysis (PCA) to the TDOG image. As the example shown in Fig. 3.3(a), the TDOG foreground is planarly distributed nearby the MSP, whereas the distribution is more isotropic in other regions. Applying PCA to the TDOG image, the two eigenvectors corresponding to the largest two eigenvalues roughly span the MSP and the eigenvector corresponding to the smallest eigenvalue provides an estimate for the normal vector of the MSP. Fig. 3.3(b) shows that the closed-form solution provides a good initial estimation of the MSP. This initial estimation is further refined toward the “relatively darkest” plane in the brain by maximizing the number of TDOG foreground voxels. This optimization process can improve the MSP determination, as shown in Fig. 3.3(c), as well as the overlapping of the MSPs in the source and target images, which is required in the proposed affine registration method, as shown in Fig. 3.2(b).



### Alignment on the overlapped MSPs

We align the brain volumes on the overlapped MSPs to estimate other three rigid parameters, including a translation vector on the MSP and a rotation angle around the MSP normal. The rotation angle is first estimated by the directions of corpus callosums (CC) segmented from the MSPs. Applying PCA to the segmented CC, the eigenvector corresponding to the largest eigenvalue provides an estimate of the CC direction. Directional difference between CCs gives a good initial estimate of the rotation around the MSP normal. The rotation angle and the translation vector compose a rigid transform  $\mathbf{T}'_r$  and are refined by optimizing the CR,  $S_{CR}(I_t, I_s, \mathbf{T}'_r)$ , between the source image  $I_s$  and target image  $I_t$ . As shown in Fig. 3.2(c), the proposed method can robustly register brain images, even if there are large rotational differences in some unusual cases.

The segmentation of CC is based on the phenomenon that the intensities of CC in a T1-weighted MR image are significantly larger than those of the surrounding tissues. One

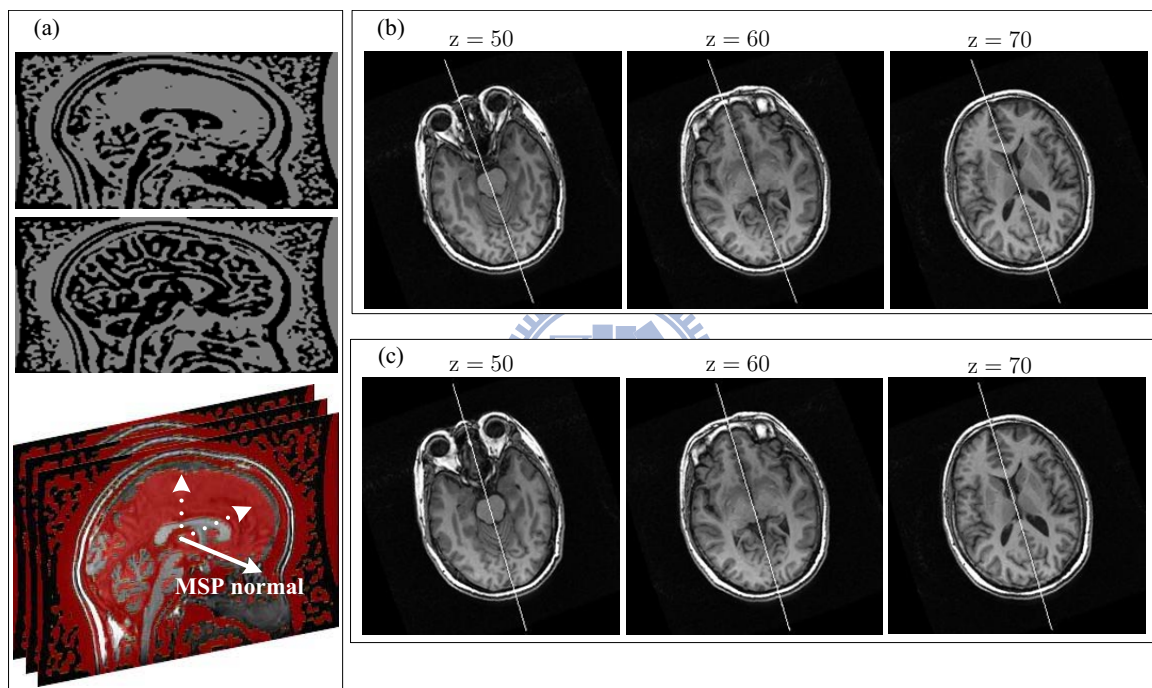


Figure 3.3: Brain MSP estimation and refinement. (a) TDOG image is more planarly distributed nearby the MSP (top), compared to other regions (middle). Applying PCA to the TDOG image, the eigenvector corresponding to the smallest eigenvalue gives an estimate to the MSP normal (bottom). (b) The MSP estimated with an analytical solution. (c) The MSP refined by maximizing the number of foreground TDOG voxels.

or two intensity thresholding steps are used to segment the CC. For each located MSP, we first calculate an effective intensity range  $[t_1, t_2]$  to ignore the pixels with unusual intensities, the brain centroid  $\mathbf{O}$ , and a radius  $r$  mm which estimates the brain size, as the work of [24]. The segmentation of CC only considers the area within the circle with center at  $\mathbf{O}$  and with radius  $kr$  mm, where the value of  $k$  is set to be 0.7 in our implementation, as shown in Fig. 3.4(a). All the connected regions with intensity larger than  $t_1 + \beta(t_2 - t_1)$  and with area larger than  $\gamma$  are extracted from MSP, where the values of  $\beta$  and  $\gamma$  were set to be 0.7 and 100 mm<sup>2</sup> in BIRT, respectively. We regard the extracted region(s) as the candidate(s) of CC. The segmentation of CC is achieved if there is only one CC candidate, as shown in Fig. 3.4(b). However, the intensity differences between CC and the surrounding tissues can vary considerably and thus the regions other than CC often survive in the first thresholding process, as shown in Fig. 3.4(d). To further distinguish these tissues, we apply Otsu's method [67] to calculate another intensity threshold if there are many CC candidates. Notice that only the pixels in the candidate regions are involved in the calculation. The proposed method can well segment the CC on MSP, even if there are excess non-brain tissues, such as the neck and shoulder areas, as shown in Fig. 3.4(e). Nevertheless, extracting the brain regions beforehand increases the robustness of our segmentation method because it avoids the disturbance of non-brain tissues, which can result in the estimation bias of the brain centroid, as shown in Fig. 3.4(c).

### 3.2.2 Non-rigid registration

Non-rigid spatial mapping between brain images is related by a set of Wendland's RBFs with different levels of support extents. Fig. 3.5 shows the flowchart of the proposed non-rigid registration procedure. Non-brain structures are first removed because the inter-subject variation of these regions is relatively large compared to that of brain tissues and hence could interfere with registration efficacy [36]. Therefore, we use a brain mask to extract the brain area as well as the boundary of the brain in the TDOG image, referred

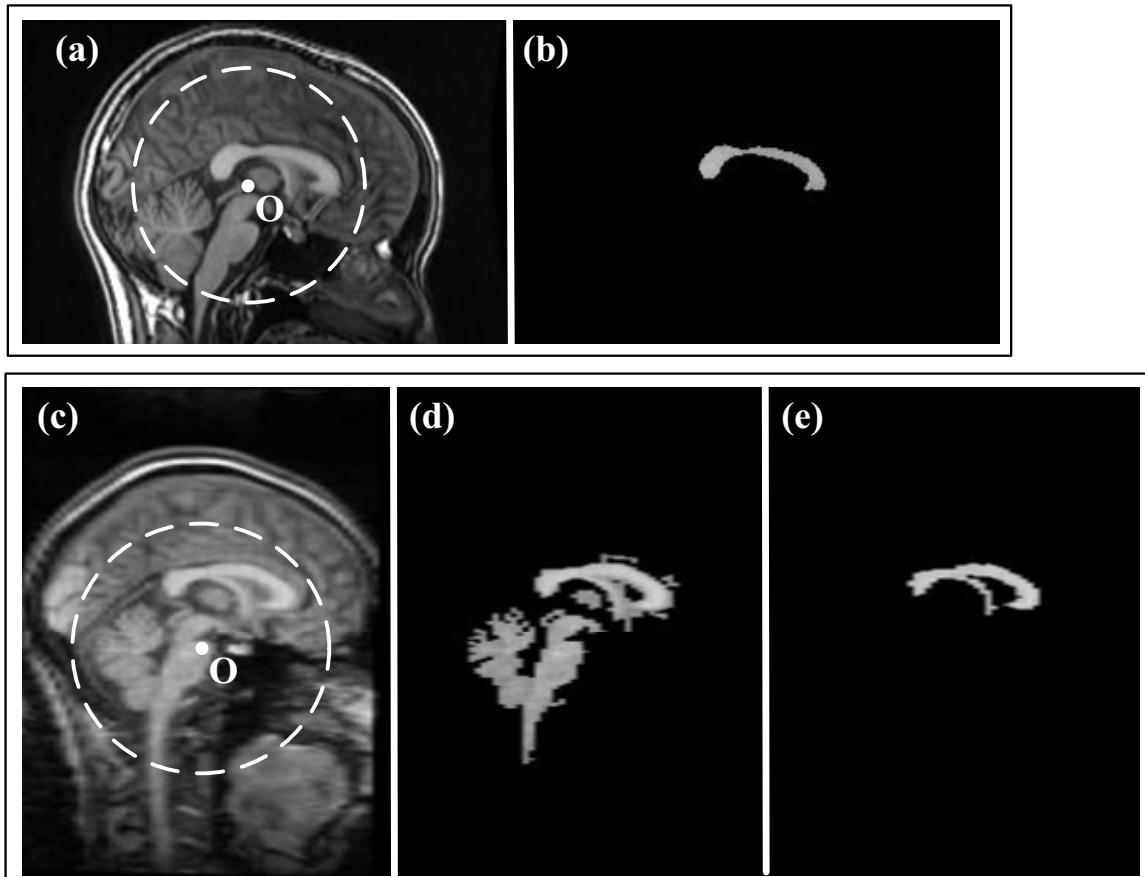


Figure 3.4: Segmentation of CC on MSP. (a) The circular area centered at the gravity of brain MSP,  $O$ , is considered in the segmentation of CC. (b) Only one connected region, the CC on MSP, is found in the first thresholding step locates the CC. (c) Excess non-brain tissues can bias the estimation of the circular area considered in the CC segmentation. (d) The intensity differences between CC and the surrounding tissues are not significant and thus many connected regions, the candidates of CC, are found in the first thresholding step. (e) Applying Otsu's method [67], the calculated intensity threshold can distinguish the CC from other tissues.

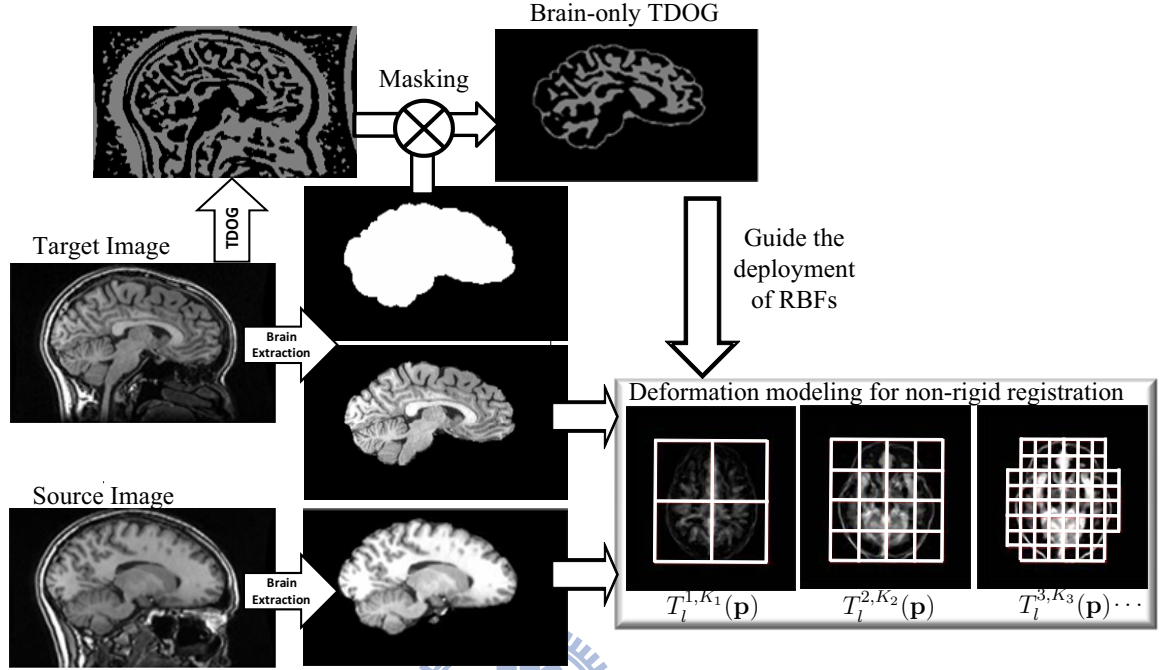


Figure 3.5: Flowchart of the proposed non-rigid registration method. Non-brain regions of the target brain are first removed to obtain a brain mask, which is then used to extract the brain region in the TDOG image of the target brain and construct the brain-only TDOG. The deformation field is modeled by a set of Wendland's RBFs hierarchically distributed at the anatomical structures revealed in the brain-only TDOG.

as the brain-only TDOG. Though the structures revealed in the brain-only TDOG are quite rough, they provide a guidance to deploy RBFs near the brain boundary, the boundary between GM and WM, and the boundary between CSF and GM/WM. Furthermore, the deformation field is progressively estimated by optimizing the coefficients of each RBF in a coarse-to-fine manner.

### Non-rigid transformation model

We use a combination of  $K$  RBFs to model the non-rigid deformation field,  $\mathbf{T}_1(\cdot)$ ,

$$\mathbf{T}_1(\mathbf{p}) = \sum_{i=1}^K \alpha_i \phi(\|\mathbf{p} - \mathbf{c}_i\|) , \quad (3.2)$$

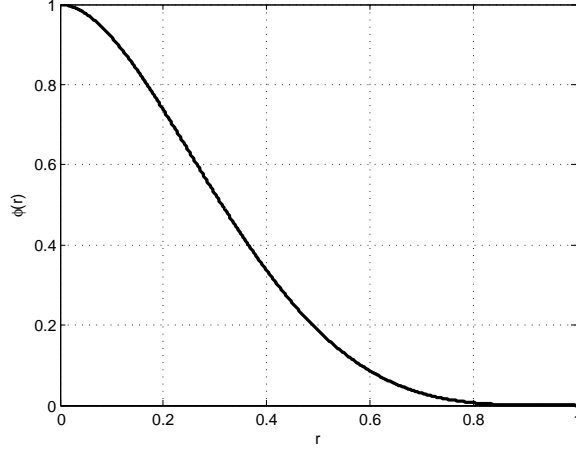


Figure 3.6: Wendland's RBF  $\phi(r)$  adopted in this work.

where  $\|\cdot\|$  is the Euclidean norm and the one-argument function  $\phi : \mathbb{R}_+ \rightarrow \mathbb{R}$  is the RBF centered at  $\mathbf{c}_i$  with coefficients  $\alpha_i \in \mathbb{R}^3$ ,  $i = 1, \dots, K$ . There are different types of RBFs. In this work, we use one of the Wendland's  $\psi$ -functions,  $\psi_{3,1}$ , as the RBF  $\phi$  due to its low computational complexity and the compact support property [68, 69]. This function  $\phi$  is shown in Fig. 3.6 and is formulated as

$$\phi(r) = \begin{cases} (1-r)^4(4r+1) & , \quad 0 \leq r < 1 \\ 0 & , \quad 1 \leq r \end{cases} . \quad (3.3)$$

Based on this set of  $K$  RBFs, the positions  $\mathbf{c}_i$  and the coefficients  $\alpha_i$ ,  $i = 1, \dots, K$ , of the RBFs determine the 3-D displacement vector  $\mathbf{T}_1(\mathbf{p})$  for each point  $\mathbf{p}$  in the image volume.

With the compact support property, the influence of each RBF is restricted to a local region which is a unit sphere around the RBF center. It is a preferred characteristic in non-rigid registration because the deformation of one area should not affect remote regions. This property also greatly alleviates the computational complexity of spatial transformation in contrast to the functions with global support, such as TPS and multi-quadrics, because only a few RBFs are involved in the calculation of displacement vector for an image point. To accommodate various extents of compact support, the argument  $r$  of the function  $\phi(\cdot)$

is scaled by the shape parameter,  $s$  [129]. The Wendland's RBF with support extent  $s$  is formulated as

$$\phi_s(r) = \phi\left(\frac{r}{s}\right) . \quad (3.4)$$

### Hierarchical decomposition of deformation field

For the  $K$  RBFs involved in our non-rigid deformation model, there are  $L$  different support extents,  $s_j$ ,  $j = 1, \dots, L$ , each with  $K_j$  RBFs and  $K_1 + K_2 + \dots + K_L = K$ . Therefore, the non-rigid deformation field,  $\mathbf{T}_l(\cdot)$ , can be rewritten as

$$\mathbf{T}_l(\mathbf{p}) = \sum_{j=1}^L \sum_{i=1}^{K_j} \alpha_{j,i} \phi_{s_j}(\|\mathbf{p} - \mathbf{c}_{j,i}\|) , \quad (3.5)$$

where  $\phi_{s_j}(\cdot)$  denotes the RBF with support extent  $s_j$  and coefficients  $\alpha_{j,i}$  centered at  $\mathbf{c}_{j,i}$ . For proper deployment of RBFs, brain volume is hierarchically divided into eight equal subregions, which are cubes in our implementation, and each subregion has an RBF placed at the center if this region contains any foreground voxels in the brain-only TDOG, as shown in Fig. 3.7. Although the maximum number of RBFs required at level  $j$  is  $8^j$ , the use of brain-only TDOG can help to place necessary RBFs near important anatomical features and avoid the dramatic increase of the number of RBFs. This deployment method is fairly beneficial for computational efficiency while maintaining high registration accuracy, particularly at the fine levels. The support extent  $s_j$  at each level  $j$  is a parameter which is set to be multiples of the width of subregions. Therefore, the RBFs from low to high levels are capable of modeling the deformation field from coarse to fine resolutions.

Since the deformation field model is hierarchically decomposed into RBFs with different levels of support extent, we estimate the coefficients of RBFs one-by-one while gradually accumulating the deformation field in a coarse-to-fine manner. Consider the coefficient estimation for the  $m$ -th RBF at level  $l$ . The centered positions and coefficients of the RBFs at the coarser levels from 1 to  $l - 1$  and the RBFs from 1 to  $m - 1$  at level  $l$  are all deter-

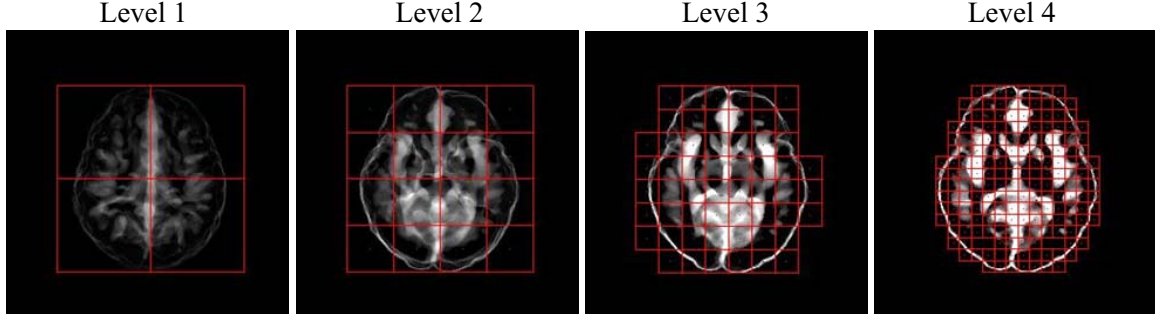


Figure 3.7: The whole brain volume is hierarchically divided into eight subregions. An RBF is deployed at the center of a subregion containing salient structure revealed by the brain-only TDOG. This figure illustrates the RBF distributions at four levels, in which a red square represents a subregion deployed with an RBF.

mined previously. We update the deformation field by adding a new RBF  $\phi_{s_l}(\|\mathbf{p} - \mathbf{c}_{l,m}\|)$  centered at  $\mathbf{c}_{l,m}$  with coefficients  $\alpha_{l,m}$ :

$$\mathbf{T}_1^{l,m}(\mathbf{p}) = \sum_{j=1}^{l-1} \sum_{i=1}^{K_j} \alpha_{j,i} \phi_{s_j}(\|\mathbf{p} - \mathbf{c}_{j,i}\|) + \sum_{i=1}^{m-1} \alpha_{l,i} \phi_{s_l}(\|\mathbf{p} - \mathbf{c}_{l,i}\|) + \alpha_{l,m} \phi_{s_l}(\|\mathbf{p} - \mathbf{c}_{l,m}\|) . \quad (3.6)$$

In this way, the displacement vector for the point  $\mathbf{p}$  is progressively updated. The accumulation process terminates when  $l = L$  and  $m = K_L$ , that is,  $\mathbf{T}_1(\mathbf{p}) = \mathbf{T}_1^{L,K_L}(\mathbf{p})$ . Because only three coefficients of an RBF are estimated at a time, the proposed method avoids the searching in a huge parameter space and thus the whole optimization process is quite fast.

### Objective function

Coefficient estimation for each RBF is an optimization process that minimizes an objective function:

$$C(I_t, I_s, \mathbf{T}) = -S_{\text{CR}}(I_t, I_s, \mathbf{T}) + \lambda E(\mathbf{T}) , \quad (3.7)$$

where  $\mathbf{T}$  is the spatial mapping between the target image  $I_t$  and the source image  $I_s$ ,  $S_{\text{CR}}$  measures the image similarity by CR, the smoothness regularization function  $E$  calculates



the deformation energy of  $\mathbf{T}$ , and the parameter  $\lambda$  compromises the measurements  $S_{CR}$  and  $E$ . The Laplacian model and the thin-plate model are widely applied to regularize the structure deformation in image registration [91]. Due to the computational efficiency, we adopt the Laplacian model in this work:

$$E(\mathbf{T}) = \frac{1}{V} \iiint \left[ \left( \frac{\partial \mathbf{T}}{\partial x} \right)^2 + \left( \frac{\partial \mathbf{T}}{\partial y} \right)^2 + \left( \frac{\partial \mathbf{T}}{\partial z} \right)^2 \right] dx dy dz , \quad (3.8)$$

where  $V$  is the volume involved in the estimation. The Nelder-Mead downhill simplex method is utilized to optimize the objective function. Fig. 3.2(e) demonstrates that the proposed non-rigid method can well register the corresponding anatomical structures.

### Implementation issues



In the optimization process of non-rigid registration, iterative calculation of image transformation contributes to the major computation burden, particularly when registering high resolution image volumes. The hierarchical decomposition of the non-rigid transformation model and the compact support property of Wendland's RBFs are both beneficial to the alleviation of this heavy burden. However, the execution time of non-rigid registration is still large. Some implementation techniques described below are helpful to further improve the efficiency. First, we construct a volume pyramid with  $L'$  levels for each MR image volume, generally  $L' \leq L$ . When evaluating the objective function, the  $K_j$  RBFs,  $\phi_{s_j}(\cdot)$  with support extent  $s_j$ ,  $j = 1, \dots, L$ , are associated with the  $j'$ -th level of volume pyramid, where  $j' = j$  when  $j \leq L'$  and  $j' = L'$  when  $j > L'$ . This hierarchical architecture enables a coarse-to-fine optimization that helps to avoid the local traps and improves the computational efficiency. Second, one lookup table is constructed beforehand for each support extent level of Wendland's RBFs to avoid the repeated function evaluations. Therefore, updating the deformation field with the RBF  $\phi_{s_j}(\cdot)$  in Eq. (3.6) requires only three subtractions, one table lookup, three multiplications, and three additions.

### 3.2.3 Correlation ratio

The image similarity function has strong influence on registration results. Statistical measurements such as MI [130, 131], NMI [132], and CR [133] have been used in multi-modal image registration [38, 87, 88]. These measurements are also adequate to unimodal image registration because they are robust to the noise, the different intensity contrast, and the intensity inhomogeneity. In this work, CR is adopted because it is superior in accuracy, efficiency, and robustness [37, 133, 134].

For the voxels of the same tissue in the target image, CR measures the intensity dispersion for their corresponding points in the source image. Let  $N$  be the number of voxels in the overlapping region  $\Omega$  between the source image  $I_s$  and the target image  $I_t$ . We divide the whole intensity range into  $N_B$  bins:  $B_i, i = 1, \dots, N_B$ . Let  $X_i$  denote a set of voxels in the region  $\Omega$  of the source image satisfying that their corresponding voxels in the target image have intensities belonging to the same intensity bin,  $B_i$ , as shown in Fig. 3.8. That is,

$$X_i = \{\mathbf{p} \mid \mathbf{p} \in \Omega, I_t(\mathbf{F}(\mathbf{p})) \in B_i\} , \quad (3.9)$$

where  $\mathbf{F}$  can be the spatial transformation function  $\mathbf{T}_r$ ,  $\mathbf{T}'_r$ ,  $\mathbf{T}_g$ , or  $\mathbf{T}$  in this work. Notice that  $N_1 + N_2 + \dots + N_{N_B} = N$ , where  $N_i$  is the number of voxels in  $X_i$ . Image similarity based on CR is calculated by

$$S_{CR}(I_t, I_s, \mathbf{F}) = 1 - \frac{1}{Var(I_s(\Omega))} \sum_{i=1}^{N_B} \frac{N_i}{N} Var(I_s(X_i)) , \quad (3.10)$$

where function  $Var(I_s(\Omega))$  and  $Var(I_s(X_i))$  evaluate the intensity variances of source image in  $\Omega$  and  $X_i$ , respectively. The voxels belonging to the same tissue generally have similar intensities. In the target image, therefore, the voxels having intensities within each intensity bin  $B_i$  very likely belong to the same tissue. If the source and target images are well aligned, voxels in  $X_i$  of the source image should also belong to the same tissue and hence the intensity variance of  $X_i$  should be small. Consequently, larger CR value indicates higher image similarity and hence better alignment.

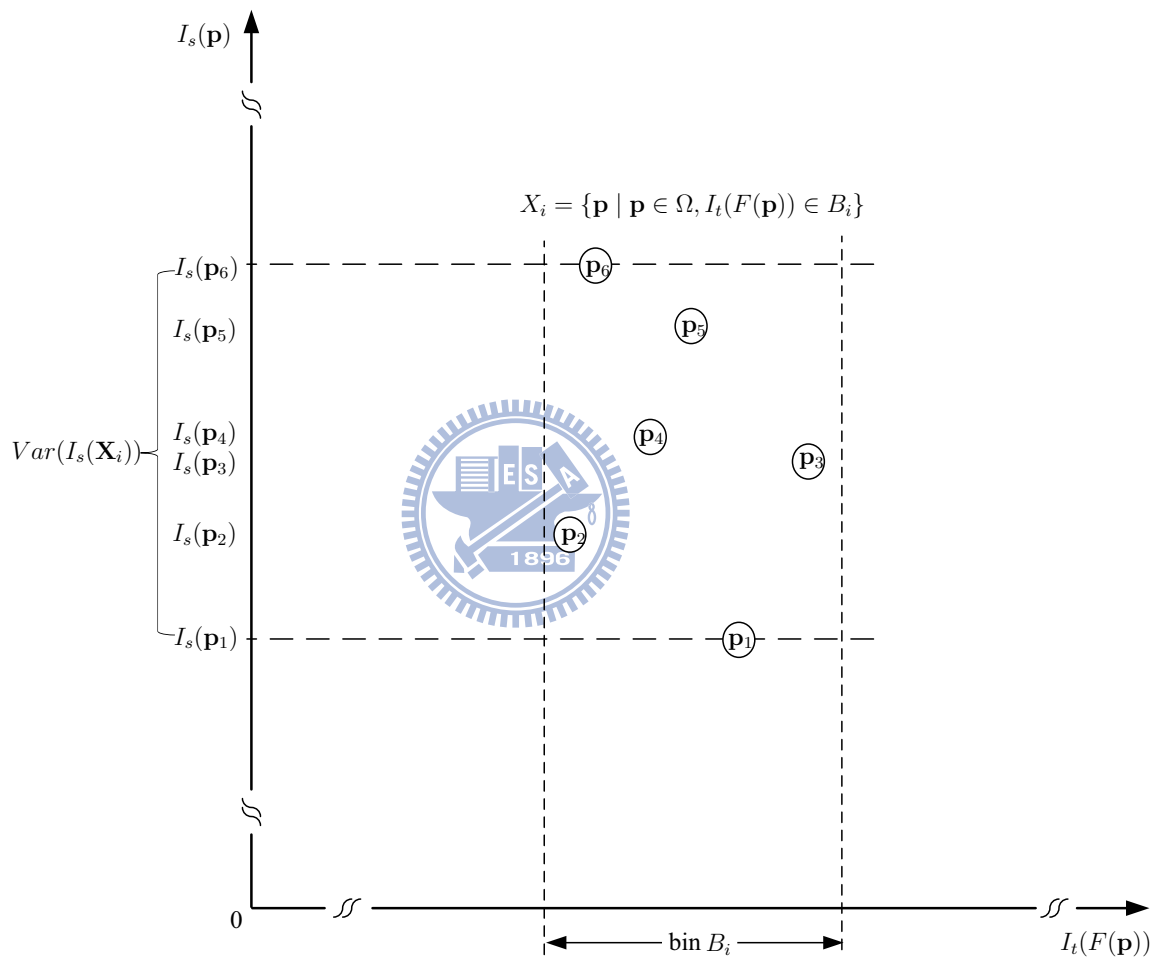


Figure 3.8: CR measures the intensity dispersion for the voxel set  $X_i$  in the source image which contains voxels with their corresponding points in the target image belonging to the same intensity bin  $B_i$ .

### 3.2.4 Evaluation of registration performance

This section introduces the methods used to evaluate the performance of the proposed affine and non-rigid registration algorithms, including the data sets and the approaches used for comparisons.

#### Registration algorithms for performance comparisons

The proposed affine registration method in BIRT was compared with Statistical Parametric Mapping 2 (SPM2) [83], Automated Image Registration version 5.2.5 (AIR5) [84], and FMRIB's Linear Image Registration Tool version 5.5 (FLIRT) [37]. The proposed non-rigid registration method in BIRT was compared with SPM2 [109], Hierarchical Attribute Matching Mechanism for Elastic Registration version 1.0 (HAMMER) [99], and Diffeomorphic Anatomical Registration Through Exponentiated Lie algebra (DARTEL) [135] in SPM5. BIRT was implemented in C++ and the programs of other algorithms were downloaded from their webpages. All registration experiments were executed on a PC with an AMD Opteron 1.4 GHz processor running Linux.

#### Data sets with known spatial mapping relation

T1-weighted head MR images acquired on a 1.5 Tesla GE MR scanner (3D-FSPGR pulse sequence; TR = 8.67 ms, TE = 1.86 ms, TI = 400 ms, NEX = 1, flip angle = 15°, bandwidth = 15.63 kHz) were used to construct simulation data in our experiments. Both the experiments of affine and non-rigid registration quantitatively measured the alignment accuracy and execution efficiency using two sets of images, each set with 30 images, with different spatial resolutions ( $256 \times 256 \times 124$ , voxel size =  $1.02 \times 1.02 \times 1.5 \text{ mm}^3$  and  $128 \times 128 \times 34$ , voxel size =  $2 \times 2 \times 5 \text{ mm}^3$ ). The registration error was evaluated by the average deviation of the estimated displacement vectors from the ground-truth ones,

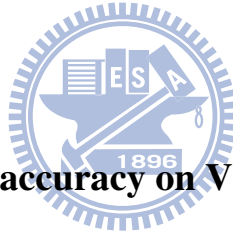
and the computational efficiency was compared according to the average execution time for registering an image pair.

Both the low- and high- resolution data sets applied in the experiment of affine registration were constructed by applying 30 times of affine transformation to each of the 30 MR images originally scanned, each time with random transformation parameters uniformly distributed within  $[-\pi/15, \pi/15]$  in radian,  $[-15 \text{ mm}, 15 \text{ mm}]$ ,  $[-0.05, 0.05]$ , and  $[-0.01, 0.01]$  for rotation, translation, scaling, and shearing, respectively. In the accuracy evaluation, each originally scanned MR image was regarded as the source image and the randomly transformed images were regarded as the target images, one at a time. The known random transformations provided the ground truths of corresponding points. Moreover, the rigid parameters of the ground truths with the same image set were also used to evaluate the accuracy of the rigid transformation estimated by the proposed method.

Three sets of source-target pairs of brain images, low and high resolution, with known deformation fields were constructed by applying SPM2, HAMMER, and DARTEL to non-linearly register 30 originally scanned MR images to a specified target image. We regarded the originally scanned images, the deformed images, and the deformation fields obtained by each registration method as the source images, the target images, and the ground truths of deformation, respectively, to evaluate the performance of other three algorithms. These materials facilitate the performance evaluation in a more objective way because the results are not biased toward a specific deformation type. The value to threshold the TDOG image can affect the performance of our non-rigid registration method, in terms of alignment accuracy and computational efficiency. Therefore, the constructed image pairs were also used to evaluate the influences of the thresholding level.

### Parameters of registration algorithms

In our experiments, the parameters of the compared methods were set to their default values, except AIR5. The intensity thresholds in AIR5 were set to the values which can exclude most of the background voxels and the scales of Gaussian kernels were determined by the best average accuracy. Two necessary preprocesses in HAMMER, brain extraction and tissue segmentation, were accomplished by Brain Extraction Tool (BET) version 2.1 [24] and FMRIB's Automated Segmentation Tool version 4.1 [34], which are parts of the FMRIB's Software Library [73]. For our affine and non-rigid methods, we set the FWHM of the Gaussian variances ( $\sigma_1^2, \sigma_2^2$ ) in TDOG to be (4 mm, 3 mm). The proposed non-rigid method applied BET2 to obtain brain masks and the RBF support extent was set to be 1.5 times of the subregion width.



### 3.2.5 Effects of registration accuracy on VBM analysis

This section introduces the experiment designed to investigate the influence of registration accuracy on the results of VBM analysis, including the construction of image groups and the criteria used for quantitative evaluation.

#### Construction of image groups

Six groups of GM images were generated by applying TPS transformation to deform a phantom GM image obtained from BrainWeb [136]. This avoids the segmentation step in VBM protocol [1, 11] such that the analysis results were not confounded by segmentation error. One normal group and five patient groups with different scales of volume differences were generated in this experiment, in which each group contained 30 subjects and all the images were  $157 \times 189 \times 156$  with voxel size  $1.0 \text{ mm}^3$ . Some related techniques for generating brain images with volumetric changes can be found in [137–139].

A total of 208 control points on the cortical surface of the cerebrum and cerebellum were selected to create MR brain images with or without volume difference in the cerebellum. Thirty of these points, referred as manipulating points, were identified on the exterior cortical surface of the cerebellum and were used to generate difference patterns with different scales. The other 178 points were used to fix anatomical structures, in which 38 points were selected from the interior surface of the cerebellum and 140 points were placed on the surface of the cerebral cortex. Fig. 3.9(a) illustrates the placement of these control points.

MR brain images of the normal subjects and patients were constructed by the following procedures. There are three steps in the generation of a patient image. First, we moved the manipulating points toward the cerebellum center. The displacement magnitude, that is, the volume difference scale, was parameter-controlled. Second, all the 208 control points were moved by a random vector with uniformly distributed magnitude within 2 mm in order to model the inter-subject structure variation. In the last step, we applied TPS transformation to construct a patient image according to these 208 control points. The construction procedure for a normal subject was the same as that for a patient, except the scale of volume difference was set to zero. In our experiments, the magnitude of the volume difference was uniformly distributed within different scales. Figs. 3.9(b) to (g) show the examples of the constructed images with difference scale of 0 mm (normal subject), 2 mm, 3 mm, 4 mm, 5 mm, and 6 mm, respectively.

### Accuracy assessment of VBM analysis

Two non-rigid registration algorithms, SPM2 and BIRT, were applied in the VBM analysis procedure. Normal subjects and patients were first registered to the GM phantom and the obtained deformation fields were used to modulate the deformed images for GM volume estimation [11]. The modulated images were convolved by a Gaussian kernel (FWHM = 4 mm) and the resulted images were statistically analyzed by using two-sample t-test.

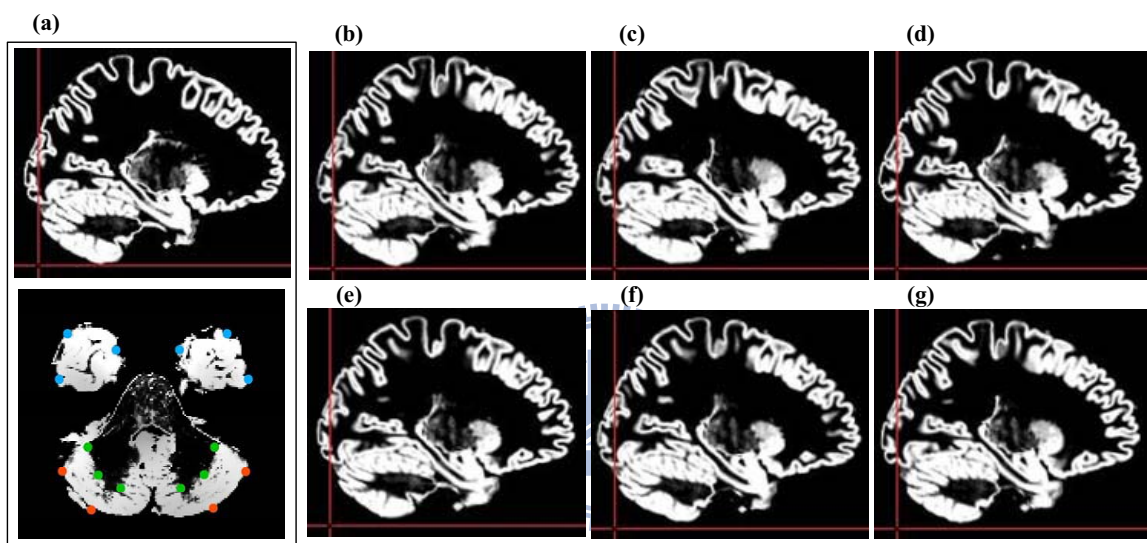


Figure 3.9: The construction of simulated images with different degrees of volume difference in the cerebellum. (a) All the images were constructed from the BrainWeb phantom GM (top) by using the TPS transformation. An inferior slice (bottom) of the phantom image illustrates the distribution of the control points. The red points placed on the exterior cortical surface of the cerebellum are used to generate volume difference patterns in the cerebellum. The green and the blue points distributed on the interior cortical surface of cerebellum and the cortical surface of cerebrum, respectively, are used to fix anatomical structures. The following figures illustrated the constructed MR images with different scales of volume differences: (b) 0 mm (normal subject), (c) 2 mm, (d) 3 mm, (e) 4 mm, (f) 5 mm, and (g) 6 mm.



We examined the VBM analysis procedure and defined proper ground truths for quantitative comparison. VBM structure analysis uses a registration method to normalize all subjects into the same stereotaxic space such that the corresponding structures are aligned and the structure variances between subjects can be removed. Therefore, the MR images transformed by a perfect registration method should be identical to the target (the GM phantom in this experiment). According to this viewpoint, the structural discrepancies discovered by the VBM analysis with a perfect registration method were the subtraction between the phantom image (that is, the perfectly registered images of normal subjects) and the phantom image modulated by the TPS deformation field (that is, the perfectly registered patient images). We applied Gaussian kernel (FWHM = 4 mm) to smooth the obtained ground truths of different scales of volume differences because the same kernel was applied to convolve the normalized and modulated subjects before the statistical analysis.

Correlation coefficient provides another quantitative measurement showing that whether accurate registration can facilitate VBM procedure to reveal more accurate statistical inferences. The voxels with higher values in the Gaussian smoothed ground truth indicate that there are larger volume differences between groups. For an accurate VBM analysis, the positions of these voxels in the t-map obtained from VBM results should have higher significance. Therefore, the higher correlation coefficient between the ground truth and the t-map implies that the VBM analysis can reveal regions with volume differences more accurately.

### 3.3 Experimental results

This section presents our experimental results, including the validation of registration performance and the investigation for the influences of registration accuracy upon VBM analysis.

### 3.3.1 Comparison of affine registration algorithms

Table 3.1 lists the performance comparisons for affine registration algorithms in terms of execution time and mean registration error calculated from all image voxels. For BIRT, the performance indices of the estimation for rigid parameters and the affine registration across four multi-resolution levels are listed in the table. The results of our experiment using high- (low-) resolution images showed that BIRT can achieve better accuracy than other algorithms in 76 (28) seconds, which is longer than that of SPM2 (SPM2 and AIR5) within 30 seconds. We can observe that the initial rigid transformation estimated by the proposed method is quite accurate, which was 1.46 (2.62) mm in the alignment of high- (low-) resolution images when only the rigid parameters of the ground truths are considered. It is apparent that the alignment error of the subsequent affine registration decreases rapidly from coarse to fine levels. Fig. 3.10 plots the sorted registration accuracy for all methods. The relatively low increasing rate indicates that BIRT can stably register brain image volumes. This figure also shows that the accuracy of about 95% cases was smaller than 0.1 mm by using the proposed method in this experiment. From Table 3.1 and Fig. 3.10, we can see that good spatial resolution of images can benefit the alignment accuracy for all compared methods at the expense of longer execution time. Nevertheless, BIRT was less sensitive to image resolution in contrast to other algorithms.

### 3.3.2 Determination of TDOG threshold

Fig. 3.11 illustrates the performance of our non-rigid method with respect to different settings of the Gaussian variances and TDOG threshold. Our experimental results showed that a smaller TDOG threshold, which increases the amount of structure information, generally resulted in better alignment accuracy at the expense of longer execution time. We can observe that both the alignment accuracy and computational efficiency of our non-rigid method converged when the threshold was smaller than  $-5$ . Gaussian variances also deter-

Table 3.1: Performance comparison of affine registration algorithms.

Performance criteria	BIRT							Affine				
	MDM	MSP overlap	MSP alignment	Rigid	Level 1	Level 2	Level 3	Level 4	FLIRT	SPM2	AIR5	
Error (mm) <sup>H</sup>	22.83	9.79 (9.09)	3.34 (1.62)	3.30 (1.46)	2.98	0.78	0.20	0.05	0.28	0.57	3.52	
Time (sec) <sup>H</sup>	-	27 (26.89)	45	51	51	53	76	364	442	51	131	
Error (mm) <sup>L</sup>	22.80	9.89 (9.83)	7.80 (3.35)	3.35 (2.62)	3.00	0.76	0.21	0.06	0.37	0.94	4.00	
Time (sec) <sup>L</sup>	-	1 (0.99)	9	12	12	13	28	43	120	21	7	

<sup>H</sup>256 × 256 × 124 images with voxel size 1.02 × 1.02 × 1.5 mm<sup>3</sup>; <sup>L</sup>128 × 128 × 34 images with voxel size 2 × 2 × 5 mm<sup>3</sup>

The upper and lower parts list the results of experiments using images with higher and lower spatial resolution, respectively. The first column lists the mean displacement magnitude (MDM) calculated from the spatial mapping relation of image pairs. The following seven columns list the averaged performance of the proposed BIRT method step-by-step, including the MSP overlapping, the alignment on the overlapped MSP, the rigid registration, and the affine registration across four multi-resolution levels. To demonstrate the accuracy of rigid transformation estimation, the numbers shown in the parentheses of the Error rows are the average alignment error when only the rigid parameters of the ground truths are considered. The average execution times used to calculate the TDOG images are listed in the parentheses of the Time rows. Note that the execution time of BIRT is accumulated for each step. The last three columns list the performance indices for FLIRT, SPM2, and AIR5.

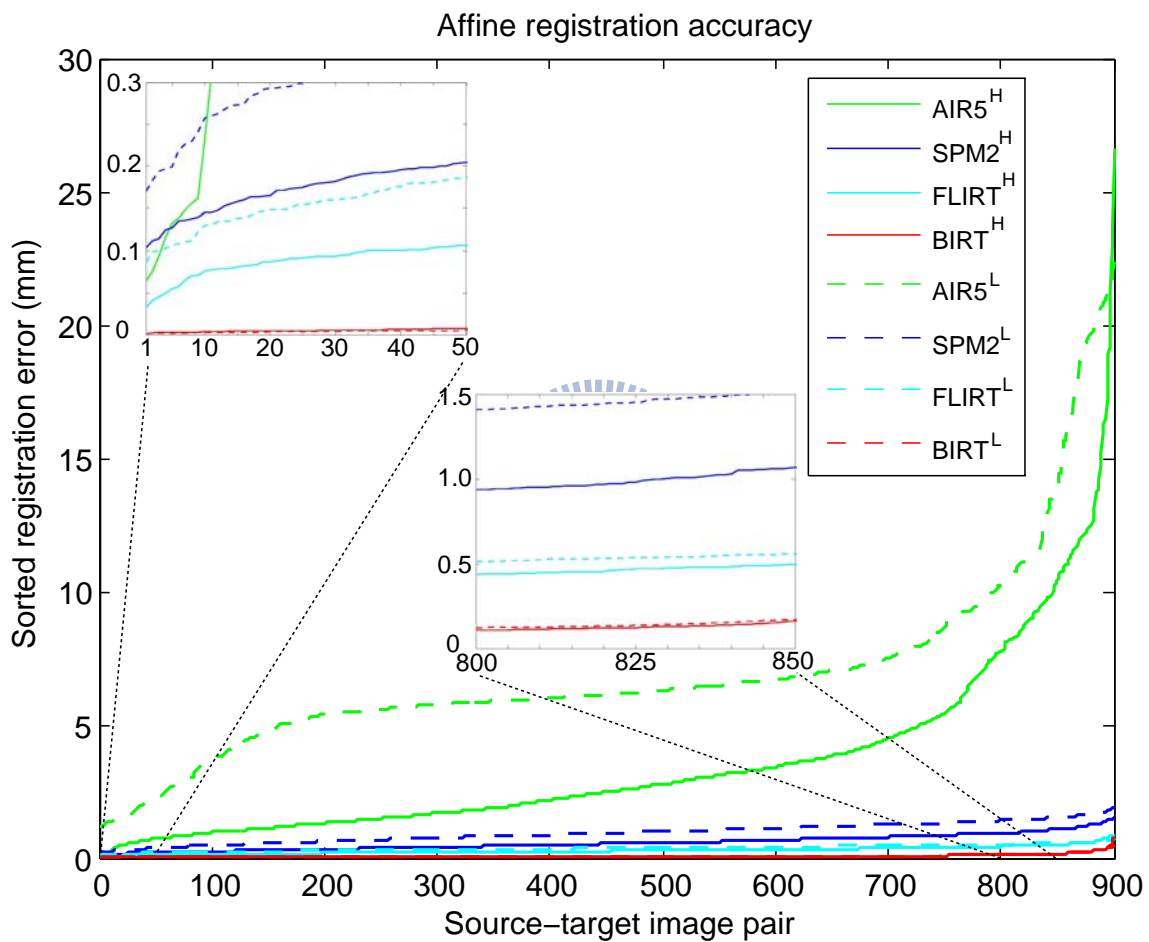


Figure 3.10: Comparison for the stability and accuracy of affine registration algorithms. The solid (dashed) lines show the results of experiments using  $256 \times 256 \times 124$  ( $128 \times 128 \times 34$ ) images with voxel size  $1.02 \times 1.02 \times 1.5$  ( $2 \times 2 \times 5$ )  $\text{mm}^3$ .

mine the amount of the structure information, coarse or fine. With the same thresholding level, it can be observed that the Gaussian variances providing coarse structure information commonly resulted in efficient registration process at the cost of high alignment error. Our experimental results also showed that the TDOG threshold had greater influences upon the registration performance for high-resolution images compared to that for low-resolution images. Compromising the registration accuracy and execution efficiency, we empirically determined the values of the FWHMs of the Gaussian variances  $\sigma_1^2$  and  $\sigma_2^2$  and the TDOG thresholding level to be 4 mm, 3 mm, and 0, respectively.

### 3.3.3 Comparison of non-rigid registration algorithms

Table 3.2 shows the evaluation results of BIRT (both the affine and non-rigid methods), SPM2, HAMMER, and DARTEL, in which the registration error was calculated from the voxels in the brain area. Both the experiments using high- and low- resolution images indicated that the registration error of BIRT steadily decreased across five deformation levels and achieved better accuracy than other algorithms in a short period of time. It can be observed that HAMMER, DARTEL, and BIRT performed better for the simulation images constructed by SPM2, compared to other data sets. The registration accuracy of BIRT at the second (third) deformation level was comparable to that of SPM2 with the high- (low-) resolution HAMMER and DARTEL data sets. The registration errors of HAMMER and BIRT for the images constructed by DARTEL were relatively higher than those for other data sets. On the other hand, in the experiments using high-resolution images, DARTEL did not perform as well for the alignments of the HAMMER data set as that of the SPM2 data set. Figure 3.12 illustrates the sorted accuracy for the experiments of all data sets. From the increasing rate of the profiles, we can see that the registration processes of all non-rigid methods were quite stable, except for SPM2 with the DARTEL data set and HAMMER with the low-resolution DARTEL data set. Our experimental results also indicated that the alignment of high-resolution images can achieve better accuracy at the expense of longer

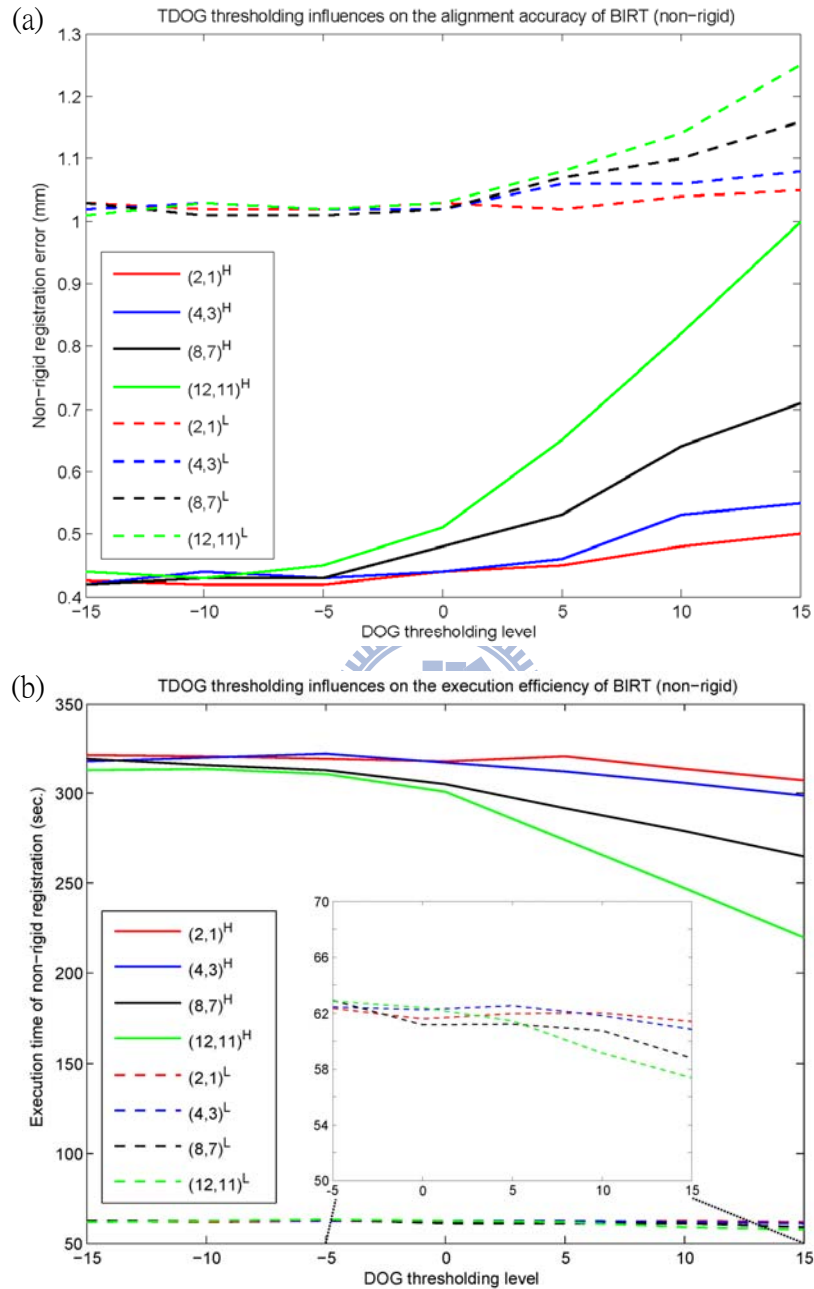


Figure 3.11: Influences of the thresholding value in TDOG upon the alignment accuracy and computational efficiency of our non-rigid registration method. Four different FWHM settings for the Gaussian variances were evaluated, including (12 mm, 11 mm), (8 mm, 7 mm), (4 mm, 3 mm), and (2 mm, 1 mm). The solid (dashed) lines show the results of experiments using  $256 \times 256 \times 124$  ( $128 \times 128 \times 34$ ) images with voxel size  $1.02 \times 1.02 \times 1.5$  ( $2 \times 2 \times 5$ )  $\text{mm}^3$ . Notice that the listed computational efficiency excluded the execution time of the required brain extraction and affine registration processes.

execution time compared to the registration of low-resolution data. Notice that the execution efficiency of DARTEL did not improve significantly for low-resolution images, possibly because DARTEL imports data with the same spatial resolution,  $1.5 \text{ mm}^3$ .

### 3.3.4 Effects of registration accuracy on VBM analysis

Fig. 3.13 shows the results of VBM analyses using two different registration algorithms, SPM2 and BIRT. It can be seen that the revealed patterns of volume difference ( $p < 0.005$ ) using BIRT are more focal in all cases. This figure also depicts that the VBM analysis using SPM2 non-rigid registration presents more false volume differences, particularly in the groups with larger difference scales. Comparing the ground truths with the VBM results of various thresholds for significance level, we obtained the receiver operating characteristics (ROC) of each registration algorithm. According to the ROC curves shown in Fig. 3.14, BIRT is superior to SPM2 with respect to sensitivity and specificity. Table 3.3 lists the correlation coefficients between the ground truths and the t-maps. Apparently, BIRT has higher values and thus is superior to SPM2 in all cases.

## 3.4 Discussion

The proposed affine method registers brain images by optimizing the twelve parameters subsequent to the estimation of the rigid transformation. Generally, rigid parameters are highly coupled and are critical to accurate registration results. Due to the use of structure information, BIRT can robustly estimate the orientation and position differences between MR images of the brains and the estimation error is small in our experiments. Therefore, the rigid transformation can provide a good initial for the optimization of all affine parameters, even if there are large orientation differences, as the example shown in Fig. 3.15. Both FLIRT and BIRT can find the correct orientation in such cases. However, FLIRT achieves

Table 3.2: Performance comparison of non-rigid registration algorithms.

Data set	MDM	BIRT									
		Affine	L1	L2	L3	L4	L5	SPM2	HAMMER	DARTEL	
SPM2 data <sup>H</sup>	17.44/-	2.74/113 (47)	2.67/116	1.55/121	0.77/141	0.33/242	0.19/321	-	0.59/8845 (3766)	0.52/12783 (2145)	
HAMMER data <sup>H</sup>	14.39/-	2.67/119 (33)	2.53/125	1.96/150	1.22/278	0.65/350	0.34/415	2.07/276	-	1.92/11480 (1950)	
DARTEL data <sup>H</sup>	14.49/-	2.86/114 (33)	2.02/119	1.86/141	1.60/251	1.12/311	0.78/367	2.26/298	1.01/8646 (3777)	-	
SPM2 data <sup>L</sup>	17.49/-	3.75/45 (8)	3.44/46	2.70/71	1.52/98	0.80/110	0.60/121	-	1.17/781 (135)	2.03/11273 (1011)	
HAMMER data <sup>L</sup>	13.39/-	2.95/43 (8)	2.82/43	2.64/64	2.05/84	1.36/94	1.03/102	2.02/194	-	2.15/11594 (933)	
DARTEL data <sup>L</sup>	15.49/-	2.91/32 (8)	2.16/32	2.04/51	1.94/69	1.70/78	1.45/85	2.42/186	2.23/595 (125)	-	

mm/sec. (sec.); <sup>H</sup>256 × 256 × 124 images with voxel size 1.02 × 1.02 × 1.5 mm<sup>3</sup>; <sup>L</sup>128 × 128 × 34 images with voxel size 2 × 2 × 5 mm<sup>3</sup>

The upper and lower parts show the results of experiments using images with higher and lower spatial resolution, respectively. For each part, the performance indices with the images constructed by SPM2, HAMMER, and DARTEL are listed from top to bottom. The first column lists the mean displacement magnitude (MDM) calculated from the spatial mapping relation of image pairs. The following six columns list the performance of the proposed BIRT method. The last three columns list the registration performance of SPM2, HAMMER, and DARTEL. The numbers before and after the slash are the registration error and the execution time, respectively. The numbers in parentheses show the preprocessing time if required. Note that the execution time of BIRT is accumulated for each step.



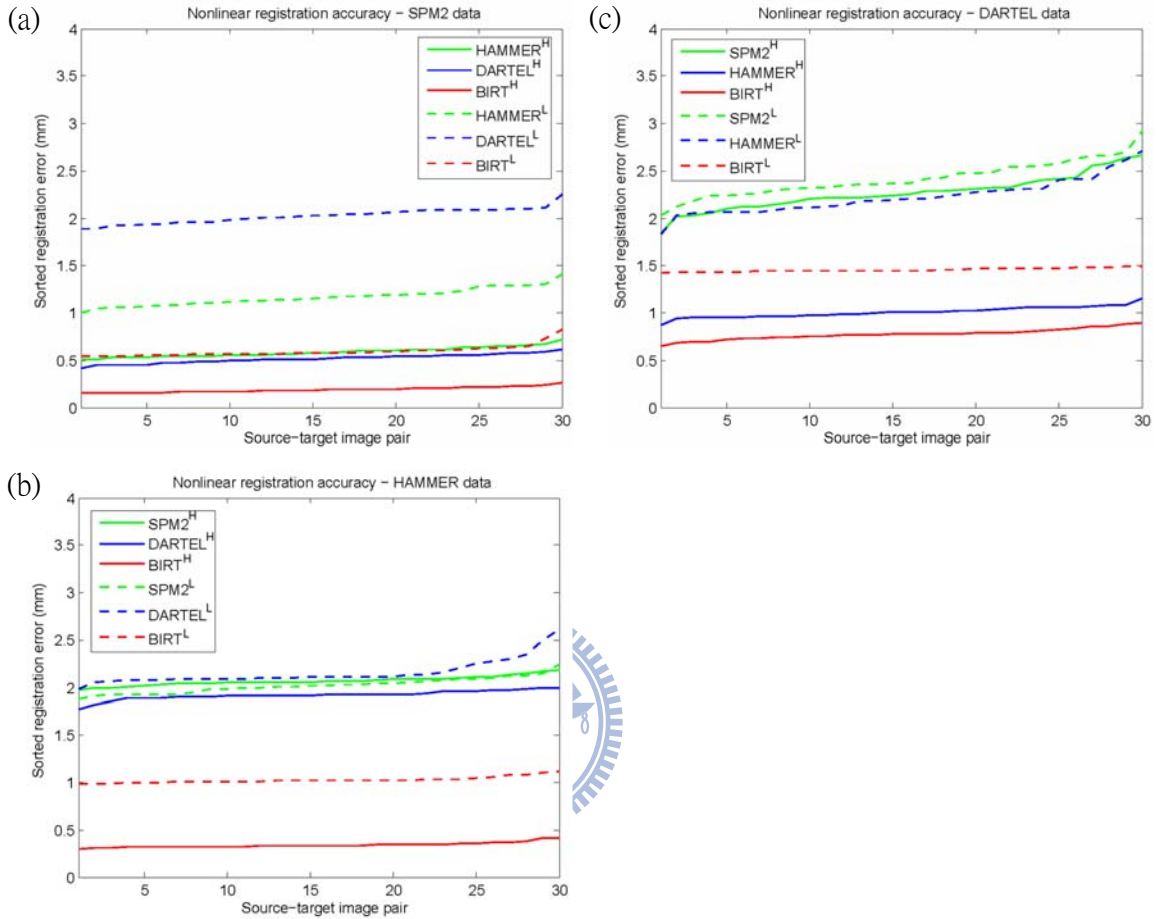


Figure 3.12: Comparison for the stability and accuracy of non-rigid registration algorithms with the simulated images constructed by (a) SPM2, (b) HAMMER, and (c) DARTEL. The solid (dashed) lines show the results of experiments using  $256 \times 256 \times 124$  ( $128 \times 128 \times 34$ ) images with voxel size  $1.02 \times 1.02 \times 1.5$  ( $2 \times 2 \times 5$ )  $\text{mm}^3$ .

Table 3.3: The correlation coefficients between the ground truths and the t-maps obtained from VBM analysis using BIRT and SPM2 methods

	Scale of volume difference				
	2 mm	3 mm	4 mm	5 mm	6 mm
<b>SPM2</b>	0.61	0.61	0.63	0.60	0.58
<b>BIRT</b>	0.65	0.67	0.74	0.74	0.74

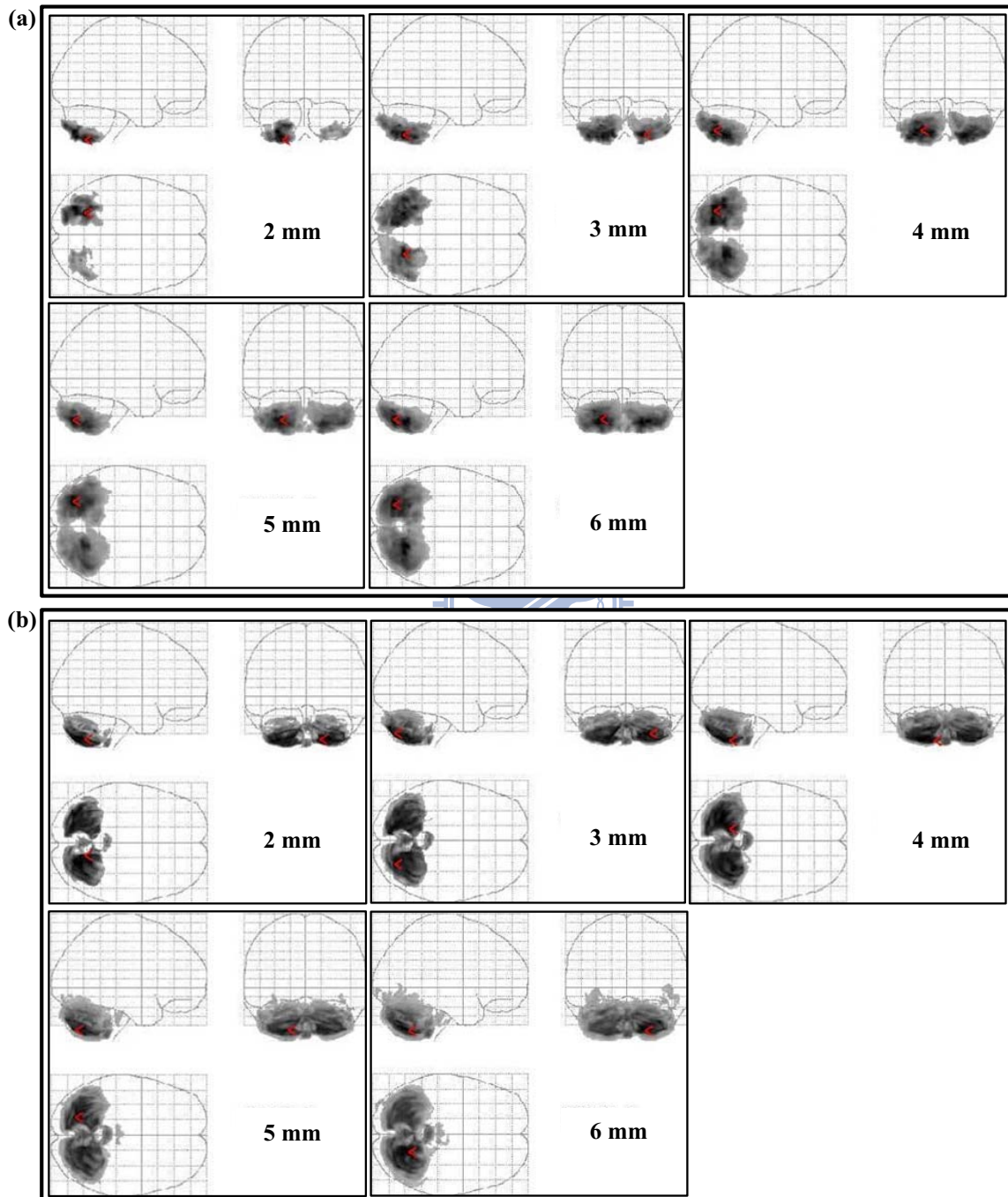


Figure 3.13: The VBM structural analysis results ( $p < 0.005$ ) using simulated images with different scales of volume differences, in which the image normalization was performed by using (a) BIRT and (b) SPM2.

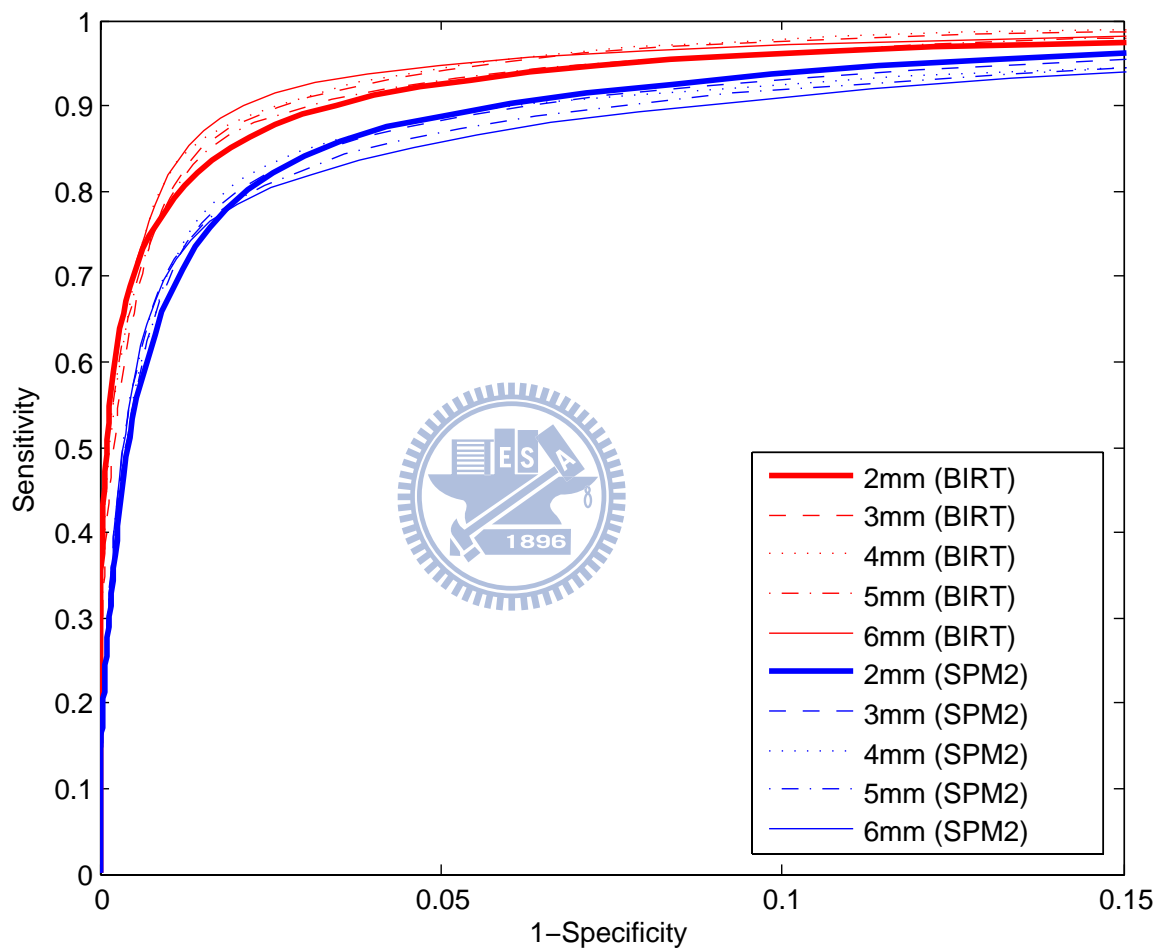


Figure 3.14: The ROC curves of the simulated VBM structural analyses, in which the red and blue curves represent the results with different scales of volume differences from 2 mm to 6 mm using BIRT and SPM2, respectively.

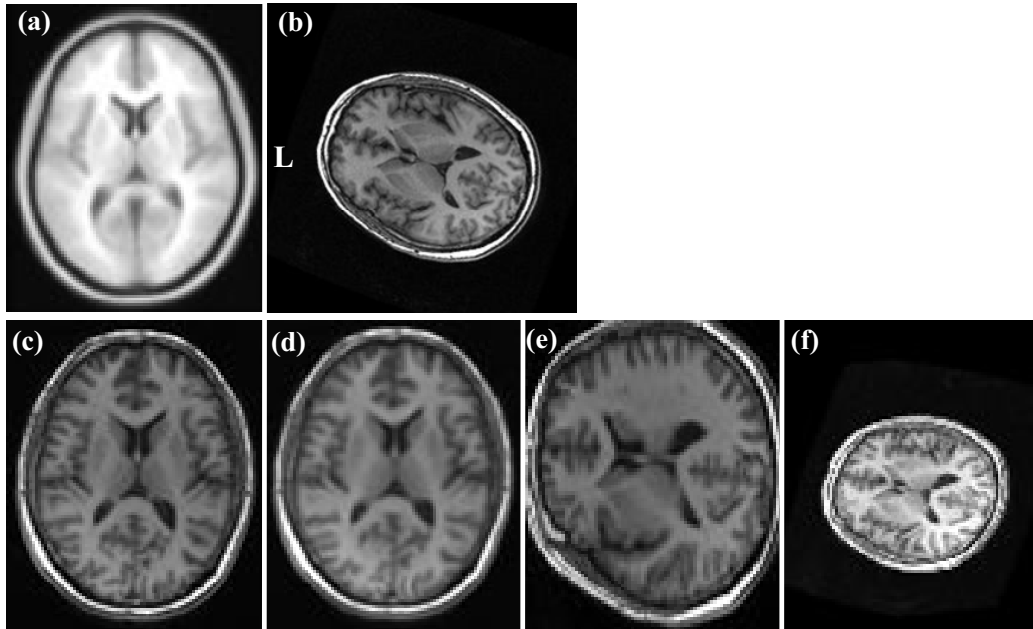


Figure 3.15: The affine registration for brains with large orientation difference. (a) The ICBM-152 brain template used as the target image. (b) A T1-weighted image used as the source image. The affine-registered result using (c) BIRT, (d) FLIRT, (e) SPM2, and (f) AIR5.

this goal by searching in a large space of parameters at the expense of longer execution time than that of BIRT. Experimental results showed that the proposed affine method performs well in terms of accuracy, efficiency, and stability.

The determination of brain MSP is an essential step in our affine registration algorithm. In general, previously published methods [126–128] can be applied to locate the MSP in the proposed procedure. In this work, we propose a new MSP location method based on the TDOG image. Because of the structural properties of MSP revealed in the TDOG image, the orientation of MSP can be estimated by a closed-form solution and the further refinement is very time efficient. As shown in Table 3.1, the major computational burden of our method is from the Gaussian filtering procedure in the TDOG image computation. Because the TDOG image is necessary for the subsequent non-rigid registration process, the proposed MSP location method only slightly increases the whole computation with the

centroid estimation, the PCA computation of  $3 \times 3$  matrices, and the following optimization procedure. Moreover, the TDOG image and the PCA procedure can reduce the influence of noise and intensity inhomogeneity. Even when the neck and shoulder regions are included in the images and could largely bias the estimation of brain centroid, the MSP can also be robustly located by the proposed affine method, as the example shown in Fig. 3.16.

Extracting the brain region beforehand is usually beneficial to registration accuracy because the inter-subject variation of non-brain structures are relatively large [36]. Nevertheless, brain extraction is not included as a necessary step in the proposed affine method for the generality of methodology. Notice that the estimation to brain orientation in the proposed affine method is only adequate to the registration of brain images because it uses the information specific to brain structures. Therefore, it is not a solution to general rigid registration problems.

The non-rigid registration method in BIRT applies Wendland's RBFs to model image deformation field hierarchically, in which all RBFs are adaptively deployed near the important structures of brains. Execution efficiency is an important issue for the alignment of 3-D images, especially for those applications which apply registration intensively, such as VBM analysis. Some characteristics of the proposed method can greatly reduce the computational complexity. First, the adaptive placement decreases the number of the required RBFs. Second, coefficient estimation for one RBF at a time can greatly reduce the parameter search space and hence accomplish the registration task rapidly. In this way, the structure topology is always preserved in the modeling of deformation fields. Third, because of the compact support property of the Wendland's RBFs, there are only a few functions involved in the transformation calculation for each image point. Fourth, some implementation skills, such as the use of pyramid images and the lookup tables of the RBFs, are also quite beneficial to further improve the efficiency of image registration. Experimental results demonstrated that BIRT can accurately align brain images in a relatively short period of time compared with SPM2, HAMMER, and DARTEL.

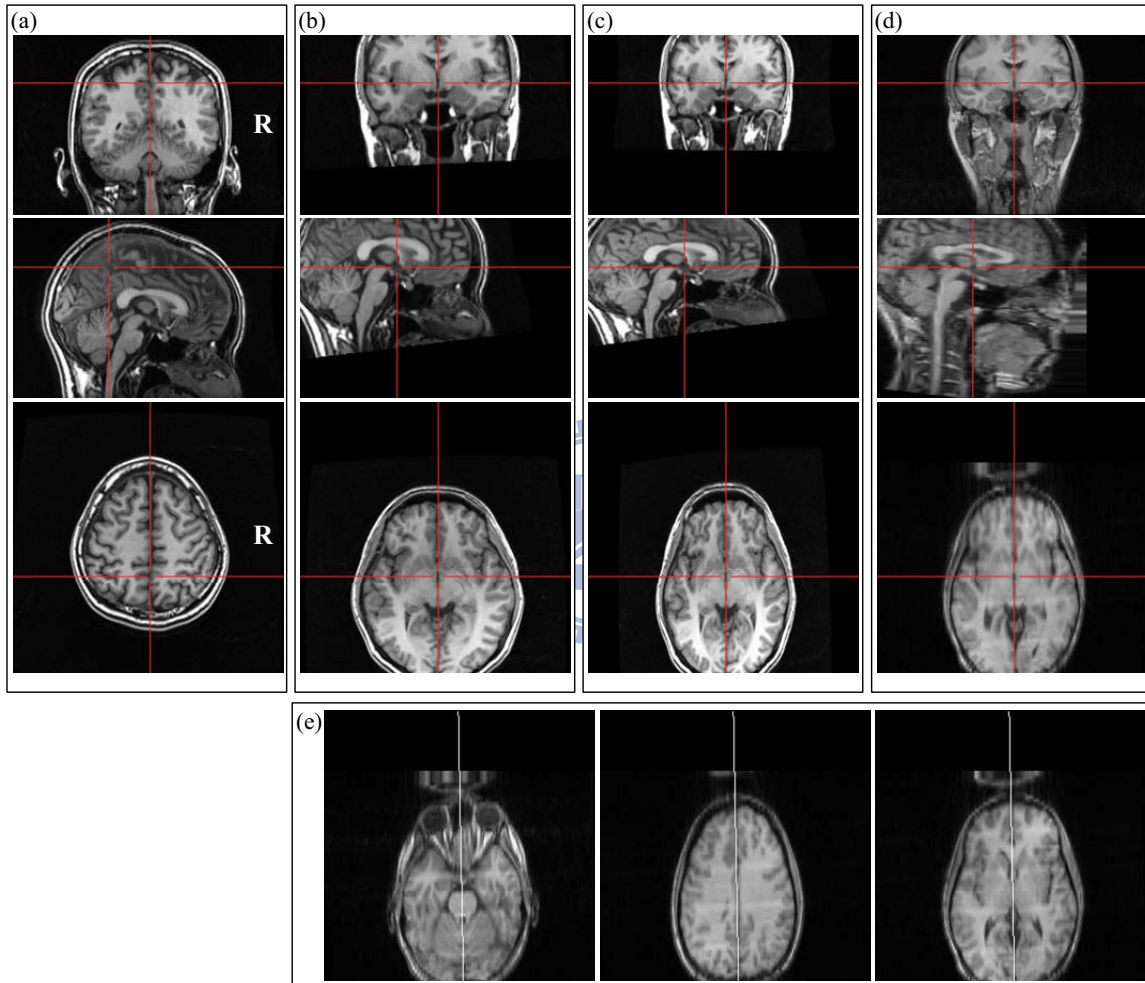


Figure 3.16: Affine registration for the brain images which include the neck regions and partial brain tissues are out of the field of view. (a) Source image. (b) Source image transformed using the estimated rigid parameters. (c) Affine registered source image. (d) Target image. (e) The estimated MSP of (d).

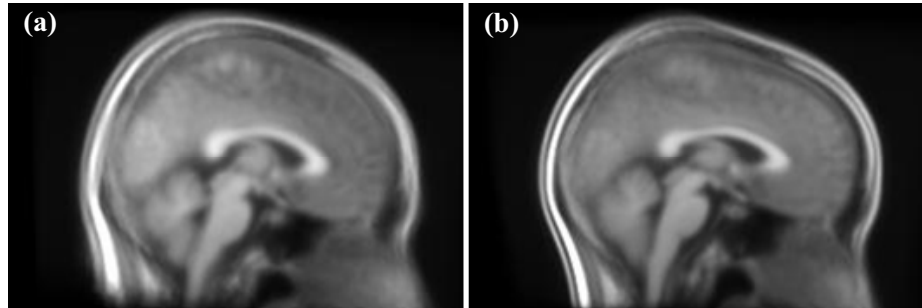


Figure 3.17: Regularization degree of non-rigid registration influences the sharpness of mean alignment results. Generally, highly regularized registrations result in sharp mean image, (b), compared to that of less regularized alignments, (a). SPM2 was utilized in this example for the non-rigid registrations of 57 T1-weighted MR images.

This work evaluated the performance of non-rigid registration techniques in an objective way which avoided the drawbacks of validation methods using the mean image averaged from alignment results and using the materials constructed by landmark-based transformation. The evaluation of registration performance utilizing landmark-based transformation identifies a set of corresponding anatomical landmarks between brains by experts and quantify the accuracy of alignment results. This approach requires manual selection of landmarks and needs several experts to eliminate the subjective factor. Therefore, it is time-consuming and the landmark identification is always prone to errors. Another extensively adopted validation approach registers images to a specified target and evaluates the sharpness of the averaged results. However, the sharpness of average image may not a good criterion used to measure the accuracy of a registration technique. Firstly, the regularization degree of non-rigid registration can influence the obtained result and less regularized alignments generally produce a clear mean image, as shown in Fig. 3.17. Secondly, a clear average image could not imply that a registration technique is accurate, as the example shown in Fig. 3.18. In this work, we applied the compared methods to generate image pairs with known deformation fields. These materials facilitated objective performance evaluation because the results were not biased toward a specific deformation type.



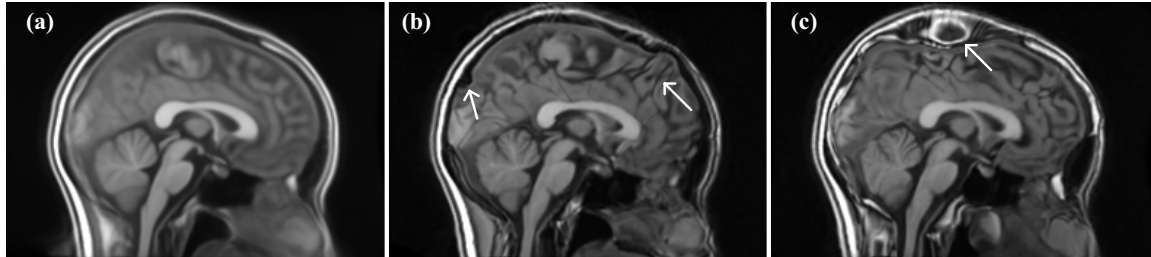


Figure 3.18: A sharp image averaged from non-rigid alignment results, (a), could not imply accurate registration, (b) and (c). Automated Registration Tool [123] was utilized in this example for the non-rigid registrations of 57 T1-weighted MR images.

The spatial normalization transforming MR brain images into the same stereotaxic space for statistical comparison is an essential step in VBM analysis. It is commonly believed that the registration accuracy greatly affects the analysis results. However, to the best of our knowledge, there is still no quantitative study addressing this issue. Deviation of the VBM analysis was majorly contributed by the smoothing, the voxel-wise statistics, and the alignment errors of image registration. In this work, we constructed MR images of subjects with or without volume differences to investigate the registration errors upon the accuracy of VBM analysis. From the results of the well-controlled experiments, we conclude that an accurate registration method can facilitate VBM analysis to precisely report the structure differences between subject groups, in terms of both sensitivity and specificity.

BIRT can also be applied to register images of different modalities other than T1-weighted MR images. Our affine method is applicable to the alignment of brain images in which the MSP and CC have sufficiently large intensity contrast with the neighboring tissues. Additional preprocessing is required to invert the intensity contrast of brain tissues if the intensities in the MSP region are higher than those of CC. On the other hand, the proposed non-rigid registration method is general and suitable for the registration of images with similar structures. Figs. 3.19 demonstrates an inter-subject alignment between T1-weighted and T2-weighted images. Intra-subject registration of T1-weighted and non-diffusion-weighted images (T1-weighted and CT images) is shown in Fig. 3.20 (Fig. 3.21).



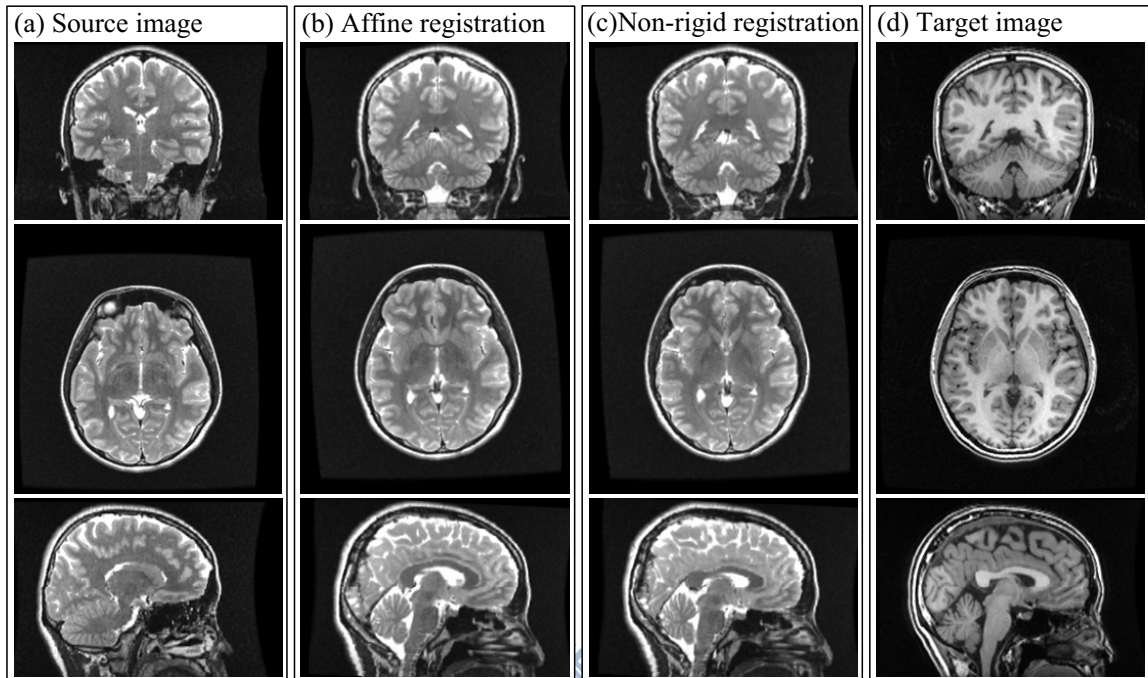


Figure 3.19: Inter-subject non-rigid alignment between T1-weighted and T2-weighted brain images using the proposed BIRT methods. (a) T2-weighted brain image as the source image. (b) Source image after the affine registration. (c) Source image after the non-rigid registration. (d) T1-weighted brain image as the target image.

The intra-subject registration between non-diffusion-weighted and T1/T2-weighted images are frequently applied for the structure analysis of diffusion images, such as the works of [140, 141]. Moreover, Fig. 3.22 shows that the proposed registration techniques can also well align the brains of drosophilas, which were acquired using confocal imaging.

In conclusion, we have proposed image registration, affine and non-rigid, which utilize the structure information derived from image derivatives. Experimental results indicated that the proposed BIRT methods can rapidly align brain structures with high accuracy compared to several other existing algorithms. An experiment using MR image groups with or without volume differences was also conducted to demonstrate that accurate registration can improve VBM analysis, in terms of both the sensitivity and the specificity.

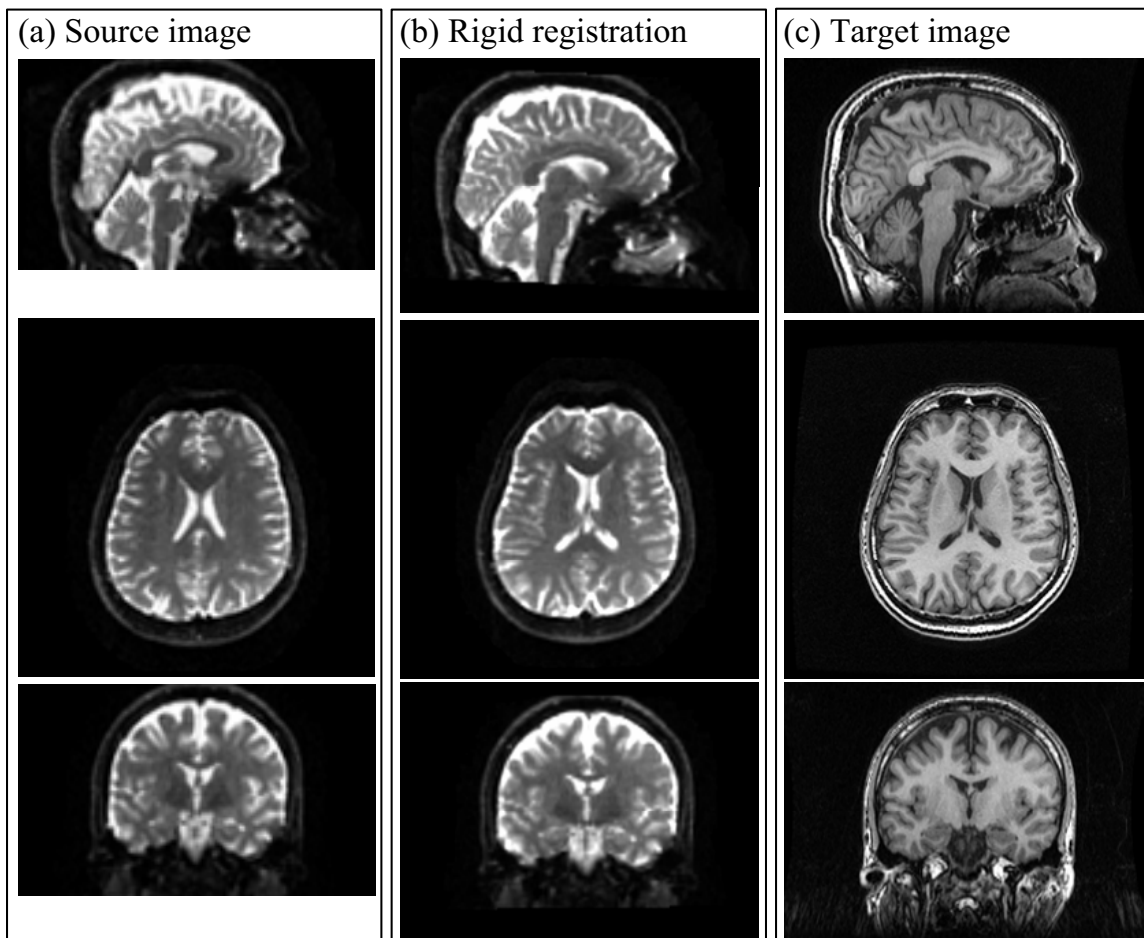


Figure 3.20: Intra-subject rigid alignment between non-diffusion-weighted and T1-weighted images using the proposed affine method. (a) Non-diffusion-weighted image as the source image. (b) Source image after the rigid registration. (c) T1-weighted brain image as the target image.

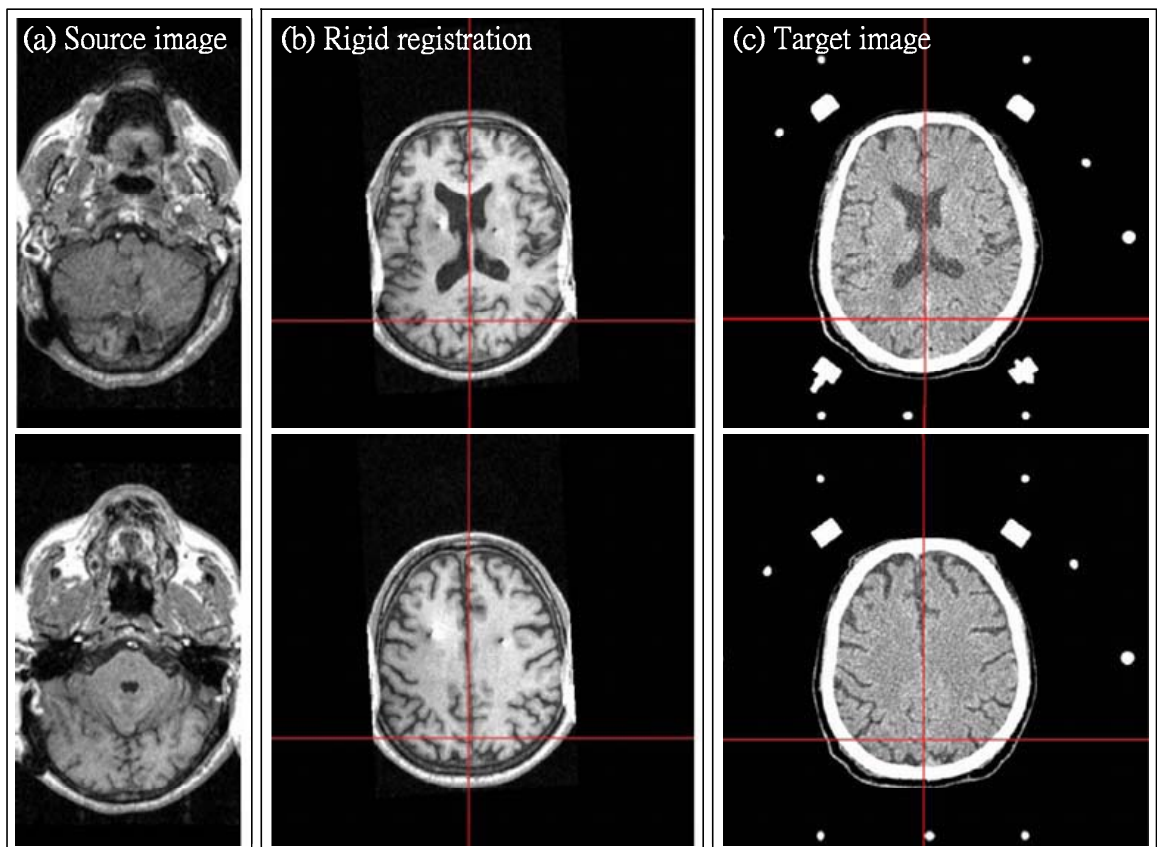


Figure 3.21: Intra-subject rigid alignment between T1-weighted and CT images using the proposed affine method. (a) T1-weighted image as the source image. (b) Source image after the rigid registration. (c) CT image as the target image. The images were provided by Chang Gung Memorial Hospital.

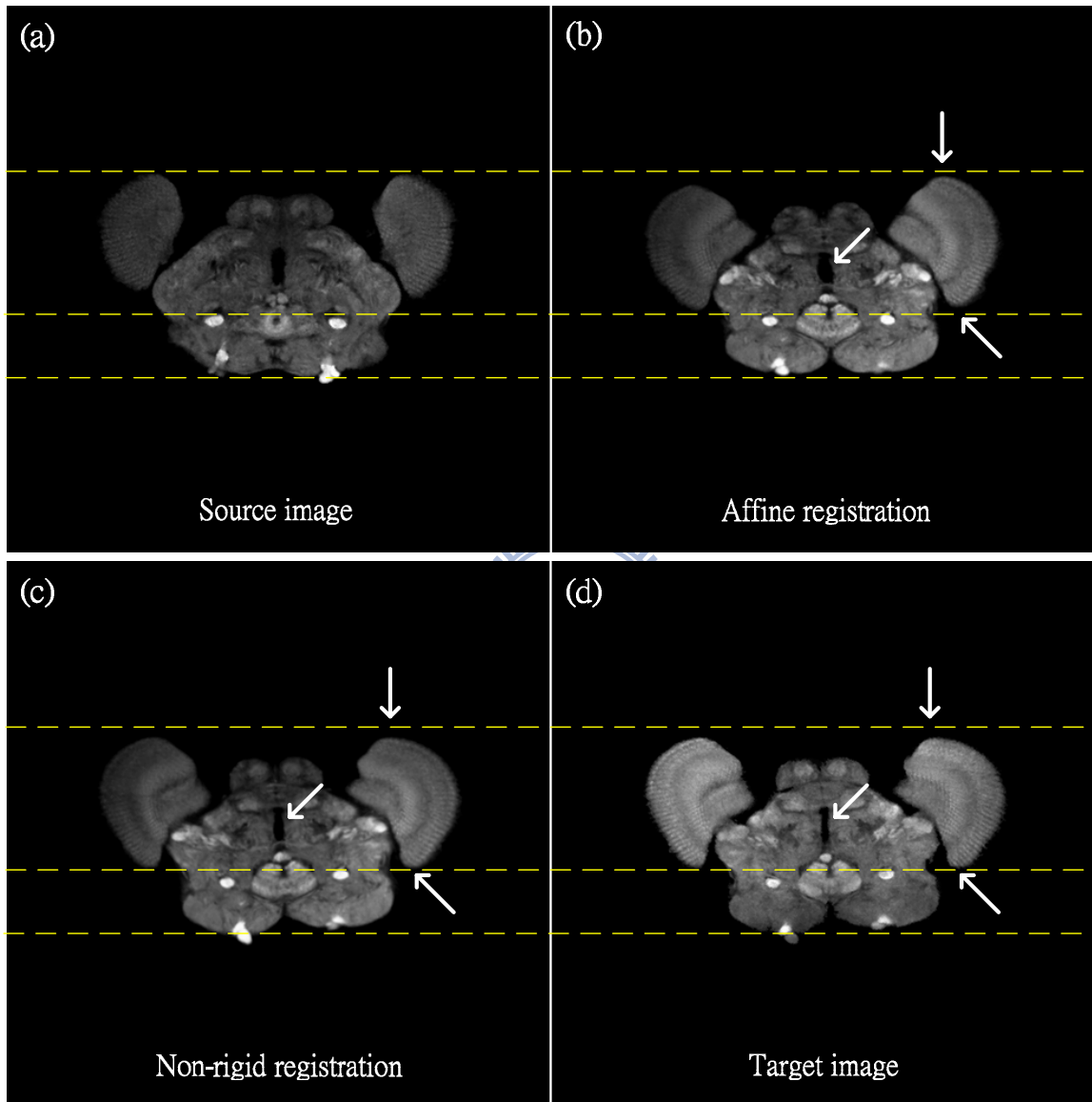


Figure 3.22: Registration of drosophila brains using the proposed BIRT methods. (a) Source image. (b) Source image after the affine registration. (c) Source image after the non-rigid registration. (d) Target image. The arrows in (b) and (c) indicate those areas with stepwise improved alignment refined by the affine and non-rigid methods. The confocal images of drosophila brains were provided by Brain Research Center, National Tsing Hua University, Taiwan.

## **Chapter 4**

# **White matter abnormalities between bipolar I and II disorders**



## 4.1 Background and related works

In the Diagnostic and Statistical Manual of Mental Disorders (text revision; DSM-IV-TR), bipolar disorder is categorized into bipolar I, bipolar II, cyclothymia, and bipolar disorder not otherwise specified subtypes according to the clinical characteristics. Findings of aberrant neuroanatomy from neuroimaging studies on bipolar patients are sometimes inconsistent and even conflicting [5]. One possible origin is the pathophysiological heterogeneity manifested in bipolar patients [28, 31]. Recent neuropsychological study reported that bipolar I patients manifested more cognitive dysfunction in verbal learning, recall, recognition, and set-shifting compared to bipolar II patients [31]. However, whether bipolar subtypes have distinct neural substrates remains unclear.

Diffusion tensor imaging allows us to detect abnormal white matter integrity by quantifying the degrees of fiber alignment, such as fractional anisotropy (FA) indices [9]. Previous studies using diffusion tensor images reported the white matter impairments of bipolar patients majorly in frontal areas [28, 142–144]. Bruno et al. indicated the fiber alterations of bipolar patients in bilateral prefrontal, middle temporal, and middle occipital regions [7]. Recently, Mahon et al. reported that bipolar patients showed fiber impairments in the pontine crossing tract, corticospinal/corticopontine tract, and thalamic radiation fibers [8]. To date, most of the bipolar studies of diffusion tensor imaging adopted the region-of-interest (ROI) approaches [28, 142–144]. Compared with ROI-based methods, voxel-wise whole-brain analysis is advantageous when the locations of abnormalities are difficult to predict and thus is more adequate to pathological investigation of bipolar disorders [7, 8].

The goal of this study was to investigate whether bipolar I and bipolar II patients manifest different patterns of white matter abnormalities. FA indices of the recruited bipolar I and II patients were compared in a voxel-wise manner, without specifying ROIs. We hypothesized that white matter impairments exhibited in patients with bipolar I might be more related to cognitive functioning in contrast to patients with bipolar II.

## 4.2 Materials and methods

### 4.2.1 Participants

Twenty-seven right-handed bipolar patients (bipolar I = 14, bipolar II = 13) were recruited from the outpatients of Taipei Veterans General Hospital. Clinical characteristics were diagnosed by two independent psychiatrists according to DSM-IV-TR. All patients, except one bipolar I and two bipolar II subjects, took a range of medications, including lithium, anticonvulsants, antidepressants, and antipsychotics. The mood symptoms were rated before image acquisition using the Young Mania Rating Scale (YMRS), 17-item Hamilton Rating Scale for Depression (HAM-D17), Montgomery Åsberg Depression Rating Scale (MADRS), and Hamilton Anxiety Rating Scale (HARS). The demographic and clinical characteristics of all participated patients are listed in Table 4.1. Twenty-one right-handed healthy participants without history of psychiatric or neurological disorders were recruited from the community through advertisements. All the healthy subjects were evaluated using the Mini-International Neuropsychiatric Interview before the experiments to exclude those with psychiatric morbidity. No subject had history of substance misuse or abuse and everyone provided written informed consent to participate in the study according to the guidelines approved by the Institutional Review Board of Taipei Veterans General Hospital.

### 4.2.2 Neuropsychological assessments

The neurocognitive functions of all participants were assessed using a neuropsychological test battery, including the Wisconsin Card Sorting Test for measuring the problem-solving ability, cognitive flexibility, and response maintenance; the Word List Test for evaluating the working memory capacity; and the Test for Attention Performance (version 1.02) for assessing the attention function. The assessment results are listed in Table 4.2.

Table 4.1: Demographic characteristics

Characteristic	Bipolar I patients (n=14)	Bipolar II patients (n=13)	Healthy subjects (n=21)
Age, years (mean/std)	35.6 / 10.9	35.1 / 9.8	38.3 / 11.9
Gender, n (male/female)	7 / 7	2 / 11	8 / 13
Handedness, n (left/right)	14 / 0	13 / 0	21 / 0
Education, years (mean/std)	13.7 / 2.0	14.6 / 2.1	15.0 / 3.2
Duration of illness, years (mean/std)	7.3 / 5.7	9.4 / 7.4	-
(Hypo-)manic episodes (mean/std)	3.8 / 2.8 <sup>a</sup>	2.8 / 2.5 <sup>b</sup>	-
(Hypo-)manic/depression ratio (mean/std)	1.0 / 0.6 <sup>c</sup>	0.6 / 0.5 <sup>d</sup>	-
YMRS (mean/std)	0.9 / 1.6	2.0 / 2.7	-
HAMD17 (mean/std)	6.7 / 5.8	9.5 / 6.6	-
MADRS (mean/std)	5.6 / 5.7	11.5 / 9.0	-
HARS (mean/std) <sup>e</sup>	5.1 / 4.7	10.6 / 7.9	-
Medications, n			
Lithium <sup>f</sup>	2	0	-
Anticonvulsants <sup>g</sup>	12	10	-
Antidepressants <sup>h</sup>	12	10	-
Antipsychotics <sup>i</sup>	1	1	-

YMRS: Young Mania Rating Scale; HAMD17: 17-item Hamilton Rating Scale for Depression; MADRS: Montgomery Åsberg Depression Rating Scale; HARS: Hamilton Anxiety Rating Scale; std: standard deviation

<sup>a</sup>Manic episodes; <sup>b</sup>hypomanic episodes; <sup>c</sup>manic/depression ratio; <sup>d</sup>hypomanic/depression ratio; <sup>e</sup>significant difference between bipolar I and II patients ( $z=2.32$ ,  $p=0.02$ ); <sup>f</sup>Lithium, lithium carbonate, lisdin; <sup>g</sup>Lamictal, lamotrigine, rivotril, depakine, depakine chrono, adivan, topiramate; <sup>h</sup>Wellbutrin, seroquel, crispan, stinnox, lexapro, effexor XR; <sup>i</sup>Abilify

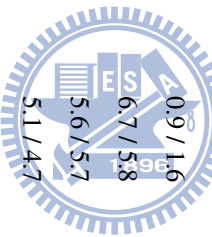




Table 4.2: Performance of neuropsychological tests

Tests	Bipolar I patients	Bipolar II patients	Healthy subjects
<b>WCST</b>			
Perseverative errors (%)	12.6 (5.3)	14.7 (10.2)	9.1 (3.8)
Perseverative response (n)	15.9 (9.1)	18.8 (16.7)	9.8 (6.2)
Non-perseverative errors (n)	23.6 (21.4)	20.8 (17.5)	11.8 (7.9)
Failure to maintain set (n) <sup>a</sup>	0.9 (0.8)	0.5 (1.1)	0.7 (1.1)
<b>Word list</b>			
Short-delayed recall (n)	7.9 (2.7)	8.8 (1.6)	9.2 (2.8)
Recognition (n)	23.1 (1.1)	23.2 (0.8)	22.4 (5.5)
Retention ( Learning slope (n)	4.5 (2.0)	4.2 (1.3)	3.6 (1.6)
<b>Attention</b>			
Go/no-go (ms)	496.2 (68.2)	488.7 (63.7)	485.8 (59.2)
Divided attention (sounds) (ms)	590.1 (99.2)	597.4 (70.4)	851.3 (116.4)
Divided attention (squares) (ms) <sup>b</sup>	938.1 (145.6)	926.3 (77.7) <sup>b</sup>	604.4 (79.3)
mean (standard deviation)			

WCST: Wisconsin Card Sorting Test; WLT: Word List Test; TAP: Test for Attention Performance

<sup>a</sup>Significant difference between bipolar I and II patients ( $z=-2.00$ ,  $p=0.05$ )

<sup>b</sup>Significant difference between bipolar I/II patients and healthy subjects ( $z=-2.25$ ,  $p=0.03/z=-2.36$ ,  $p=0.02$ )

### 4.2.3 Image acquisition and processing

All subjects were scanned on a GE Signa EXCITE 1.5T system. A total of fourteen diffusion tensor images were acquired for each subject (spin-echo EPI, TR = 17000 ms, TE = 69.2 ms, matrix size =  $128 \times 128 \times 70$ , voxel size =  $2.03 \times 2.03 \times 2.2 \text{ mm}^3$ ), including thirteen images obtained by using diffusion gradients applied along thirteen nonparallel directions ( $b = 900 \text{ s/mm}^2$ ) and one image without diffusion weighting ( $b = 0 \text{ s/mm}^2$ , B0). One additional T1-weighted image was acquired for each subject to provide a high resolution anatomical reference (3D-FSPGR, TR = 8.67 ms, TE = 1.86 ms, matrix size =  $256 \times 256 \times 124$ , voxel size =  $1.02 \times 1.02 \times 1.5 \text{ mm}^3$ ).

Fig. 4.1 shows the image processing protocol used for the analysis of diffusion tensor images. To reduce the head motion as well as the geometric distortion caused by eddy currents, diffusion tensor images of each subject were first aligned to the B0 image using affine registration. The aligned diffusion tensor images were then used to calculate the FA maps using FMRIB's Diffusion Toolbox<sup>1</sup>. The white matter regions in T1-weighted images were segmented using FMRIB's Automated Segmentation Tool<sup>1</sup> after removing the non-brain tissues [27]. A customized white matter template was constructed by averaging the white matter images of all participants nonlinearly registered to a white matter template built from the local population. For each subject, a deformation field was estimated by combining the results of rigid registration between the B0 and T1 images and non-rigid registration between the segmented white matter image and customized white matter. Subsequently, the FA map of each subject was spatially normalized to the customized white matter space by applying the individual deformation field. Before statistical comparison, all the normalized FA maps were smoothed by a Gaussian kernel with 6-mm full width at half maximum, which was determined according to the diameter of major fiber tracts in the human brain [7, 145]. In addition, the software of Brain Image Registration Tools (BIRT) was adopted to perform the affine and non-rigid registrations in this work [146].

<sup>1</sup><http://www.fmrib.ox.ac.uk/fsl>

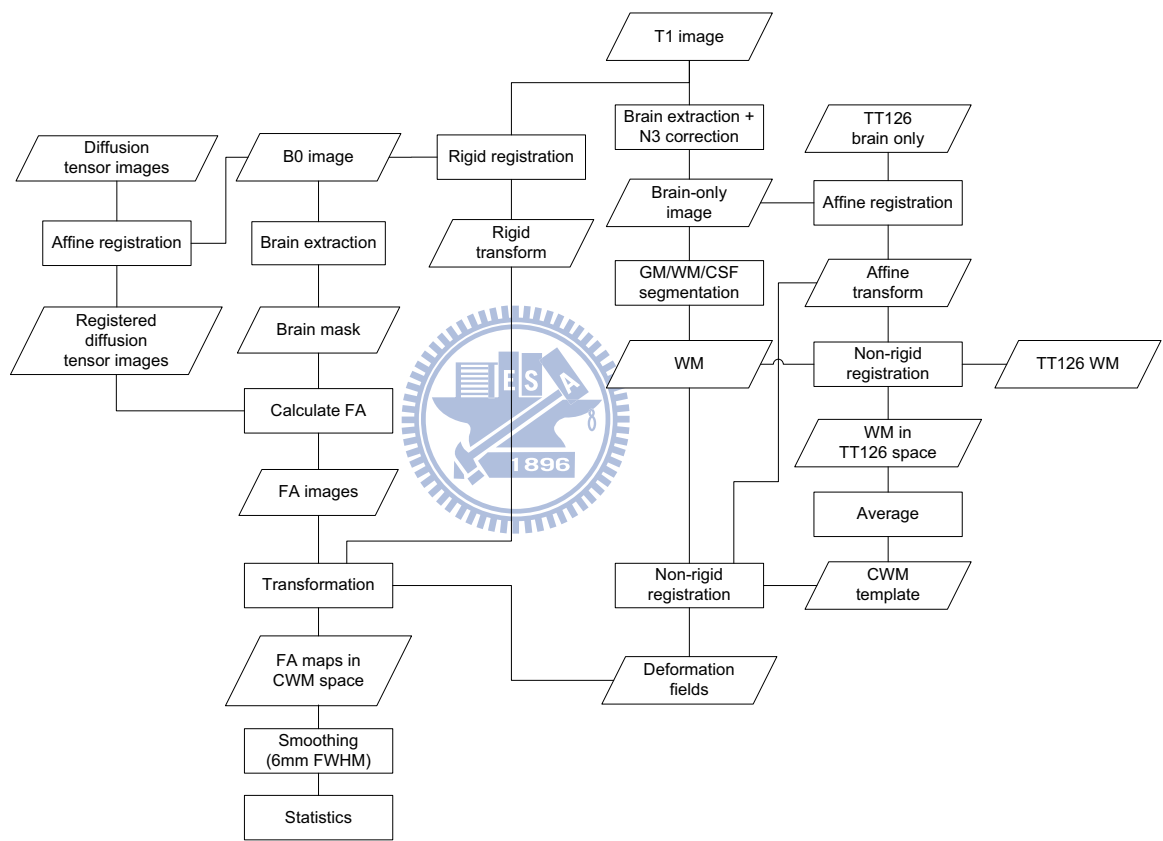


Figure 4.1: Morphometric analysis protocol for bipolar patients.

#### 4.2.4 Statistical analyses

A voxel-wise two-sample t-test analysis using Statistical Parametric Mapping (SPM2)<sup>2</sup> with age, gender, education, and total intracranial volume as covariates was performed to compare the whole-brain FA maps between the control group and three patient groups, including bipolar I, bipolar II, and mixed bipolar groups. This analysis was also performed to directly contrast the FA maps between the bipolar I and II groups. All the regions found in the whole brain analysis (uncorrected,  $p < 0.001$ ) were corrected based on the false discovery rate. The clusters surviving a threshold of  $p < 0.001$  (corrected) were reported as significant loci with structure and fiber labels indicated by Anatomical Automatic Labeling<sup>3</sup> and the probabilistic fiber tracts<sup>4</sup>, respectively. The Mann-Whitney U-test and Pearson  $\chi^2$  test were used to compare the demographic features and the neuropsychological performance, respectively, among the healthy, bipolar I, and bipolar II groups. The Spearman's correlation analysis was also applied to calculate the correlations between the mean FA value of each significant area and the clinical characteristics as well as the scores of neuropsychological tests.

### 4.3 Results

All the group pairs did not differ significantly in age, gender, handedness, education, and duration of illness (for patient groups only) ( $p > 0.05$ ). The comparison results of clinical rating scales showed that only the HARS values of the bipolar II patients were significantly higher than those of the bipolar I patients ( $z = -2.32$ ,  $p = 0.02$ ). In the comparison of neuropsychological performance, the failure to maintain set scores measured from the bipolar I patients was higher than those measured from the bipolar II patients ( $z = -2.0$ ,

<sup>2</sup><http://www.fil.ion.ucl.ac.uk/spm/software/spm2>

<sup>3</sup><http://www.cyceron.fr/freeware>

<sup>4</sup><http://cmrm.med.jhmi.edu>

$p=0.05$ ). The healthy subjects had lower scores of divided attention (sounds) than the bipolar I patients ( $z=-2.25$ ,  $p=0.03$ ) and bipolar II patients ( $z=-2.36$ ,  $p=0.02$ ).

The regions with significantly decreased FA values found in group pairs are listed in Table 4.3. In contrast to the controls, the mixed bipolar group displayed lower FA values in the right thalamus and right subgenual anterior cingulate cortex (Fig. 4.2a). For the bipolar I patients, significant decreases in FA were found in the right thalamus, right subgenual anterior cingulate cortex, right inferior frontal area, and left rostral anterior cingulate cortex, compared to the controls (Fig. 4.2b). The bipolar II patients showed lower FA values than the controls in the bilateral subgenual anterior cingulate, right inferior frontal, left middle temporal, and left inferior temporal areas (Fig. 4.2c). Compared to the controls, no areas with higher FA values were found in three patient groups. The bipolar II patients, compared to bipolar I, presented decreased FA values in the right precuneus, right inferior frontal gyrus, and left inferior prefrontal area (Fig. 4.2d). No areas with higher FA values were found in the bipolar II group compared to the bipolar I patients.

For the areas found in the comparison between the bipolar I and control groups, our correlation analyses showed that the mean FA value of the right subgenual anterior cingulate cortex was significantly correlated with the scores of short-delayed recall ( $\rho=-0.83$ ,  $p<0.001$ ) and the mean FA value of the right inferior frontal area was significantly correlated with the performance of perseverative errors ( $\rho=0.56$ ,  $p=0.04$ ), perseverative responses ( $\rho=0.57$ ,  $p=0.03$ ), and word-list recognition ( $\rho=-0.66$ ,  $p=0.01$ ). For the contrast between the bipolar II and control groups, the mean FA value of the bilateral subgenual anterior cingulate cortex was correlated with the scores of word-list retention ( $\rho=-0.39$ ,  $p=0.05$ ) and YMRS ( $\rho=0.47$ ,  $p=0.01$ ), and the mean FA value of the left middle temporal region was correlated with the performance of perseverative responses ( $\rho=0.59$ ,  $p=0.04$ ). The mean FA value of the left inferior prefrontal area found in the comparison between the bipolar I and II patients was significantly correlated with the hypomanic episode ( $\rho=0.38$ ,  $p<0.05$ ).

Table 4.3: Results of statistical analyses for FA comparison and correlation

Comparison groups	Side	Brodmann area	Fiber tract	MNI coordinate*	Cluster size (mm <sup>3</sup> )	t
<b>Mixed bipolar &lt; Control</b>						
Thalamus	R	-	Anterior thalamic radiation	(13, -1, -8)	472	5.31
Subgenual anterior cingulum	R	11	Corpus callosum forceps minor	(13, 38, -2)	149	4.55
<b>Bipolar I &lt; Control</b>						
Thalamus	R	-	Anterior thalamic radiation	(13, -1, -9)	111	4.94
Subgenual anterior cingulum*	R	11	Corpus callosum forceps minor	(12, 39, -2)	79	3.93
Inferior frontal gyrus*	R	44, 6	Superior longitudinal fasciculus	(49, 2, 23)	303	4.86
Rostral anterior cingulum	L	32	Cingulum	(-10, 37, 20)	79	5.00
<b>Bipolar II &lt; Control</b>						
Subgenual anterior cingulum*	B	11, 25	Corpus callosum forceps minor	(13, 37, 0)	777	5.18
Inferior frontal gyrus	R	48	Inferior frontal-occipital fasciculus	(41, 22, 21)	215	4.79
Middle temporal gyrus	L	37, 21	Superior longitudinal fasciculus	(-43, -52, 8)	118	4.52
Inferior temporal gyrus*	L	20	Inferior frontal-occipital fasciculus	(-30, -24, -1)	133	4.06
<b>Bipolar II &lt; Bipolar I</b>						
Precuneus	R	-	Cingulum	(17, -53, 47)	206	5.58
Inferior frontal gyrus	R	48	Superior longitudinal fasciculus	(30, 12, 28)	94	4.41
Inferior prefrontal gyrus*	L	47	Anterior thalamic radiation	(-30, 37, 8)	77	4.21

L: left; R: right; B: bilateral

\*Peak location (corrected based on false discovery rate,  $p < 0.001$ , cluster threshold=50)

\* Significant correlation with the scores of neuropsychological tests.

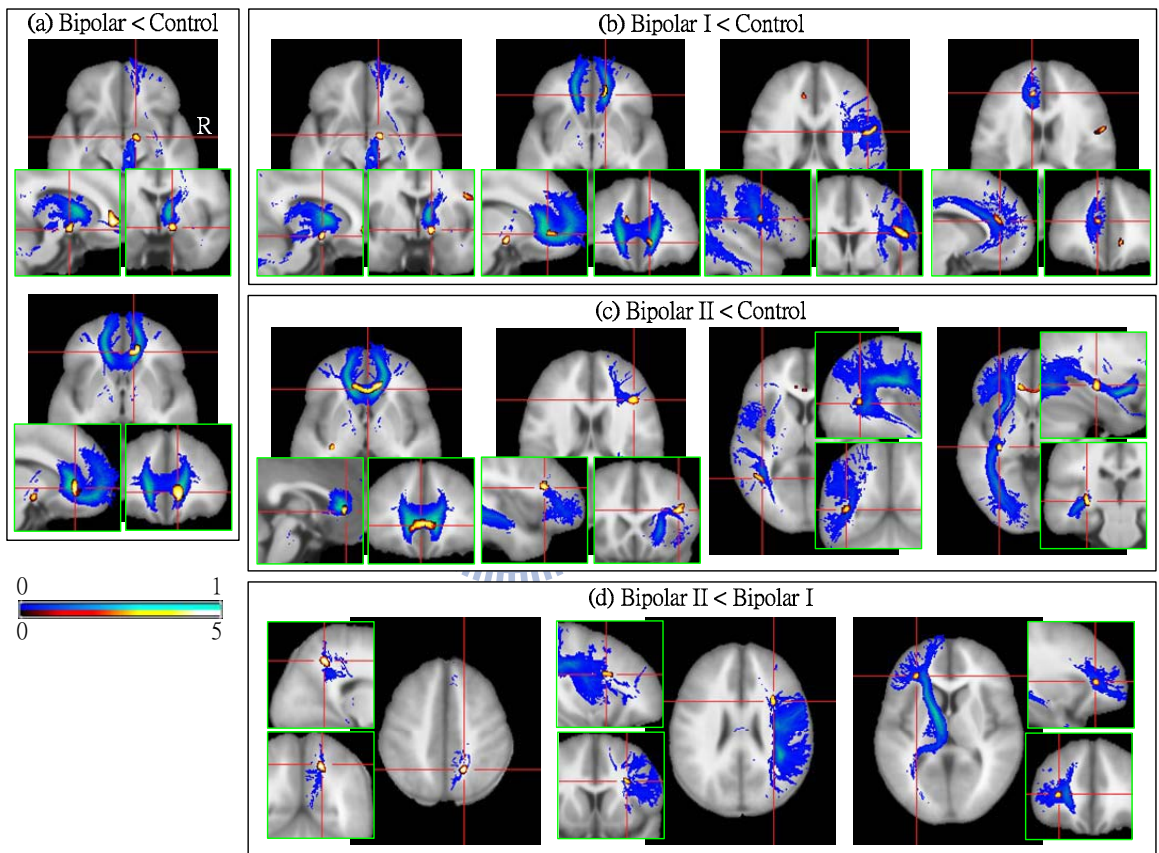


Figure 4.2: Regions with significantly decreased FA values found in the (a) mixed bipolar, (b) bipolar I, and (c) bipolar II groups compared to the controls, and (d) bipolar II group compared to the bipolar I patients. Detailed description of these regions can be found in the text and Table 4.3.

## 4.4 Discussion

In this study the fiber abnormalities of bipolar I and II patients were majorly located in the frontal lobe. The abnormal regions found in bipolar II patients were more bilaterally distributed, extending to the left temporal lobe, whereas the fiber alterations of bipolar I patients were more lateralized to the right hemisphere. Our results suggest that bipolar I and II patients present different neuropathological substrates in terms of the loss of bundle coherence or the disruption of fiber tracts.

Brain regions with significantly decreased FA indices found in the bipolar I patients majorly relate to the cognitive functions. The anterior cingulate cortex is highly involved in the network regulating both cognitive and emotional processing cortex [147]. Particularly, the rostral area found in this study locates in the cognitive division of anterior cingulate [147] and plays an important role in monitoring/signaling conflict or interference, decision making, and response to errors [148]. Thalamus is associated with the modulation of attentional processing and self-regulation of affective states. Its abnormalities were frequently reported in mood disorders, particularly in bipolar disorders [5, 149]. The anterior region of thalamus manifested in the bipolar I patients connects to the prefrontal and temporal areas [150] and is important to affective and cognitive regulation [151]. The inferior frontal area found in bipolar I, which locates in the superior longitudinal fasciculus III [152], participates in attention and executive functions [4] and plays an important role in working memory [152]. Furthermore, this finding in superior longitudinal fasciculus III embraces Brodmann area 44 which belongs to the dorsal attention-cognitive system [153].

The brain areas with fiber deficits found in the bipolar II patients majorly associate with emotional processing. The observed bilateral subgenual anterior cingulate cortex locates in the affective division (Brodmann areas 11 and 25) [147] and is important to emotion regulation, such as affective responses and monitoring of rewarding or punishing results [148]. The middle and inferior temporal areas found in bipolar II patients were related



to bottom-up emotional appraisal processing [154]. The middle temporal area located in the vertical part of arcuate fascicle, which links the frontal and temporal cortices, also modulates audiospatial information [152]. The right inferior frontal area found in bipolar II patients relates to the emotional communicative processing based on facial emotions [155].

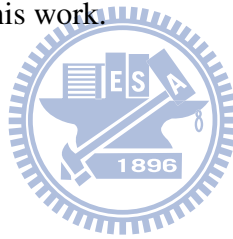
The FA indices of mixed bipolar patients were significantly lower in the right subgenual anterior cingulate cortex and the right thalamus compared to the controls. The right subgenual anterior cingulate cortex observed in both subtypes represents the common fiber abnormality in bipolar patients. This result is consistent with numerous previous findings in functional and volumetric aspects [5]. On the other hand, the thalamus area shown in the mixed bipolar group only revealed in bipolar I group, but not in bipolar II group. This also supports the distinct neural substrates between the two subtypes.

For the contrast between bipolar I and II subtypes, the lower FA values of bipolar II patients in the precuneus implicate the impairments of the appraisal of emotionally salient visual perception as well as the subsequent preprocessing. As reported in [156], the right precuneus of bipolar II patients manifested abnormal activation in response to positive vs. negative captioned pictures compared to healthy controls. The bipolar II patients also presented lower FA indices in the left inferior prefrontal and right inferior frontal areas, which were located in the superior longitudinal fasciculus and anterior thalamic radiation tract, respectively. These two major fiber tracts link to the orbitofrontal cortex and dorsolateral prefrontal cortex that participate in the process of emotion regulation [157]. The fiber abnormality of the right inferior frontal region was also reported in a previous diffusion tensor imaging study [142].

The results of this study indicated that the fiber alterations found in bipolar I and II groups were significantly correlated with the performance of working memory and executive function. However, the FA values of the bipolar I patients were correlated with more neuropsychological tests and these results support the findings of a recent neuropsychological study in which bipolar I patients presented cognitive dysfunction both in pattern and

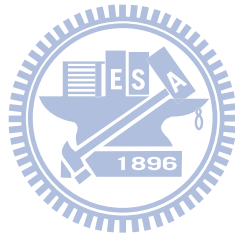
magnitude than bipolar II patients [31]. On the other hand, our correlation results indicated that the bipolar II patients showed significant correlations with emotional symptoms, including YMRS scores and hypomanic episodes. This strengthened the association of bipolar II patients with the abnormal emotion regulation.

Treatments could affect the results of this study though the medication influences on neuropathological abnormalities are currently not certain. Chronic exposure to antipsychotics may alter the volume of thalamus [28]. Antidepressant treatment could decrease the FA in frontal white matter [158]. It was also reported that lithium may protect the anterior cingulate cortices of bipolar patients from volume loss [159]. Due to the variety of medication and the small numbers of patients taking each drug combination, analysis of the medication effects is difficult in this work.



# **Chapter 5**

## **Conclusions and future works**



We have proposed brain extraction and registration algorithms which can be utilized in computational anatomy. The high processing accuracy of our methods facilitates morphometry to report results precisely. Our methods also have the advantage of low computational complexity, and thus are feasible for structural analysis when a large number of participants are involved. The developed image processing techniques have been adopted in an analysis protocol which was conducted to investigate the fiber pathology of bipolar I and II disorders.

This dissertation applied a new implicit deformable model for the development of brain extraction algorithm. Our extraction method was less sensitive to image artifacts, such as intensity inhomogeneity, low signal-to-noise ratio, and the noise spike in k-space. Due to the use of brain structure information, the proposed extraction algorithm can accommodate the varied intensity profiles of images. Furthermore, excess non-brain tissues do not affect the segmentation results of our method significantly. The performance of a brain extraction algorithm generally mediates a trade-off between extraction specificity and sensitivity, and experimental results showed that our method outperformed BSE, BET, HWA, and MLS when jointly considering both criteria. The proposed deformable model utilized a set of Wendland's RBFs to describe object contour smoothly and to fit the brain boundary efficiently. This new model could be further applied to identify the areas of interest for other medical imaging applications. For example, the segmentation of brain tissues or specific anatomical structures is valuable in longitudinal or cross-section morphometry. Locating brain tumors or other pathologies are useful in diagnosis and treatment planning. In addition, further extension of the proposed deformable model is required in order to describe 3-D object surface.

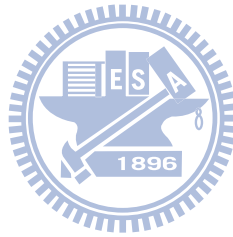
We have introduced affine and non-rigid methods for the registration of brain images. Both algorithms utilized the structure information extracted from the TDOG image. The orientation and position differences between brains can thus be well estimated and the results provide a good initial for the subsequent optimization of affine transformation. Adap-

tively deploying RBFs near the extracted anatomical structures can not only model image deformation accurately but also reduce the computational complexity dramatically. Experimental results indicated that our methods can efficiently align low- and high- resolution brain images with high accuracy compared to SPM2, AIR5, FLIRT, HAMMER, and DARTEL, which are extensively applied in neuroimaging research. It was also demonstrated that the proposed affine and non-rigid algorithms are capable of multi-modality registration, including T1-weighted, T2-weighted, CT, diffusion tensor, and confocal imaging. Nevertheless, further performance validation is necessary for the alignment of different modalities using the proposed approaches.

The morphometric analysis results of bipolar I and II disorders are highly relevant to the literature, given that the pathophysiological differences between these two subtypes are less known. Our results showed that the patients of both subtypes manifested fiber impairments in the thalamus, anterior cingulate, and inferior frontal areas, whereas the bipolar II patients presented more fiber alterations in the temporal and inferior prefrontal regions. Correlations between the mean FA value of each survived area and the clinical characteristics indicated that the left middle temporal and inferior prefrontal FA values of the bipolar II patients were significantly correlated with the scores of YMRS and hypomanic episodes, respectively. The correlation analyses for the scores of neuropsychological tests showed that the FA values of the subgenual anterior cingulate cortices observed in both subtypes correlated with the performance of working memory significantly. Furthermore, the FA values of the right inferior frontal area of bipolar I and the left middle temporal area of bipolar II both correlated with execution function. These findings suggested that the bipolar I patients were majorly associated with cognitive dysfunction, whereas those in the bipolar II patients were related to both cognitive and emotional processing.

Morphometric techniques other than the whole-brain exploration adopted in this dissertation can be further utilized to confirm the analysis results of bipolar disorders. For instance, Tract-Based Spatial Statistics proposed by Smith et al. is also adequate for esti-

mating localized changes of FA maps [160]. To focus the investigation on specific brain regions, one can segment the concerned anatomical structures followed by normalizing the extracted areas into the same stereotaxic space before the statistical inferences. Furthermore, the deformation fields obtained from highly non-rigid registration encode the structural differences between subjects and can also be applied in morphometric studies.



# Bibliography

- [1] C. D. Good, I. Johnsrude, J. Ashburner, R. N. A. Henson, K. J. Friston, and R. S. J. Frackowiak. Cerebral asymmetry and the effects of sex and handedness on brain structure: a voxel-based morphometric analysis of 465 normal adult human brains. *NeuroImage*, 14(3):685–700, 2001.
- [2] C. D. Good, I. S. Johnsrude, J. Ashburner, R. N. A. Henson, K. J. Friston, and R. S. J. Frackowiak. A voxel-based morphometric study of ageing in 465 normal adult human brains. *NeuroImage*, 14(1):21–36, 2001.
- [3] C. Brenneis, S. M. Bösch, M. Schocke, G. K. Wenning, and W. Poewe. Atrophy pattern in SCA2 determined by voxel-based morphometry. *NeuroReport*, 14(14):1799–1802, 2003.
- [4] I. K. Lyoo, M. J. Kim, A. L. Stoll, C. M. Demopulos, A. M. Parow, S. R. Dager, S. D. Friedman, D. L. Dunner, and P. F. Renshaw. Frontal lobe gray matter density decreases in bipolar I disorder. *Biological Psychiatry*, 55(6):648–651, 2004.
- [5] J. Z. Konarski, R. S. McIntyre, S. H. Kennedy, S. Rafi-Tari, J. K. Soczynska, and T. A. Ketter. Volumetric neuroimaging investigations in mood disorders: bipolar disorder versus major depressive disorder. *Bipolar Disorders*, 10(1):1–37, 2008.
- [6] K. Bendfeldt, P. Kuster, S. Traud, H. Egger, S. Winkelhofer, N. Mueller-Lenke, Y. Naegelin, G. E. Achim, L. Kappos, P. M. Matthews, T. E. Nichols, E. W. Radue,

- and S. J. Borgwardt. Association of regional gray matter volume loss and progression of white matter lesions in multiple sclerosis - a longitudinal voxel-based morphometry study. *NeuroImage*, 45(1):60–67, 2009.
- [7] S. Bruno, M. Cercignani, and M. A. Ron. White matter abnormalities in bipolar disorder: a voxel-based diffusion tensor imaging study. *Bipolar Disorders*, 10(4):460–468, 2008.
- [8] K. Mahon, J. H. Wu, A. K. Malhotra, K. E. Burdick, P. DeRosse, B. A. Ardekani, and P. R. Szeszko. A voxel-based diffusion tensor imaging study of white matter in bipolar disorder. *Neuropsychopharmacology*, 34(6):1590–1600, 2009.
- [9] D. Le Bihan, J. F. Mangin, C. Poupon, C. A. Clark, S. Pappata, N. Molko, and H. Chabriat. Diffusion tensor imaging: concepts and applications. *Journal of Magnetic Resonance Imaging*, 13(4):534–546, 2001.
- [10] D. Mitchen and C. Gaser. Computational morphometry for detecting changes in brain structure due to development, aging, learning, disease and evolution. *Frontiers in Neuroinformatics*, 3:25–25, 2009.
- [11] J. Ashburner and K. J. Friston. Voxel-based morphometry - the methods. *NeuroImage*, 11(6):805–821, 2000.
- [12] M. K. Chung, K. J. Worsley, T. Paus, C. Cherif, D. L. Collins, J. N. Giedd, J. L. Rapoport, and A. C. Evans. A unified statistical approach to deformation-based morphometry. *NeuroImage*, 14(3):595–606, 2001.
- [13] M. K. Chung, K. J. Worsley, S. Robbins, T. Paus, J. Taylor, J. N. Giedd, J. L. Rapoport, and A. C. Evans. Deformation-based surface morphometry applied to gray matter deformation. *NeuroImage*, 18(2):198–213, 2003.
- [14] David H. Salat, Randy L. Buckner, Abraham Z. Snyder, Douglas N. Greve, Rahul S.R. Desikan, Evelina Busa, John C. Morris, Anders M. Dale, and Bruce



- Fischl. Thinning of the cerebral cortex in aging. *Cerebral Cortex*, 14(7):721–730, 2004.
- [15] M. S. Panizzon, C. Fennema-Notestine, L. T. Eyler, T. L. Jernigan, E. Prom-Wormley, M. Neale, K. Jacobson, M. J. Lyons, M. D. Grant, C. E. Franz, H. Xian, M. Tsuang, B. Fischl, L. Seidman, A. Dale, and W. S. Kremen. Distinct genetic influences on cortical surface area and cortical thickness. *Cerebral Cortex*, 19(11):2728–2735, 2009.
- [16] David C. Van Essen, Donna Dierker, A. Z. Snyder, Marcus E. Raichle, Allan L. Reiss, and Julie Korenberg. Symmetry of cortical folding abnormalities in Williams syndrome revealed by surface-based analyses. *Journal of Neuroscience*, 26(20):5470–5483, 2006.
- [17] J. G. Sled, A. P. Zijdenbos, and A. C. Evans. A nonparametric method for automatic correction of intensity nonuniformity in MRI data. *IEEE Transactions on Medical Imaging*, 17(1):87–97, 1998.
- [18] J. Jovicich, S. Czanner, D. Greve, E. Haley, A. van der Kouwe, R. Gollub, D. Kennedy, F. Schmitt, G. Brown, J. MacFall, B. Fischl, and A. Dale. Reliability in multi-site structural MRI studies: effects of gradient non-linearity correction on phantom and human data. *NeuroImage*, 30(2):436–443, 2006.
- [19] C. Fennema-Notestine, I. B. Ozyurt, C. P. Clark, S. Morris, A. Bischoff-Grethe, M. W. Bondi, T. L. Jernigan, B. Fischl, F. Segonne, D. W. Shattuck, R. M. Leahy, D. E. Rex, A. W. Toga, K. H. Zou, M. Birn, and G. G. Brown. Quantitative evaluation of automated skull-stripping methods applied to contemporary and legacy images: effects of diagnosis, bias correction, and slice location. *Human Brain Mapping*, 27(2):99–113, 2006.
- [20] J. Acosta-Cabronero, G. B. Williams, J. M. S. Pereira, G. Pengas, and P. J. Nestor.

- The impact of skull-stripping and radio-frequency bins correction on grey-matter segmentation for voxel-based morphometry. *NeuroImage*, 39(4):1654–1665, 2008.
- [21] J. C. Mazziotta, A. W. Toga, A. Evans, P. Fox, and J. Lancaster. A probabilistic atlas of the human brain - theory and rationale for its development. *NeuroImage*, 2(2):89–101, 1995.
- [22] A. C. Evans, D. L. Collins, S. R. Mills, E. D. Brown, R. L. Kelly, and T. M. Peters. 3D statistical neuroanatomical models from 305 MRI volumes. In *Nuclear Science Symposium and Medical Imaging Conference*, volume 3, pages 1813–1817, San Francisco, USA, 1993.
- [23] J. Mazziotta, A. Toga, A. Evans, P. Fox, J. Lancaster, K. Zilles, R. Woods, T. Paus, G. Simpson, B. Pike, C. Holmes, L. Collins, P. Thompson, D. MacDonald, M. Iacoboni, T. Schormann, K. Amunts, N. Palomero-Gallagher, S. Geyer, L. Parsons, K. Narr, N. Kabani, G. Le Goualher, D. Boomsma, T. Cannon, R. Kawashima, and B. Mazoyer. A probabilistic atlas and reference system for the human brain: International Consortium for Brain Mapping (ICBM). *Philosophical Transactions of the Royal Society of London - Series B: Biological Sciences*, 356(1412):1293–1322, 2001.
- [24] S. M. Smith. Fast robust automated brain extraction. *Human Brain Mapping*, 17(3):143–155, 2002.
- [25] F. Ségonne, A. M. Dale, E. Busa, M. Glessner, D. Salat, H. K. Hahn, and B. Fischl. A hybrid approach to the skull stripping problem in MRI. *NeuroImage*, 22(3):1060–1075, 2004.
- [26] A. H. Zhuang, D. J. Valentino, and A. W. Toga. Skull-stripping magnetic resonance brain images using a model-based level set. *NeuroImage*, 32(1):79–92, 2006.

- [27] J. X. Liu, Y. S. Chen, and L. F. Chen. Accurate and robust extraction of brain regions using a deformable model based on radial basis functions. *Journal of Neuroscience Methods*, 183(2):255–266, 2009.
- [28] M. M. Haznedar, F. Roversi, S. Pallanti, N. Baldini-Rossi, D. B. Schnur, E. M. LiCalzi, C. Tang, P. R. Hof, E. Hollander, and M. S. Buchsbaum. Fronto-thalamo-striatal gray and white matter volumes and anisotropy of their connections in bipolar spectrum illnesses. *Biological Psychiatry*, 57(7):733–742, 2005.
- [29] M. Summers, K. Papadopoulou, S. Bruno, L. Cipolotti, and M. A. Ron. Bipolar I and bipolar II disorder: cognition and emotion processing. *Psychological Medicine*, 36(12):1799–1809, 2006.
- [30] S. Dittmann, K. Hennig-Fast, S. Gerber, F. Seemuller, M. Riedel, W. Severus, J. Langosch, R. R. Engel, H. J. Moller, and H. C. Grunze. Cognitive functioning in euthymic bipolar I and bipolar II patients. *Bipolar Disorders*, 10(8):877–887, 2008.
- [31] C. Simonsen, K. Sundet, A. Vaskinn, A. B. Birkenaes, J. A. Engh, C. F. Hansen, H. Jonsdottir, P. A. Ringen, S. Opjordsmoen, S. Friis, and O. A. Andreassen. Neurocognitive profiles in bipolar I and bipolar II disorder: differences in pattern and magnitude of dysfunction. *Bipolar Disorders*, 10(2):245–255, 2008.
- [32] M. Rovaris and M. Filippi. MR-based technology for in vivo detection, characterization, and quantification of pathology of relapsing-remitting multiple sclerosis. *Journal of Rehabilitation Research and Development*, 39(2):243–259, 2002.
- [33] A. M. Dale, B. Fischl, and M. I. Sereno. Cortical surface-based analysis - I. segmentation and surface reconstruction. *NeuroImage*, 9(2):179–194, 1999.
- [34] Y. Y. Zhang, M. Brady, and S. Smith. Segmentation of brain MR images through a hidden Markov random field model and the expectation-maximization algorithm. *IEEE Transactions on Medical Imaging*, 20(1):45–57, 2001.

- [35] D. W. Shattuck, S. R. Sandor-Leahy, K. A. Schaper, D. A. Rottenberg, and R. M. Leahy. Magnetic resonance image tissue classification using a partial volume model. *NeuroImage*, 13(5):856–876, 2001.
- [36] R. P. Woods, S. T. Grafton, J. D. G. Watson, N. L. Sicotte, and J. C. Mazziotta. Automated image registration II: intersubject validation of linear and nonlinear models. *Journal of Computer Assisted Tomography*, 22(1):153–165, 1998.
- [37] M. Jenkinson and S. Smith. A global optimisation method for robust affine registration of brain images. *Medical Image Analysis*, 5(2):143–156, 2001.
- [38] A. Gholipour, N. Kehtarnavaz, R. Briggs, M. Devous, and K. Gopinath. Brain functional localization: a survey of image registration techniques. *IEEE Transactions on Medical Imaging*, 26(4):427–451, 2007.
- [39] J. X. Liu, Y. S. Chen, and L. F. Chen. Nonlinear registration based on the approximation of radial basis function coefficients. *Journal of Medical and Biological Engineering*, 28(3):119–126, 2008.
- [40] J. L. Beyer and K. R. R. Krishnan. Volumetric brain imaging findings in mood disorders. *Bipolar Disorders*, 4(2):89–104, 2002.
- [41] G. B. Karas, E. J. Burton, S. A. R. B. Rombouts, R. A. van Schijndel, J. T. O’Brien, P. Scheltens, I. G. McKeith, D. Williams, C. Ballard, and F. Barkhof. A comprehensive study of gray matter loss in patients with Alzheimer’s disease using optimized voxel-based morphometry. *NeuroImage*, 18(4):895–907, 2003.
- [42] Y. S. Chen, L. F. Chen, Y. T. Chang, Y. T. Huang, T. P. Su, and J. C. Hsieh. Quantitative evaluation of brain magnetic resonance images using voxel-based morphometry and Bayesian theorem for patients with bipolar disorder. *Journal of Medical and Biological Engineering*, 28(3):127–133, 2008.

- [43] G. Fein, B. Landman, H. Tran, J. Barakos, K. Moon, V. Di Sclafani, and R. Shumway. Statistical parametric mapping of brain morphology: sensitivity is dramatically increased by using brain-extracted images as inputs. *NeuroImage*, 30(4):1187–1195, 2006.
- [44] L. Lemieux, G. Hagemann, K. Krakow, and F. G. Woermann. Fast, accurate, and reproducible automatic segmentation of the brain in T1-weighted volume MRI data. *Magnetic Resonance in Medicine*, 42(1):127–135, 1999.
- [45] R. W. Cox. AFNI: software for analysis and visualization of functional magnetic resonance neuroimages. *Computers and Biomedical Research*, 29(3):162–173, 1996.
- [46] B. D. Ward. Intracranial segmentation. Technical report, Biophysics Research Institute, Medical College of Wisconsin, 1999.
- [47] H. K. Hahn and H. O. Peitgen. The skull stripping problem in MRI solved by a single 3D watershed transform. *Lecture Notes in Computer Science*, 1935:134–143, 2000.
- [48] M. E. Brummer, R. M. Mersereau, R. L. Eisner, and R. R. J. Lewine. Automatic detection of brain contours in MRI data sets. *IEEE Transactions on Medical Imaging*, 12(2):153–166, 1993.
- [49] C. Lee, S. Huh, T. A. Ketter, and M. Unser. Unsupervised connectivity-based thresholding segmentation of midsagittal brain MR images. *Computers in Biology and Medicine*, 28(3):309–338, 1998.
- [50] A. J. Worth, N. Makris, J. W. Meyer, V. S. Caviness, and D. N. Kennedy. Semiautomatic segmentation of brain exterior in magnetic resonance images driven by empirical procedures and anatomical knowledge. *Medical Image Analysis*, 2(4):315–324, 1998.

- [51] Y. Hata, S. Kobashi, S. Hirano, H. Kitagaki, and E. Mori. Automated segmentation of human brain MR images aided by fuzzy information granulation and fuzzy inference. *IEEE Transactions on Systems Man and Cybernetics Part C-Applications and Reviews*, 30(3):381–395, 2000.
- [52] R. Stokking, K. L. Vincken, and M. A. Viergever. Automatic morphology-based brain segmentation (MBRASE) from MRI-T1 data. *NeuroImage*, 12(6):726–738, 2000.
- [53] S. Huh, T. A. Ketter, K. H. Sohn, and C. H. Lee. Automated cerebrum segmentation from three-dimensional sagittal brain MR images. *Computers in Biology and Medicine*, 32(5):311–328, 2002.
- [54] M. Bomans, K. H. Höhne, U. Tiede, and M. Riemer. 3-D segmentation of MR images of the head for 3-D display. *IEEE Transactions on Medical Imaging*, 9(2):177–183, 1990.
- [55] S. Sandor and R. Leahy. Surface-based labeling of cortical anatomy using a deformable atlas. *IEEE Transactions on Medical Imaging*, 16(1):41–54, 1997.
- [56] C. Xu, D. L. Pham, and J. L. Prince. *Image segmentation using deformable models*. Handbook of Medical Imaging. SPIE Press, Bellingham, 2000.
- [57] J. Montagnat, H. Delingette, and N. Ayache. A review of deformable surfaces: topology, geometry and deformation. *Image and Vision Computing*, 19(14):1023–1040, 2001.
- [58] C. Davatzikos and R. N. Bryan. Using a deformable surface model to obtain a shape representation of the cortex. *IEEE Transactions on Medical Imaging*, 15(6):785–795, 1996.
- [59] A. Kelemen, G. Székely, and G. Gerig. Elastic model-based segmentation of 3-D

- neuroradiological data sets. *IEEE Transactions on Medical Imaging*, 18(10):828–839, 1999.
- [60] M. S. Atkins and B. T. Mackiewich. Fully automatic segmentation of the brain in MRI. *IEEE Transactions on Medical Imaging*, 17(1):98–107, 1998.
- [61] G. B. Aboutanos, J. Nikanne, N. Watkins, and B. M. Dawant. Model creation and deformation for the automatic segmentation of the brain in MR images. *IEEE Transactions on Biomedical Engineering*, 46(11):1346–1356, 1999.
- [62] L. Germond, M. Dojat, C. Taylor, and C. Garbay. A cooperative framework for segmentation of MRI brain scans. *Artificial Intelligence in Medicine*, 20(1):77–93, 2000.
- [63] C. Baillard, P. Hellier, and C. Barillot. Segmentation of brain 3D MR images using level sets and dense registration. *Medical Image Analysis*, 5(3):185–194, 2001.
- [64] D. E. Rex, D. W. Shattuck, R. P. Woods, K. L. Narr, E. Luders, K. Rehm, S. E. Stolzner, D. A. Rottenberg, and A. W. Toga. A meta-algorithm for brain extraction in MRI. *NeuroImage*, 23(2):625–637, 2004.
- [65] A. Mikheev, G. Nevsky, S. Govindan, R. Grossman, and H. Rusinek. Fully automatic segmentation of the brain from T1-weighted MRI using Bridge Burner algorithm. *Journal of Magnetic Resonance Imaging*, 27(6):1235–1241, 2008.
- [66] K. Rehm, K. Schaper, J. Anderson, R. Woods, S. Stoltzner, and D. Rottenberg. Putting our heads together: a consensus approach to brain/non-brain segmentation in T1-weighted MR volumes. *NeuroImage*, 22(3):1262–1270, 2004.
- [67] N. Otsu. Threshold selection method from gray-level histograms. *IEEE Transactions on Systems Man and Cybernetics*, 9(1):62–66, 1979.

- [68] H. Wendland. Piecewise polynomial, positive definite and compactly supported radial functions of minimal degree. *Advances in Computational Mathematics*, 4(1):389–396, 1995.
- [69] M. Fornefett, K. Rohr, and H. S. Stiehl. Radial basis functions with compact support for elastic registration of medical images. *Image and Vision Computing*, 19(1-2):87–96, 2001.
- [70] J. M. Lee, U. Yoon, S. H. Nam, J. H. Kim, I. Y. Kim, and S. I. Kim. Evaluation of automated and semi-automated skull-stripping algorithms using similarity index and segmentation error. *Computers in Biology and Medicine*, 33(6):495–507, 2003.
- [71] K. Boesen, K. Rehm, K. Schaper, S. Stoltzner, R. Woods, E. Luders, and D. Rotenberg. Quantitative comparison of four brain extraction algorithms. *NeuroImage*, 22(3):1255–1261, 2004.
- [72] D. W. Shattuck and R. M. Leahy. BrainSuite: an automated cortical surface identification tool. *Medical Image Analysis*, 6(2):129–142, 2002.
- [73] S. Smith, P. R. Bannister, C. Beckmann, M. Brady, S. Clare, D. Flitney, P. Hansen, M. Jenkinson, D. Lebovici, B. Ripley, M. Woolrich, and Y. Y. Zhang. FSL: new tools for functional and structural brain image analysis. *NeuroImage*, 13(6):S249–S249, 2001.
- [74] H. G. Schnack, N. E. M. van Haren, H. E. H. Pol, M. Picchioni, M. Weisbrod, H. Sauer, T. Cannon, M. Huttunen, R. Murray, and R. S. Kahn. Reliability of brain volumes from multicenter MRI acquisition: a calibration study. *Human Brain Mapping*, 22(4):312–320, 2004.
- [75] P. A. Freeborough and N. C. Fox. Modeling brain deformations in Alzheimer disease by fluid registration of serial 3D MR images. *Journal of Computer Assisted Tomography*, 22(5):838–843, 1998.



- [76] A. Oatridge, J.V. Hajnal, and G.M. Bydder. *Registration and subtraction of serial magnetic resonance images of the brain: image interpretation and clinical applications*. Medical Image Registration. CRC, Boca Raton, 2001.
- [77] P. M. Thompson, J. N. Gledd, R. P. Woods, D. MacDonald, A. C. Evans, and A. W. Toga. Growth patterns in the developing brain detected by using continuum mechanical tensor maps. *Nature*, 404(6774):190–193, 2000.
- [78] D. Rey, G. Subsol, H. Delingette, and N. Ayache. Automatic detection and segmentation of evolving processes in 3D medical images: application to multiple sclerosis. *Medical Image Analysis*, 6(2):163–179, 2002.
- [79] A. C. Evans, D. L. Collins, and B. Milner. An MRI-based stereotactic atlas from 250 young normal subjects. In *Society for Neuroscience (Abstract)*, volume 18, pages 408–408, 1992.
- [80] J. Talairach and P. Tournoux. *Co-planar stereotaxic atlas of the human brain*. Thieme Medical Publishers, New York, 1988.
- [81] D. L. Collins, C. J. Holmes, T. M. Peters, and A. C. Evans. Automatic 3-D model-based neuroanatomical segmentation. *Human Brain Mapping*, 3(3):190–208, 1995.
- [82] T. F. Cootes, C. Beeston, G. J. Edwards, and C. J. Taylor. A unified framework for atlas matching using active appearance models. *Lecture Notes in Computer Science*, 1613:322–333, 1999.
- [83] J. Ashburner, P. Neelin, D. L. Collins, A. Evans, and K. Friston. Incorporating prior knowledge into image registration. *NeuroImage*, 6(4):344–352, 1997.
- [84] R. P. Woods, S. T. Grafton, C. J. Holmes, S. R. Cherry, and J. C. Mazziotta. Automated image registration I: general methods and intrasubject, intramodality validation. *Journal of Computer Assisted Tomography*, 22(1):139–152, 1998.

- [85] M. Jenkinson, P. Bannister, M. Brady, and S. Smith. Improved optimization for the robust and accurate linear registration and motion correction of brain images. *NeuroImage*, 17(2):825–841, 2002.
- [86] D. L. G. Hill, P. G. Batchelor, M. Holden, and D. J. Hawkes. Medical image registration. *Physics in Medicine and Biology*, 46(3):R1–R45, 2001.
- [87] J. P. W. Pluim, J. B. A. Maintz, and M. A. Viergever. Mutual-information-based registration of medical images: a survey. *IEEE Transactions on Medical Imaging*, 22(8):986–1004, 2003.
- [88] B. Zitová and J. Flusser. Image registration methods: a survey. *Image and Vision Computing*, 21(11):977–1000, 2003.
- [89] R. Bajcsy and S. Kovačič. Multiresolution elastic matching. *Computer Vision, Graphics, and Image Processing*, 46:1–21, 1989.
- [90] H. Lester and S. R. Arridge. A survey of hierarchical non-linear medical image registration. *Pattern Recognition*, 32(1):129–149, 1999.
- [91] D. Rueckert. *Nonrigid registration: concepts, algorithms, and applications*. Medical Image Registration. CRC, Boca Raton, 2001.
- [92] G. E. Christensen, R. D. Rabbitt, and M. I. Miller. Deformable templates using large deformation kinematics. *IEEE Transactions on Image Processing*, 5(10):1435–1447, 1996.
- [93] M. Bro-Nielsen and C. Gramkow. Fast fluid registration of medical images. *Lecture Notes in Computer Science*, 1131:267–276, 1996.
- [94] J. P. Thirion. Image matching as a diffusion process: an analogy with Maxwell’s demons. *Medical Image Analysis*, 2(3):243–260, 1998.

- [95] T. Vercauteren, X. Pennec, A. Perchant, and N. Ayache. Non-parametric diffeomorphic image registration with the demons algorithm. *Lecture Notes in Computer Science*, 4792:319–326, 2007.
- [96] P. J. Edwards, D. L. G. Hill, J. A. Little, and D. J. Hawkes. Deformation for image guided interventions using a three component tissue model. *Lecture Notes in Computer Science*, 1230:218–231, 1997.
- [97] J. Ashburner, J. L. R. Andersson, and K. J. Friston. High-dimensional image registration using symmetric priors. *NeuroImage*, 9(6):619–628, 1999.
- [98] M. Ferrant, A. Nabavi, B. Macq, F. A. Jolesz, R. Kikinis, and S. K. Warfield. Registration of 3-D intraoperative MR images of the brain using a finite-element biomechanical model. *IEEE Transactions on Medical Imaging*, 20(12):1384–1397, 2001.
- [99] D. G. Shen and C. Davatzikos. HAMMER: hierarchical attribute matching mechanism for elastic registration. *IEEE Transactions on Medical Imaging*, 21(11):1421–1439, 2002.
- [100] O. Škrinjar, A. Nabavi, and J. Duncan. Model-driven brain shift compensation. *Medical Image Analysis*, 6(4):361–373, 2002.
- [101] M. Sermesant, C. Forest, X. Pennec, H. Delingette, and N. Ayache. Deformable biomechanical models: application to 4D cardiac image analysis. *Medical Image Analysis*, 7(4):475–488, 2003.
- [102] G. R. Wu, F. H. Qi, and D. G. Shen. Learning-based deformable registration of MR brain images. *IEEE Transactions on Medical Imaging*, 25(9):1145–1157, 2006.
- [103] F. L. Bookstein. Principal warps: thin-plate splines and the decomposition of deformations. *IEEE Transactions on Pattern Analysis and Machine Intelligence*, 11(6):567–585, 1989.

- [104] J. A. Little, D. L. G. Hill, and D. J. Hawkes. Deformations incorporating rigid structures. *Computer Vision and Image Understanding*, 66(2):223–232, 1997.
- [105] N. Arad, N. Dyn, D. Reifeld, and Y. Yeshurun. Image warping by radial basis functions: application to facial expressions. *CVGIP-Graphical Models and Image Processing*, 56(2):161–172, 1994.
- [106] D. Ruprecht, R. Nagel, and H. Müller. Spatial free-form deformation with scattered data interpolation methods. *Computers and Graphics*, 19(1):63–71, 1995.
- [107] B. Likar and F. Pernuš. A hierarchical approach to elastic registration based on mutual information. *Image and Vision Computing*, 19(1-2):33–44, 2001.
- [108] Y. Amit. A nonlinear variational problem for image matching. *SIAM Journal on Scientific Computing*, 15(1):207–224, 1994.
- [109] J. Ashburner and K. J. Friston. Nonlinear spatial normalization using basis functions. *Human Brain Mapping*, 7(4):254–266, 1999.
- [110] D. Rueckert, L. I. Sonoda, C. Hayes, D. L. G. Hill, M. O. Leach, and D. J. Hawkes. Nonrigid registration using free-form deformations: application to breast MR images. *IEEE Transactions on Medical Imaging*, 18(8):712–721, 1999.
- [111] J. Kybic, P. Thévenaz, A. Nirkko, and M. Unser. Unwarping of unidirectionally distorted EPI images. *IEEE Transactions on Medical Imaging*, 19(2):80–93, 2000.
- [112] G. K. Rohde, A. Aldroubi, and B. M. Dawant. The adaptive bases algorithm for intensity-based nonrigid image registration. *IEEE Transactions on Medical Imaging*, 22(11):1470–1479, 2003.
- [113] J. P. W. Pluim, J. B. A. Maintz, and M. A. Viergever. Image registration by maximization of combined mutual information and gradient information. *IEEE Transactions on Medical Imaging*, 19(8):809–814, 2000.

- [114] S. Marsland, C. J. Twining, and C. J. Taylor. Groupwise non-rigid registration using polyharmonic clamped-plate splines. *Lecture Notes in Computer Science*, 2879:771–779, 2003.
- [115] O. Camara, G. Delso, O. Colliot, A. Moreno-Ingelmo, and I. Bloch. Explicit incorporation of prior anatomical information into a nonrigid registration of thoracic and abdominal CT and 18-FDG whole-body emission PET images. *IEEE Transactions on Medical Imaging*, 26(2):164–178, 2007.
- [116] J. S. Kim, J. M. Lee, Y. H. Lee, J. S. Kim, I. Y. Kim, and S. I. Kim. Intensity based affine registration including feature similarity for spatial normalization. *Computers in Biology and Medicine*, 32(5):389–402, 2002.
- [117] P. Cachier, E. Bardinet, D. Dormont, X. Pennec, and N. Ayache. Iconic feature based nonrigid registration: the PASHA algorithm. *Computer Vision and Image Understanding*, 89(2-3):272–298, 2003.
- [118] P. Hellier and C. Barillot. Coupling dense and landmark-based approaches for non-rigid registration. *IEEE Transactions on Medical Imaging*, 22(2):217–227, 2003.
- [119] T. M. Liu, D. G. Shen, and C. Davatzikos. Deformable registration of cortical structures via hybrid volumetric and surface warping. *NeuroImage*, 22(4):1790–1801, 2004.
- [120] C. J. Twining, T. Cootes, S. Marsland, V. Petrovic, R. Schestowitz, and C. J. Taylor. A unified information-theoretic approach to groupwise non-rigid registration and model building. *Lecture Notes in Computer Science*, 3565:1–14, 2005.
- [121] F. L. Bookstein. “Voxel-based morphometry” should not be used with imperfectly registered images. *NeuroImage*, 14(6):1454–1462, 2001.
- [122] J. Ashburner and K. J. Friston. Why voxel-based morphometry should be used. *NeuroImage*, 14(6):1238–1243, 2001.

- [123] B. A. Ardekani, S. Guckemus, A. Bachman, M. J. Hoptman, M. Wojtaszek, and J. Nierenberg. Quantitative comparison of algorithms for inter-subject registration of 3D volumetric brain MRI scans. *Journal of Neuroscience Methods*, 142(1):67–76, 2005.
- [124] C. Chu, G. Tan, and J. Ashburner. Improving voxel-based morphometry with diffeomorphic non-linear registration by DARTEL toolbox: conventional SPM normalization vs. DARTEL normalization. In *The 14th Annual Meeting of the Organization for Human Brain Mapping*, Melbourne, Australia, 2008.
- [125] W. H. Press, S. A. Teukolsky, W. T. Vetterling, and B. P. Flannery. *Numerical recipes in C : the art of scientific computing*. Cambridge University Press, New York, 1992.
- [126] A. V. Tuzikov, O. Colliot, and I. Bloch. Evaluation of the symmetry plane in 3D MR brain images. *Pattern Recognition Letters*, 24(14):2219–2233, 2003.
- [127] B. A. Ardekani, J. Kershaw, M. Braun, and I. Kanno. Automatic detection of the mid-sagittal plane in 3-D brain images. *IEEE Transactions on Medical Imaging*, 16(6):947–952, 1997.
- [128] Y. X. Liu, R. T. Collins, and W. E. Rothfus. Robust midsagittal plane extraction from normal and pathological 3-D neuroradiology images. *IEEE Transactions on Medical Imaging*, 20(3):175–192, 2001.
- [129] P. Kowalczyk and M. Mrozowski. Mesh-free approach to Helmholtz equation based on radial basis functions. In *The 15th International Conference on Microwave, Radar and Wireless Communication*, pages 702–705, Warsaw, Poland, 2004.
- [130] A. Collignon, F. Maes, D. Delaere, D. Vandermeulen, P. Suetens, and G. Marchal. Automated multimodality medical image registration using information theory. In *Proceedings of the Information Processing in Medical Imaging*, pages 263–274, 1995.

- [131] P. Viola and W. M. Wells. Alignment by maximization of mutual information. *International Journal of Computer Vision*, 24(2):137–154, 1997.
- [132] C. Studholme, D. L. G. Hill, and D. J. Hawkes. An overlap invariant entropy measure of 3D medical image alignment. *Pattern Recognition*, 32(1):71–86, 1999.
- [133] A. Roche, G. Malandain, X. Pennec, and N. Ayache. The correlation ratio as a new similarity measure for multimodal image registration. *Lecture Notes in Computer Science*, 1496:1115–1124, 1998.
- [134] J. P. W. Pluim, J. B. A. Maintz, and M. A. Viergever. Interpolation artefacts in mutual information-based image registration. *Computer Vision and Image Understanding*, 77(2):211–232, 2000.
- [135] J. Ashburner. A fast diffeomorphic image registration algorithm. *NeuroImage*, 38(1):95–113, 2007.
- [136] D. L. Collins, A. P. Zijdenbos, V. Kollokian, J. G. Sled, N. J. Kabani, C. J. Holmes, and A. C. Evans. Design and construction of a realistic digital brain phantom. *IEEE Transactions on Medical Imaging*, 17(3):463–468, 1998.
- [137] B. Karacali and C. Davatzikos. Simulation of tissue atrophy using a topology preserving transformation model. *IEEE Transactions on Medical Imaging*, 25(5):649–652, 2006.
- [138] O. Camara, M. Schweiger, R. I. Scahill, W. R. Crum, B. I. Sneller, J. A. Schnabel, G. R. Ridgway, D. M. Cash, D. L. G. Hill, and N. C. Fox. Phenomenological model of diffuse global and regional atrophy using finite-element methods. *IEEE Transactions on Medical Imaging*, 25(11):1417–1430, 2006.
- [139] O. Camara, J. A. Schnabel, G. R. Ridgway, W. R. Crum, A. Douiri, R. I. Scahill, D. L. G. Hill, and N. C. Fox. Accuracy assessment of global and local atrophy

- measurement techniques with realistic simulated longitudinal Alzheimer's disease images. *NeuroImage*, 42(2):696–709, 2008.
- [140] A. U. Turken, S. Whitfield-Gabrieli, R. Bammer, J. V. Baldo, N. F. Dronkers, and J. D. E. Gabrieli. Cognitive processing speed and the structure of white matter pathways: convergent evidence from normal variation and lesion studies. *NeuroImage*, 42(2):1032–1044, 2008.
- [141] C. Steinbrink, K. Vogt, A. Kastrup, H. P. Müller, F. D. Juengling, J. Kassubeek, and A. Riecker. The contribution of white and gray matter differences to developmental dyslexia: insights from DTI and VBM at 3.0 T. *Neuropsychologia*, 46(13):3170–3178, 2008.
- [142] C. M. Adler, S. K. Holland, V. Schmithorst, M. Wilke, K. L. Weiss, H. Pan, and S. M. Strakowski. Abnormal frontal white matter tracts in bipolar disorder: a diffusion tensor imaging study. *Bipolar Disorders*, 6(3):197–203, 2004.
- [143] J. L. Beyer, W. D. Taylor, J. R. MacFall, M. Kuchibhatla, M. E. Payne, J. M. Provenza, F. Cassidy, and K. R. R. Krishnan. Cortical white matter microstructural abnormalities in bipolar disorder. *Neuropsychopharmacology*, 30(12):2225–2229, 2005.
- [144] W. T. Regenold, C. A. D'Agostino, N. Ramesh, M. Hasnain, S. Roys, and R. P. Gullapalli. Diffusion-weighted magnetic resonance imaging of white matter in bipolar disorder: a pilot study. *Bipolar Disorders*, 8(2):188–195, 2006.
- [145] N. Makris, A. J. Worth, A. G. Sorensen, G. M. Papadimitriou, O. Wu, T. G. Reese, V. J. Wedeen, T. L. Davis, J. W. Stakes, V. S. Caviness, E. Kaplan, B. R. Rosen, D. N. Pandya, and D. N. Kennedy. Morphometry of in vivo human white matter association pathways with diffusion-weighted magnetic resonance imaging. *Annals of Neurology*, 42(6):951–962, 1997.



- [146] J. X. Liu, Y. S. Chen, and L. F. Chen. Fast and accurate registration techniques for affine and nonrigid alignment of mr brain images. *Annals of Biomedical Engineering*, DOI: 10.1007/s10439-009-9840-9, 2009.
- [147] G. Bush, P. Luu, and M. I. Posner. Cognitive and emotional influences in anterior cingulate cortex. *Trends in Cognitive Sciences*, 4(6):215–222, 2000.
- [148] A. M. C. Kelly, A. Di Martino, L. Q. Uddin, Z. Shehzad, D. G. Gee, P. T. Reiss, D. S. Margulies, F. X. Castellanos, and M. P. Milham. Development of anterior cingulate functional connectivity from late childhood to early adulthood. *Cerebral Cortex*, 19(3):640–657, 2009.
- [149] J. K. Zubieta, P. Huguelet, L. E. Ohl, R. A. Koeppe, M. R. Kilbourn, J. M. Carr, B. J. Giordani, and K. A. Frey. High vesicular monoamine transporter binding in asymptomatic bipolar I disorder: sex differences and cognitive correlates. *American Journal of Psychiatry*, 157(10):1619–1628, 2000.
- [150] T. E. J. Behrens, H. Johansen-Berg, M. W. Woolrich, S. M. Smith, C. A. M. Wheeler-Kingshott, P. A. Boulby, G. J. Barker, E. L. Sillery, K. Sheehan, O. Ciccarelli, A. J. Thompson, J. M. Brady, and P. M. Matthews. Non-invasive mapping of connections between human thalamus and cortex using diffusion imaging. *Nature Neuroscience*, 6(7):750–757, 2003.
- [151] J. P. Aggleton and M. W. Brown. Episodic memory, amnesia and the hippocampal-anterior thalamic axis. *Behavioral and Brain Sciences*, 22(3):425–489, 1999.
- [152] N. Makris, D. N. Kennedy, S. McInerney, A. G. Sorensen, R. Wang, V. S. Caviness, and D. N. Pandya. Segmentation of subcomponents within the superior longitudinal fascicle in humans: a quantitative, in vivo, DT-MRI study. *Cerebral Cortex*, 15(6):854–869, 2005.

- [153] H. S. Mayberg. Limbic-cortical dysregulation: a proposed model of depression. *Journal of Neuropsychiatry and Clinical Neurosciences*, 9(3):471–481, 1997.
- [154] T. Onitsuka, M. E. Shenton, D. F. Salisbury, C. C. Dickey, K. Kasai, S. K. Toner, M. Frumin, R. Kikinis, F. A. Jolesz, and R. W. McCarley. Middle and inferior temporal gyrus gray matter volume abnormalities in chronic schizophrenia: an MRI study. *American Journal of Psychiatry*, 161(9):1603–1611, 2004.
- [155] K. Nakamura, R. Kawashima, K. Ito, M. Sugiura, T. Kato, A. Nakamura, K. Hatano, S. Nagumo, K. Kubota, H. Fukuda, and S. Kojima. Activation of the right inferior frontal cortex during assessment of facial emotion. *Journal of Neurophysiology*, 82(3):1610–1614, 1999.
- [156] G. S. Malhi, J. Lagopoulos, P. Sachdev, P. B. Mitchell, B. Ivanovski, and G. B. Parker. Cognitive generation of affect in hypomania: an fMRI study. *Bipolar Disorders*, 6(4):271–285, 2004.
- [157] M. Phillips, C. Ladouceur, and W. Drevets. A neural model of voluntary and automatic emotion regulation: implications for understanding the pathophysiology and neurodevelopment of bipolar disorder. *Molecular Psychiatry*, 13(9):833–857, 2008.
- [158] G. S. Alexopoulos, D. N. Kiosses, S. J. Choi, C. F. Murphy, and K. O. Lim. Frontal white matter microstructure and treatment response of late-life depression: a preliminary study. *American Journal of Psychiatry*, 159(11):1929–1932, 2002.
- [159] R. B. Sassi, P. Brambilla, J. P. Hatch, M. A. Nicoletti, A. G. Mallinger, E. Frank, D. J. Kupfer, M. S. Keshavan, and J. C. Soares. Reduced left anterior cingulate volumes in untreated bipolar patients. *Biological Psychiatry*, 56(7):467–475, 2004.
- [160] S. M. Smith, M. Jenkinson, H. Johansen-Berg, D. Rueckert, T. E. Nichols, C. E. Mackay, K. E. Watkins, O. Ciccarelli, M. Z. Cader, P. M. Matthews, and T. E. J.

Behrens. Tract-based spatial statistics: voxelwise analysis of multi-subject diffusion data. *NeuroImage*, 31(4):1487–1505, 2006.

